



**EXPERIMENTAL VIBRATION ANALYSIS OF
INFLATABLE BEAMS FOR AN AFIT
SPACE SHUTTLE EXPERIMENT**

THESIS

Thomas G. Single, Captain, USAF

AFIT/GSO/ENY/02-2

**DEPARTMENT OF THE AIR FORCE
AIR UNIVERSITY**

AIR FORCE INSTITUTE OF TECHNOLOGY

Wright-Patterson Air Force Base, Ohio

APPROVED FOR PUBLIC RELEASE; DISTRIBUTION UNLIMITED

Report Documentation Page

Report Date 26 Mar 02	Report Type Final	Dates Covered (from... to) Aug 2000 - Mar 202
Title and Subtitle Experimental Vibration Analysis of Inflatable Beams for an AFIT Space Shuttle Experiment		Contract Number
		Grant Number
		Program Element Number
Author(s) Capt Thomas G. Single, USAF		Project Number
		Task Number
		Work Unit Number
Performing Organization Name(s) and Address(es) Air Force Institution of Technology 2950 P Street, Bldg 640 WPAFB, OH 45433-7765		Performing Organization Report Number AFIT/GSO/ENY/02-2
Sponsoring/Monitoring Agency Name(s) and Address(es) Mr. Daniel Segalman AFOSR/NA Structural Mechanics 801 North Randolph Street Arlington, VA 22203		Sponsor/Monitor's Acronym(s)
		Sponsor/Monitor's Report Number(s)
Distribution/Availability Statement Approved for public release, distribution unlimited		
Supplementary Notes		
Abstract The development of lightweight, large-aperture optics is of vital importance to the Department of Defense and the US Air Force for improving remote sensing capabilities. One way of constructing a large space structure is to use rigidized, inflatable beams. This research presents the experimental vibration analysis of the ground testing for inflatable beams that will be used in an AFIT Space Shuttle rigidized inflatable beams experiment. The natural frequencies, damping ratios, and bending modes were identified for the beams. Various parameters were modified to determine what affects the vibration characteristics of the beams. The test results were compared to an Euler-Bernouli beam model using a itz approximation.		
Subject Terms RIGEX, Inflatable structures, Inflatable Beams, Vibration testing, Model Analysis, GASCAN Experiments, Large Space Structures, Experimental Vibration Analysis		
Report Classification unclassified		Classification of this page unclassified

Classification of Abstract unclassified	Limitation of Abstract UU
Number of Pages 179	

The views expressed in this thesis are those of the author and do not reflect the official policy or position of the United States Air Force, Department of Defense, or the United States Government.

AFIT/GSO/ENY/02-2

EXPERIMENTAL VIBRATION ANALYSIS OF
INFLATABLE BEAMS FOR AN AFIT
SPACE SHUTTLE EXPERIMENT

THESIS

Presented to the Faculty
Department of Aeronautics and Astronautics
Graduate School of Engineering and Management
Air Force Institute of Technology
Air University
Air Education and Training Command
in Partial Fulfillment of the Requirements for the
Degree of Master of Science

Thomas G. Single, BS, MBA
Captain, USAF

March, 2002


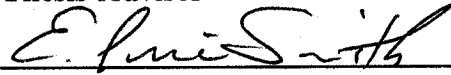

APPROVED FOR PUBLIC RELEASE; DISTRIBUTION UNLIMITED

EXPERIMENTAL VIBRATION ANALYSIS OF
INFLATABLE BEAMS FOR AN AFIT
SPACE SHUTTLE EXPERIMENT

Thomas G. Single, BS, MBA

Captain, USAF

Approved:

 Major Gregory Agnes Thesis Advisor	<u>15 Mar 02</u> Date
 Lt Col E. Price Smith Committee Member	<u>18 Mar 02</u> Date
 Major Richard Cobb Committee Member	<u>18 Mar 02</u> Date

Acknowledgements

I would like to express my sincere appreciation to my thesis advisor, Major Greg Agnes, for his insight and guidance were greatly valued, and any short-comings in this work are to be blamed only on myself. Additionally, it would not have been possible to complete my experimental work without the help of Mr. Wilber Lacy and Mr. Jay Anderson of AFIT Aeronautics Department Laboratories. Thanks for your creativity and all your help!

Thanks goes to Dr. Steve Tragresser for listening to my endless ramblings on space topics, and even though he couldn't talk me out of abusing myself and attempting a double major, I do appreciate his efforts and wish I had listened to him. I would also like to thank Dr. Gregg Gunsch, Major Richard Cobb, Lt Col Price Smith and Lt Col Robert Canfield for their advice, support, and expertise. My study of vibrations was greatly aided by Dr. Joe Slater of Wright State University for writing the Vibrations Toolbox for MATLAB® and to Dr. Daniel Inman of Virginia Tech for writing *Engineering Vibration, 2nd Ed.*, without a doubt the best introductory text on the study of vibrations.

Additionally, I could not have completed my studies at AFIT without the support and help of my fellow students. I would like to especially thank my fellow Space Operations students: Squadron Leader David Warren, Captain David Borgeson, 1Lt Ayhan Tucay, and 1Lt Fatih Temiz and the Astronautical Engineering students: Captain Erin Carreher, Captain Mike Sobers, and Lt Hakan San. A special thanks goes to my wife who sacrificed as much as I did during our time in Dayton. Her love, support, and encouragement kept me going.

Thomas G. Single

Table of Contents

	Page
Acknowledgements	iv
List of Figures	viii
List of Tables	xiv
Abstract	xvi
I. Introduction	1-1
1.1 Background and Benefits to the Air Force	1-2
1.2 Scope of Project	1-8
1.3 RIGEX Background	1-9
1.4 Research Objectives	1-9
1.5 Assumptions/Constraints	1-11
1.6 Methodology	1-11
1.7 Summary of Thesis	1-12
II. Literature Review	2-1
2.1 Overview	2-1
2.2 Gossamer Spacecraft	2-1
2.3 Vibration and Modal Testing Theory	2-4
2.4 Frequency Response Method	2-7
2.5 Dynamic Analysis of Inflated Beam Structures	2-9
2.5.1 Previous Inflatable Beam Experimental Results	2-9
2.5.2 A Dynamic Analysis of Inflated Beam Structures	2-9
2.5.3 Improved Beam-Bending Model for Inflatables	2-14
2.6 Summary	2-14
III. Experimental Methodology	3-1
3.1 Inflatable Beams Description	3-2
3.1.1 Beam Irregularities	3-4
3.1.2 Material Properties	3-7
3.2 Experimental Procedure	3-8
3.3 Experiment Equipment and Setup	3-10
3.3.1 Data Acquisition	3-11

	Page
3.3.2 Driver Description	3-16
3.3.3 PZT adhesives	3-19
3.3.4 Sensor Description	3-22
3.3.5 Accelerometer Calibration	3-27
3.3.6 Vacuum Chamber Setup	3-29
3.3.7 Heaters	3-31
3.4 Analytic Beam Model	3-35
3.4.1 Kinematics of Deformation	3-35
3.4.2 Energy	3-35
3.4.3 Equations of Motion	3-36
3.4.4 Analytical Results	3-37
3.4.5 Convergence	3-38
3.5 Experimental Vibrations Testing Overview	3-41
3.5.1 Ambient Condition Tests	3-42
3.5.2 Vacuum Chamber Tests	3-44
3.6 Modal Analysis Using ERA	3-48
3.7 Summary	3-50
IV. Experimental Results and Analysis	4-1
4.1 Shaker Tests Results	4-4
4.1.1 Short Beams	4-5
4.1.2 PZT tests with Beam S03 on the Shaker	4-10
4.1.3 Long Beams	4-12
4.2 Test Stand Tests Results	4-13
4.3 Vacuum Testing and Analysis	4-22
4.4 Comparison to Analytic Results	4-28
4.5 Summary	4-28
V. Discussion of Results	5-1
5.1 Beam Characterization Results	5-1
5.1.1 Trial Comparisons	5-1
5.1.2 Excitation Comparison	5-6
5.1.3 Orientation Comparison	5-8
5.2 Pressure Comparison	5-12
5.3 Temperature Comparison	5-23
5.4 Vacuum Comparison	5-25
5.5 Summary	5-25

	Page
VI. Summary and Future Work	6-1
6.1 Summary	6-1
6.2 Future Work	6-1
Appendix A. RIGEX CAD Drawings [13]	A-1
Appendix B. Photos of Beam Irregularities	B-1
B.1 Beam S02	B-1
B.2 Beam S03	B-2
B.3 Beam S04	B-3
B.4 Beam S05	B-4
B.5 Beam S06	B-6
Appendix C. Modal Testing Data	C-1
C.1 FRF Excitation Comparisons for S02	C-1
C.2 FRF Pressure Comparisons for S02	C-3
C.3 FRF Orientation Comparisons for S02	C-8
C.4 S03 with PZT Test Data	C-8
Appendix D. Vacuum Tests Data	D-1
Bibliography	BIB-1
Vita	VITA-1

List of Figures

Figure		Page
1.1.	Inflatable Antenna Experiment viewed from the Space Shuttle	1-3
1.2.	Effect of Aperture Size on Resolution (Alt. of 0-20,000km). .	1-4
1.3.	Effect of Aperture Size on Resolution (Alt. of 0-5000km). . .	1-5
1.4.	Sample Satellite Coverage (STK-VO)	1-6
1.5.	Sample Worldwide Satellite Coverage (STK)	1-7
1.6.	The proposed RIGEX Space Shuttle Experiment	1-8
1.7.	Inflatable Beam	1-10
2.1.	IRSS packaged	2-2
2.2.	L'Garde Inflatable Truss	2-2
2.3.	L'Garde Inflatable Strut Solar Panel	2-3
2.4.	Single Degree of Freedom System	2-4
2.5.	Single Degree of Freedom System - Beam Bending	2-6
3.1.	Diagram of Inflatable Beams (Short Beam)	3-3
3.2.	Diagram of Inflatable Beam Numbering	3-3
3.3.	Four of the short beams with the base flanges in line and touching.	3-4
3.4.	Close-up of the 4 short beams. Note the gap between the tip flanges.	3-5
3.5.	Beam surface closeup of irregularities.	3-6
3.6.	Surface comparison of smooth and irregular beam surface (Beams L01 and L03)	3-6
3.7.	Experiment Setup	3-11
3.8.	Hewlett Packard System	3-12
3.9.	SignalCalc 620 Main GUI Screen	3-13
3.10.	Electro-Seis [®] Model 113-LA Shaker with a Short Beam mounted.	3-16
3.11.	FRF of Amplifier Test on S02	3-17
3.12.	FRF of Shaker with a Mounted Beam	3-18
3.13.	Closeup of base end of beam S03	3-20

Figure		Page
3.14.	Beam S03 with PZT installed.	3-21
3.15.	Closeup of the PZT on S03	3-21
3.16.	ENDEVCO 2250A – 10 Accelerometer shown mounted on the shaker arm.	3-22
3.17.	ENDEVCO 63B-100 Accelerometer. The Σ Z-mount clip is on the right. Note that the accelerometer is NOT the actual size.	3-23
3.18.	Typical Amplitude and Temperature Response	3-23
3.19.	Accelerometer Axis Alignment	3-24
3.20.	PSV 300 Laser Vibrometer	3-25
3.21.	PSV Rectangular Mesh Scan Points	3-26
3.22.	PSV Triangle Mesh Scan Points	3-26
3.23.	PSV GUI	3-27
3.24.	Accelerometer Calibration Setup	3-28
3.25.	Vacuum Chamber with heating canister and Beam S03	3-30
3.26.	Vacuum Chamber Setup (Internal View)	3-31
3.27.	Example of a Minco Thermofoil TM heater	3-32
3.28.	Heating Canister	3-33
3.29.	Heating canister with MINCO Thermofoil TM heaters installed	3-34
3.30.	Wire Diagram of Heater Power System	3-34
3.31.	1st Bending Mode at 1 Hz	3-39
3.32.	2nd Bending Mode at 60.9 Hz	3-40
3.33.	3rd Bending Mode at 196.9 Hz	3-40
3.34.	4th Bending Mode at 417.3 Hz	3-40
3.35.	Short beam mounted on shaker	3-41
3.36.	Beam S03 with PZT installed.	3-42
3.37.	Long Beam on the shaker	3-43
3.38.	Beam S03 in Vacuum Chamber with no damping applied to the structure.	3-46
3.39.	Beam in vacuum chamber without the heater canister installed.	3-47
3.40.	Beam S03 in vacuum with heater canister installed.	3-48
3.41.	ERA Program	3-49

Figure		Page
4.1.	Sample of Results from MATLAB of FRF of Accelerometer and Vibrometer	4-1
4.2.	FRF for X,Y,and Z axis of S04	4-2
4.3.	FRF ERA fit for S02-1 at 125mV and 0psi	4-3
4.4.	Sample of Results for FRF, Phase, and Coherence from MATLAB (using EZERA data)	4-4
4.5.	FRFs from PSV - Short Beams	4-6
4.6.	PSV 3-D Model @ 12 Hz	4-8
4.7.	PSV 3-D Model @ 32 Hz	4-9
4.8.	PSV 3-D Model @ 61 Hz	4-9
4.9.	PSV 3-D Model @ 232 Hz	4-10
4.10.	Z axis FRF for S03 with PZT on shaker at 4 psi (Shaker exciting)	4-11
4.11.	Z axis FRF for S03 with PZT on shaker at 4 psi (PZT exciting)	4-12
4.12.	FRF ERAfit L01 0psi	4-13
4.13.	Z axis FRF for S03 w/ PZT on Test Stand @ 4 psi (PZT exciting)	4-14
4.14.	Z axis FRF Comparison from PSV for S03 with PZT	4-15
4.15.	Short Beam Comparison of Omega vs Mode	4-15
4.16.	Short Beam Comparison of Omega vs Mode for Shaker/PZT driving	4-16
4.17.	Omega vs Mode for Shaker and Test Stand	4-17
4.18.	PSV - Beam S03 @ 34Hz on test stand with PZT as the exciter (side view)	4-18
4.19.	PSV - Beam S03 @ 34Hz on test stand with PZT as the exciter(length view)	4-18
4.20.	PSV - Beam S03 @ 130Hz on test stand with PZT as the exciter(side view)	4-19
4.21.	PSV - Beam S03 @ 130Hz on test stand with PZT as the exciter(length view)	4-19
4.22.	PSV - Beam S03 @ 211Hz on test stand with PZT as the exciter(side view)	4-20
4.23.	PSV - Beam S03 @ 211Hz on test stand with PZT as the exciter(length view)	4-20
4.24.	PSV - Beam S03 @ 230Hz on test stand with PZT as the exciter(side view)	4-21

Figure		Page
4.25.	PSV - Beam S03 @ 230Hz on test stand with PZT as the exciter(length view)	4-21
4.26.	FRF for Beam S03 in Vacuum at 25 C	4-23
4.27.	FRF for Beam S03 in Vacuum at 95 C	4-24
4.28.	Vacuum Comparison of Peak Frequency vs Temperature for Modes 1 and 2	4-25
4.29.	Vacuum Comparison of Damping vs Temperature for Modes 1 and 2	4-25
4.30.	Vacuum Comparison of Damping vs Temperature for Mode3	4-26
4.31.	Vacuum Comparison of Damping vs Temperature for Mode 3	4-26
4.32.	Vacuum Comparison of Omega vs Temperature for 0 psi . . .	4-27
4.33.	Vacuum Comparison of Zeta vs Temperature for 0 psi	4-27
5.1.	Trial Comparison for S02-1 @ 0psi, 125mV	5-2
5.2.	Trial Number Comparison: Zeta vs Omega for S02-1	5-4
5.3.	Z axis (Vibrometer) FRF Comparison of 3 Trials, S02-1 0psi, 125mV, 1000Hz	5-4
5.4.	Z axis(Vibrometer) FRF Comparison of 3 Trials, S02-1 0psi, 125mV, 300 Hz	5-5
5.5.	Excitation Comparison (0-1000 Hz) for S02-1 @ 0psi	5-7
5.6.	Excitation Comparison (0-200 Hz) for S02-1 @ 0psi	5-7
5.7.	Excitation Comparison: Zeta vs Omega for S02-1	5-8
5.8.	Orientation Comparison (0-1000 Hz for S02 @ 0psi,300mV)	5-9
5.9.	Orientation Comparison (0-200 Hz for S02 @ 0psi,300mV) .	5-9
5.10.	Omega vs Position Orientation Comparison of the 1st 8 modes for S02 @ 0psi,300mV)	5-10
5.11.	Zeta vs. Omega Orientation Comparison (0-1000 Hz for S02 @ 0psi,300mV)	5-11
5.12.	Zeta vs Omega Orientation Comparison of the 1st 8 modes for S02 @ 0psi,300mV)	5-11
5.13.	Pressure Comparison (0-1000 Hz for S02-1 @ 300mV) . . .	5-12
5.14.	Pressure Comparison (0-200 Hz for S02-1 @ 300mV)	5-13
5.15.	Pressure Comparison: Zeta vs Omega for S04-1 for Raw Data	5-14
5.16.	Omega vs Mode for Pressure Comparison from PSV	5-15

Figure		Page
5.17.	Individual Short Beam Pressure Comparisons from PSV . . .	5-16
5.18.	FRF for Pressure Comparison	5-17
5.19.	Zeta vs Omega for Pressure Comparison: Zeta vs Omega for S02-1	5-18
5.20.	Pressure Comparison: Zeta vs Omega for S04-1 for Aligned Data	5-19
5.21.	FRF PSV - Long Beams	5-20
5.22.	PSV Long Beam Comparison	5-20
5.23.	Pressure comparison L01	5-21
5.24.	Pressure comparison L03	5-22
5.25.	Temperature Comparisons for S03	5-23
5.26.	Omega and Zeta vs Temperature Comparisons for S03	5-24
5.27.	Omega and Zeta Temperature Comparisons for 0 & 4 psi. . .	5-24
5.28.	Ambient vs. Vacuum Comparisons for S03 @ 25C	5-25
5.29.	Ambient vs. Vacuum Comparisons for S03 @ 45C	5-26
B.1.	Beam Surface S02	B-1
B.2.	Beam Surface S02	B-1
B.3.	Beam Surface S03	B-2
B.4.	Beam Surface S03	B-2
B.5.	Beam Surface S04	B-3
B.6.	Beam Surface S04	B-3
B.7.	Beam Surface S05	B-4
B.8.	Beam Surface S05	B-4
B.9.	Beam Surface S05	B-5
B.10.	Beam Surface S06	B-6
B.11.	Beam Surface S06	B-6
C.1.	Sample of Results used for Trial Comparison	C-1
C.2.	Sample of Results used for Trial Comparison	C-2
C.3.	Sample of Results used for Trial Comparison	C-2
C.4.	Sample of Results used for Trial Comparison	C-3
C.5.	Sample of Results used for Trial Comparison	C-4
C.6.	Sample of Results used for Trial Comparison	C-4

Figure		Page
C.7.	Sample of Results used for Trial Comparison	C-5
C.8.	Pressure Comparisons for S05-1	C-6
C.9.	Pressure Comparisons for S06-1	C-7
C.10.	Sample of Results used for Trial Comparison	C-8
C.11.	Sample of Results used for Trial Comparison	C-9
C.12.	Sample of Results used for Trial Comparison	C-9

List of Tables

Table		Page
1.1.	Satellite Coverage of the Earth Surface	1-7
2.1.	Summary of Main's Omega and Zeta values	2-12
3.1.	Equipment Physical Properties	3-7
3.2.	Short Beam (2-3) Physical Properties	3-7
3.3.	Long Beam Physical Properties	3-8
3.4.	Accelerometer Sensitivities	3-29
3.5.	Ritz Approximation Convergence for Beam S03	3-39
3.6.	Shaker Test Matrix	3-45
3.7.	Vacuum Chamber Test Matrix, Excitation level-40V	3-47
4.1.	Short Beam Peak Frequency (Hz) calculated from PSV for S02-2 @0 psi	4-7
4.2.	Short Beam Bending Modes from PSV: Mean Freq. at 0 and 4 psi	4-7
4.3.	Short Beam Omega Values from PSV and ERA at 0 and 4 psi	4-8
4.4.	S03 with PZT Omega Values at 4 psi from PSV and ERA	4-11
4.5.	Long Beam Omega Values from ERA and PSV at 0 and 4 psi	4-13
4.6.	Short Beam Omega Values at 0 and 4 psi for S03 & S03 w/ PZT	4-22
4.7.	Summary of Vacuum Tests at 0 & 4 psi	4-23
4.8.	Summary of Bending Modes for the Short Beams	4-28
5.1.	Mean Values for 3 Trials Comparison for S02-1 @0 psi, 125mV	5-3
5.2.	Mean Values for Excitation Comparison	5-8
5.3.	Mean Values for Orientation Comparison for S02 @ 0psi,300mV	5-10
5.4.	Mean Values for Pressure Comparison	5-13
C.1.	S03 with PZT on with Shaker exciting at 0, 2, and 4 psi	C-10
C.2.	S03 with PZT with Shaker exciting at 6 psi	C-10

Table		Page
D.1.	Vacuum Tests 0psi , 25°C to 95°C	D-2
D.2.	Vacuum Tests 4psi 25°C and 35°C	D-3
D.3.	Vacuum Tests 4psi , 45°C to 95°C	D-3

Abstract

The Department of Defense, NASA, and others are considering space-based inflatable structures to reduce the costs associated with the design, manufacturing, and launch of space structures. The Rigidized Inflatable Get-Away-Special Experiment (RIGEX) is an autonomous, self-contained Space Shuttle experiment that will inflate and rigidize several cylindrical beam structures. After inflation and rigidization, the experiment will perform a vibration analysis by exciting the rigidized beams with piezoelectric transducers (PZTs) and collecting the acceleration at the tip of the beam via a tri-axial accelerometer in the zero-g vacuum of space. This thesis presents the experimental vibration analysis for the beams on the ground, using a shaker for excitation to characterize the modal properties. Piezoelectric transducers are then used for excitation in modal tests in a near-vacuum. The test data for the bending modes are compared to an Euler-Bernoulli beam theory model to determine its validity for analytic prediction.

EXPERIMENTAL VIBRATION ANALYSIS OF INFLATABLE BEAMS FOR AN AFIT SPACE SHUTTLE EXPERIMENT

I. Introduction

The United States has become dependent on satellites and the capability and service that they provide. Satellites are used by the military for all aspect of operations, including: communications, surveillance, reconnaissance, navigation, command and control, meteorology, and information operations. The Air Force is making advances in space technology and improving our capability. However, as space structures become more complex and more capable, they often become increasingly larger, and their cost and weight increase significantly. This is especially true for intelligence, surveillance and reconnaissance (ISR) satellite capability, which is dependent upon the size of the optics. Consequently, research on inflatable space structures is making a resurgence.

Three concerns dominate the space optics industry and drive all spacecraft design: aperture size (of optics or antennas), available power, and launch cost.[24] Current technology uses highly polished mirrors that are extremely expensive and heavy. These mirrors and the the supporting space structure are also limited by the size of the expendable launcher or the Space Shuttle. The Air Force's Research Laboratory (AFRL) is helping to lead the development of revolutionary new technologies by creating a dramatic shift in spacecraft design and capability.[24] Research is being done on large deployable mirrors and membrane optics to be able to increase the size of the aperture and to potentially reduce cost. One of the main components will be the supporting space structure for the vehicle, and the component that will

hold the mirror or membrane. Research was conducted by NASA in the 1960's on inflatable structures; however, the advent of increased launcher size and the familiarity with rigid/mechanical structures led to inflatables not being used for most space applications.[26]

This research is a start towards enabling the Department of Defense, NASA, and others in the space industry to be able to build large space structures, especially optical and remote sensing platforms, by using rigidized inflatable beams. There are many potential uses for inflatable structures if they can be reliably modelled before they are built and sent into space. Inflatables can be used to for large membrane optics, solar concentrators and collectors, solar arrays, truss systems, habitat modules in orbit and on the surface of the moon, the possibilities are limited only by ones imagination. The modal analysis and experimental testing on the ground is an essential first step. If the zero-g tests and the ground testing can be correlated and accurate methods of modelling can be developed, the future use of inflatable structures is likely.

1.1 Background and Benefits to the Air Force

The first observations from space were of poor quality and of limited coverage. As technology has matured, the Air Force has come to rely on space-based assets for its intelligence, surveillance, and reconnaissance. The space environment however, presents many challenges. Rocket technology has not advanced that much in the last 40 years and currently costs approximately \$10,000 per pound to launch a satellite into space.[35] Objects put into orbit must survive the launch into space, deploy and function without failure or “hands-on” assistance, must have a long operational life, and be protected against the radiation and temperature extremes in space.

The term “gossamer structure” is used to describe ultra-low-mass space structures. A space-inflatable structure is a specific application of a membrane structure that is comprised of highly flexible plate or shell-like elements, for example the poly-

mer films Kapton or Mylar. These films usually have a low-modulus of elasticity and very little bending stiffness. Consequently, they are usually found in inflated-curved configurations.[26] In 1996, the L'Garde Corporation flight tested the Inflatable Antenna Experiment (IAE), shown in Figure 1.1. The IAE successfully demonstrated

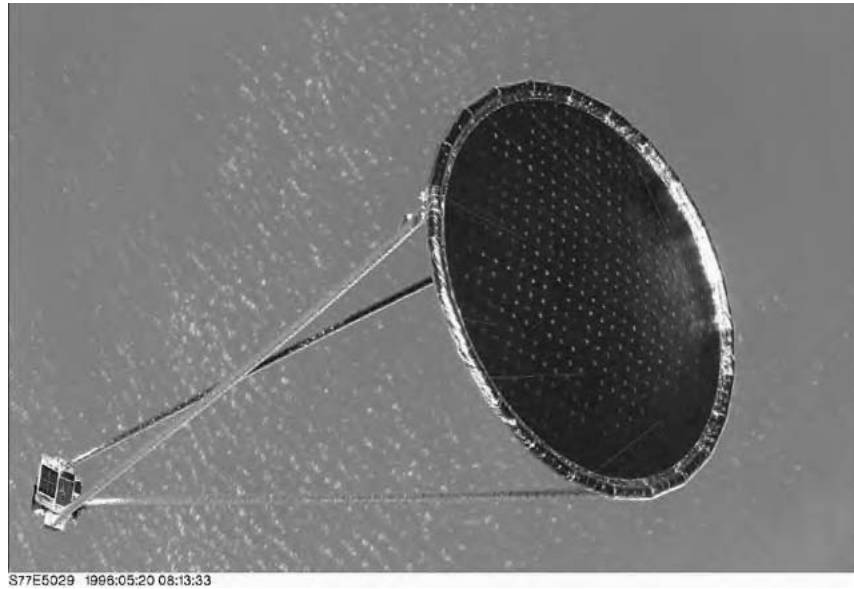


Figure 1.1 Inflatable Antenna Experiment viewed from the Space Shuttle

L'Garde's and NASA's objectives of validating their criteria for the development of large, flight-quality hardware for a low-cost, high mechanical-packaging efficiency, low weight, high deployment reliability, usable reflector-surface precision, and thermal stability in a realistic space environment.[19]

Inflatable and rigidizable structures potentially offer the Air Force significant benefits, by reducing the packing size and weight of the structures, the launch costs, and possibly reducing the cost of the satellite structure. Inflatables also offer a significant improvement in our ability to view the earth from space. These beams or struts will be the foundation of the structure for large optical intelligence, surveillance, and reconnaissance satellites.

Two key factors in determining the capability (ground resolution) of optical satellites are the altitude of the satellite and the aperture size of the mirror.[35] The

aperture size of the optics on a satellite is often limited by the payload size and launch weight to get it into orbit. Other factors such as slant angle, sun azimuth angle, environmental effects, etc. are also part of determining the ground resolution. However, using Equation 1.1 [35] gives a good approximation for the ground resolution as a function of height of the satellite at a given wavelength of observation.

$$\text{Ground Resolution} = \frac{2.44 * h * \lambda}{D} \quad (1.1)$$

where h is the satellite altitude above the ground, λ is the wavelength, and D is the aperture diameter.

Using the Equation 1.1 in MATLAB®, Figure 1.2 shows the effect aperture size on ground resolution for various altitudes and four different aperture sizes. The figure demonstrates that for a one meter aperture, the satellite must stay relatively close to the earth to have a better than one meter ground resolution.

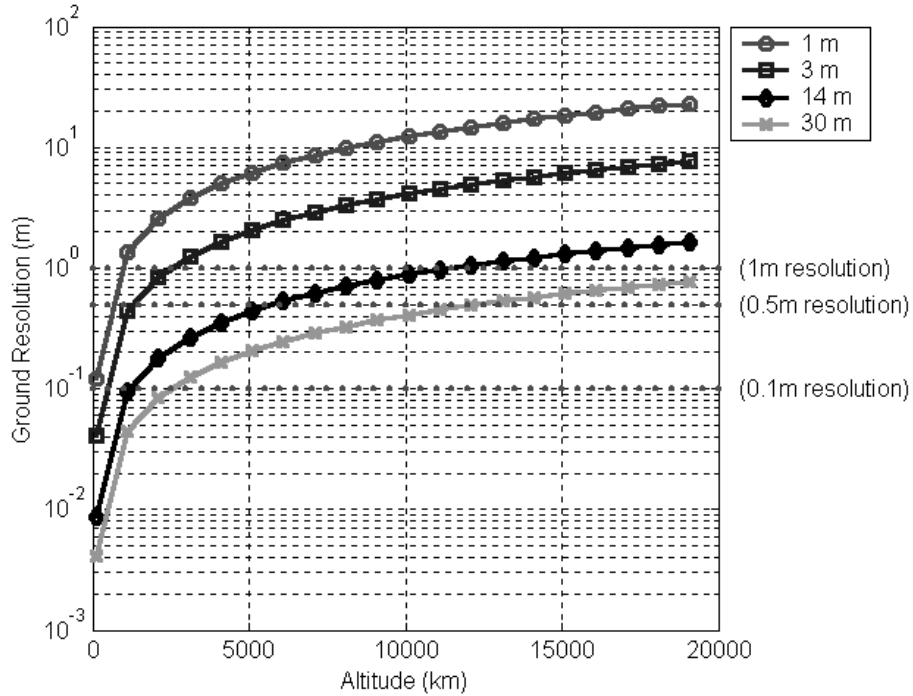


Figure 1.2 Effect of Aperture Size on Resolution (Alt. of 0-20,000km).

A Low Earth Orbit (LEO) satellite is generally defined as those satellites orbiting close to the earth, usually from less than 1,000 km. A medium-earth orbit (MEO) satellite ranges from about 10,000 to 20,000 km. A geosynchronous earth orbit (GEO), above 20,000 km, is an orbit with approximately the same period of the earth and are nearly stationary over a particular point on the earth. If the aperture size is kept constant, the resolution achieved deteriorates with an increase in altitude.

However, as can be seen in Figure 1.3, using an aperture of 30 meters at 1000 km orbital altitude still gives better than .1 meter ground resolution. This would greatly enhance our capability and due to the increase in altitude, the coverage area would be significantly increased. It can be seen from Figure 1.3, that inflatables

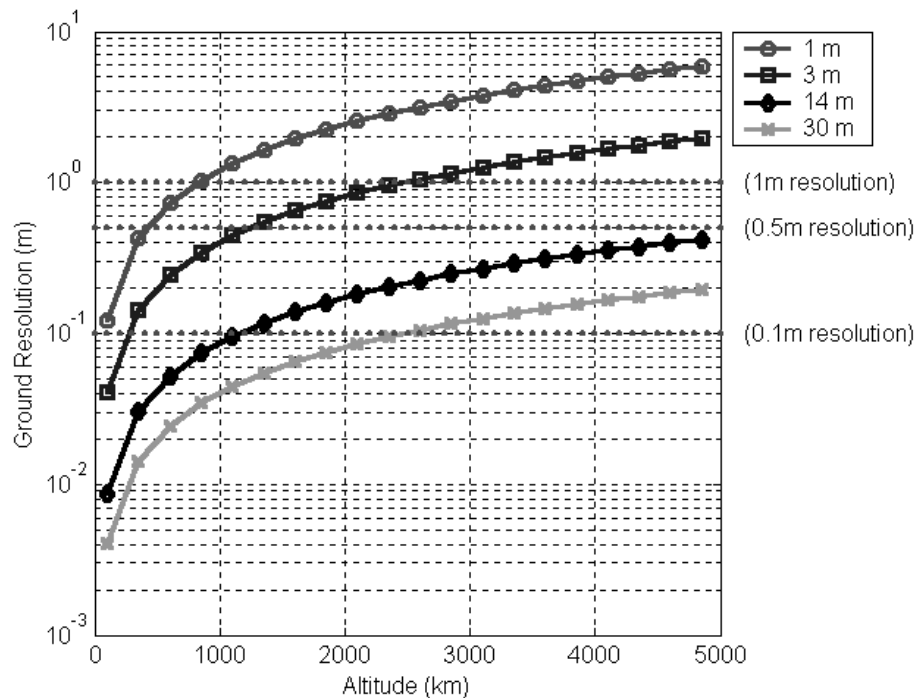


Figure 1.3 Effect of Aperture Size on Resolution (Alt. of 0-5000km).

could easily be orbited at altitudes of 1,000 to 5,000 km to achieve the desired ground resolution. Using commercially available program Satellite Toolkit (STK),

a sample is provided below. Two scenarios are demonstrated, a current technology satellite at 200 km (designated LEOSAT), and an inflatable satellite (designated MEOSAT) at 5,000 km. Using a 93 degree inclination, and assuming a desired .25 meter ground resolution, the LEOSAT has an aperture of 1.5 meters and is in a circular orbit of 200 km. The MEOSAT has a 30 meter aperture and is slightly elliptical with a perigee at 300 km and an apogee at 5,000 km. Figure 1.4 shows a three dimensional model of the earth with the orbital paths shown, as well as the “look-down” coverage area shown by the cone. Figure 1.5 shows a two dimensional map of the world with a representative coverage area shown on the ground. STK

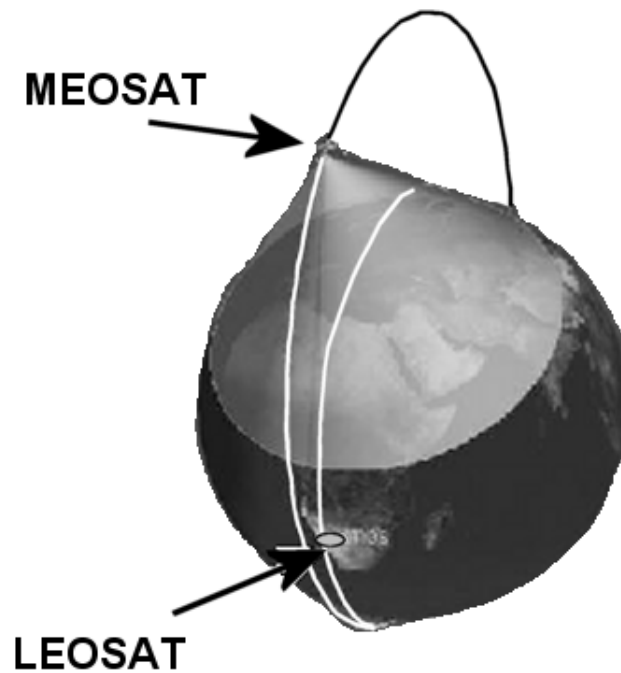


Figure 1.4 Sample Satellite Coverage (STK-VO)

provided a report with the following coverage for each satellite.

It can be seen that the average coverage of the LEOSAT is 1.6% of the earth’s surface and 14.20% for the MEOSAT, a significant increase! Assuming the fact that the Air Force would like to have less than a .2 meter ground resolution, a nominal altitude of 5,000 km could be used for an ISR satellite. Using just 7 satellites,

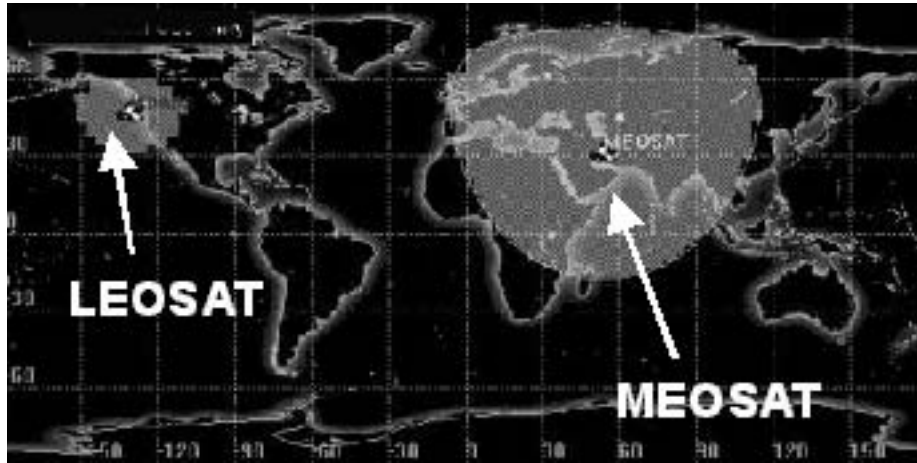


Figure 1.5 Sample Worldwide Satellite Coverage (STK)

Table 1.1 Satellite Coverage of the Earth Surface

Satellite	Min % Coverage	Max % Coverage	Average % Coverage	Accumulated % Coverage
LEOSAT	1.42	1.73	1.60	100
MEOSAT	1.63	21.79	14.20	100

approximately 99% of the surface of the earth could be covered, giving the Air Force much greater surveillance capability.

One of the first steps in building a satellite, is the design of the structure/beams that will be used. The purpose of this thesis is to help develop the technology for the next generation of space structures that will be larger, less expensive, lighter, and be able to deploy large optical membranes. AFIT has developed the Rigidized Inflatable Get-Away Special Experiment (RIGEX) to determine the vibration characteristics of an inflatable, rigidized beam in zero-g. This research focused on vibration testing on the ground in order to realize a significant cost savings for inflatable satellites in the future. The vibration characteristics were analyzed, and a beam model was used for the bending modes to predict the properties of the inflatable beams on the ground.

1.2 Scope of Project

The Rigidized Inflatable GAS Experiment (RIGEX) project is a NASA Get-Away-Special (GAS) experiment. The GAS experiments are self-contained experiments that are mounted in the Space Shuttle cargo bay. The RIGEX project will provide on-orbit data on the inflation, rigidization, and excitation of several beams. The experiment will return to Earth where further testing and analysis will be performed to verify that the ground-based testing and predictions are accurate and what improvements, if any, need to be made to the existing models. Figure 1.6.

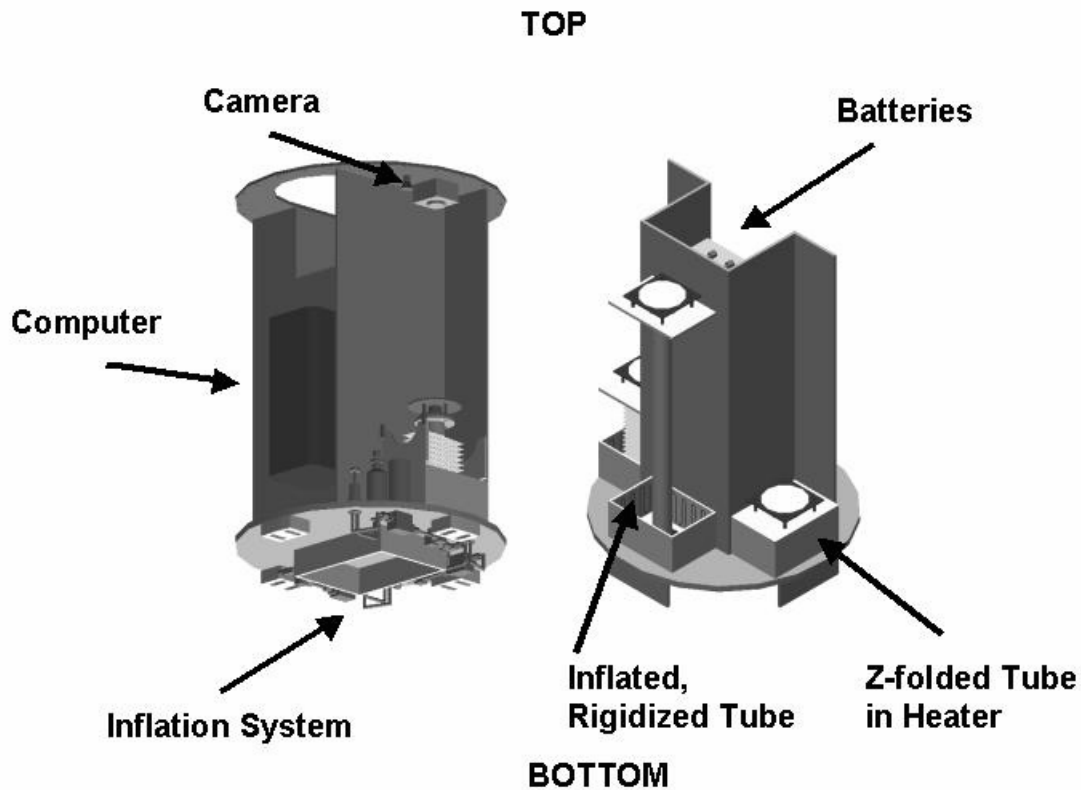


Figure 1.6 The proposed RIGEX Space Shuttle Experiment

This research is a continuation of the RIGEX project started by Captain John DiSebastion[13] at AFIT in 2000. Captain DiSebastion completed the preliminary design of RIGEX using systems engineering. The ultimate objective of RIGEX is to enable the application of large, inflated, rigidized space structures for operational

ISR systems. This research is limited to the vibration analysis of the ground testing portion of the experiment. The ground testing will form the basis from which predictions and verifications will be made as to how the beams will perform on-orbit.

1.3 RIGEX Background

The first work on RIGEX was the preliminary design, accomplished in 2001.[13] The RIGEX project will provide on-orbit data on the controlled inflation, rigidization, and structural analysis of several identical beam structures. Once the data is collected on the Space Shuttle, the entire experiment will return to Earth where further testing and flight analysis will be performed. Appendix A has the detailed drawings of the flight experiment, including the subsystems. The following mission statement was developed by AFIT for the RIGEX project[13]:

To verify and validate ground testing of inflation and rigidization methods for inflatable space structures against a zero-gravity space environment.

The primary objective of the preliminary design was the development of an experiment to collect data on rigidized space structures[13]. The secondary objective of implementing systems engineering principles into the experiment's design was also accomplished. If the vibration testing and modal analysis cannot be accomplished on the ground, the RIGEX project will have to be re-designed. Therefore, this initial experimental vibration testing is critical to the future success of the project.

1.4 Research Objectives

Given the mission statement for the RIGEX project, the following primary and secondary objectives were developed for the experimental vibration testing on the ground:

Primary Objective:

- *To perform vibration analysis on ground testing of the rigidized inflatable beams by identifying the natural frequencies, damping ratios, and the bending modes.*

Secondary Objectives:

- *To examine the analytic beam to determine its validity for the rigidized inflatable beams.*
- *To determine what parameters are important to the vibration characteristics of the rigidized inflatable beams.*

The research involves the ground testing portion of several inflatable struts and to determine how accurately a simple cantilever beam analytic model matches the test data. It is hoped that the properties of the beams will be accurately captured and the data will be used with the future flight test data to create an accurate analytic model to predict performance in space. For the purpose of this study, the “beam” refers to the tube with the two end-flanges as shown in Figure 1.7.

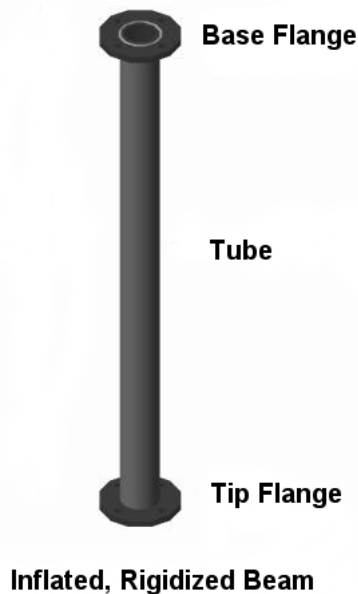


Figure 1.7 Inflatable Beam

1.5 Assumptions/Constraints

NASA regulations and limitations for the Get-Away-Special experiment have placed several constraints on RIGEX. The only constraints that are pertinent to ground testing is that the overall height of the canister is 28.25 inches; therefore, the beam was limited to a length of 20 inches.

The ground testing will be limited to the beams that were purchased from the L'Garde Corporation. Although the beams were manufactured from the same batch, there are many inconsistencies in the beams. For the experiments, it will be assumed that the beams are identical in material properties and physical description and that there are no physical imperfections. This study will be limited to just looking at bending modes. Preliminary tests on the beams showed that they behaved non-linearly above the first couple of low frequency bending modes; consequently, only the linear first bending modes will be considered. The temperature and internal pressure will also be assumed to be constant throughout the testing. The feedback and noise from the test equipment was minimal, except as where stated later.

The beams are fairly rigid and stiff, and the bending from the excitation will be small. Therefore, it will be assumed that no wrinkles will form in the beams and that the effects due to wrinkling of the material can be neglected. The beams will be folded for the flight test experiment; however, the beams that will be used for this study will not be folded and the effects due to the folding process and inflation are not considered here in.

1.6 Methodology

There are many factors which can influence the vibrational properties of a space structure. The number of components, mass, structural stiffness, coupling locations, space environment factors changing all of the above, to name a few. For the limited focus of this research, the only factors to be considered are changing pressure (internal and external), temperature, orientation, and excitation level.

The goal of the experiments is to be able to model the inflatable beams on the ground and be able to predict how they will perform in the zero-g, vacuum of space. In order to do this, the ground testing attempted to capture as many of the vibrational properties of the rigidized beams as possible. The ground testing utilized a shaker for the initial testing. Tests were conducted in ambient conditions on a damped vibrational testing table. Various forcing levels were used, as well as varying pressures in the beams. Piezoelectric Transducers were mounted on one of the short beams and used for excitation. The signals from an accelerometer (placed in the tip flange of the beam) and a reference signal (which changed depending on the test configuration) were used to generate a transfer function. A laser vibrometer was also utilized to collect the mobility transfer function. Additional testing was accomplished in a vacuum chamber using the PZTs for excitation. Additional tests were conducted by placing the beams inside of a heater canister in the vacuum chamber and were heated to approximately $95^{\circ}C$. This experimental work was accomplished in the AFIT Vibrations Laboratory.

1.7 Summary of Thesis

In the following chapters, vibration analysis of the ground testing for RIGEX is presented. In Chapter 2, recent research material and a simple dynamic modal analysis model are summarized. Recent advances in inflatable structures and relevant experimental tests are briefly discussed. The experimental setup and procedure is discussed in Chapter 3. The test procedure for the ambient and vacuum tests are outlined.

Chapter 4 presents the experimental results and analysis. The first tests in ambient conditions are shown, followed by the vacuum tests. A discussion of the results is made in Chapter 5. A summary and recommendations for further research are provided in Chapter 6.

II. Literature Review

2.1 Overview

The first studies on inflatable structures for use in space began in the 1960's. There have been several studies done on their properties, inflation, uses, etc.. Some relevant research is presented. Research accomplished by Dr. John Main[30] on inflatable space structures is particularly relevant. The equations of motion for a cantilever beam model are developed for analytic comparison of the test data.

2.2 Gossamer Spacecraft

The Goodyear Corporation was one of the early pioneers associated with the development of inflatable, deployable structures. Goodyear developed structural concepts, in the 1950s to 1960s for a search radar antenna, a radar calibration sphere, and a lenticular inflatable parabolic reflector[26]. Their collaboration with NASA resulted in the Echo balloon being flown in 1960. Echo I was made from a large number of mylar gores that were very thin and coated with a vapor-deposited aluminum, which was bonded together to form a sphere. The sphere was inflated on orbit, and the pressure was vented. The balloon kept its rigidized shape. This was the first large-size, high-precision, operational inflation space structure on orbit. L'Garde, Inc. has also been a pioneer in the development, application, and orbital demonstration of inflatable space structures technology for 30 years. L'Garde successfully flew a large number of reentry vehicle decoys. Their most notable demonstration was the IN-STEP Inflatable Antenna Experiment (IAE) conducted with NASA in 1996. The inflatable structure was comprised of two basic elements: the inflatable reflector assembly and the torus/strut support structure. The experiment was successfully flown on the recoverable Spartan spacecraft. L'Garde built the structure for about a million dollars and was able to stow the package in about the size of a desk. The inflated structure was 14 by 28 meters. This was the first large-size inflat-



Figure 2.1 IRSS packaged

able reflector structure deployed on orbit[26]. Figure 2.1(from the L'Garde website: www.lgarde.com) shows the stored configuration of the Inflatable Rigidized Space Structure. The figure following (also from the L'Garde website, is after the truss system has been inflated.



Figure 2.2 L'Garde Inflatable Truss

A third company making advances in inflatables is ILC Dover. They have experience in high technology inflatable ground structures, astronaut spacesuits, the

Mars Pathfinder landing airbags, the Next Generation Space Telescope (NGST), and many others. ILC Dover developed the technology for building a 3 by 10 meter inflatable deployable rigidizable solar-array system[26]. An inflatable solar-array system being developed by L'Garde is shown in Figure 2.3[26] The mechanical systems that

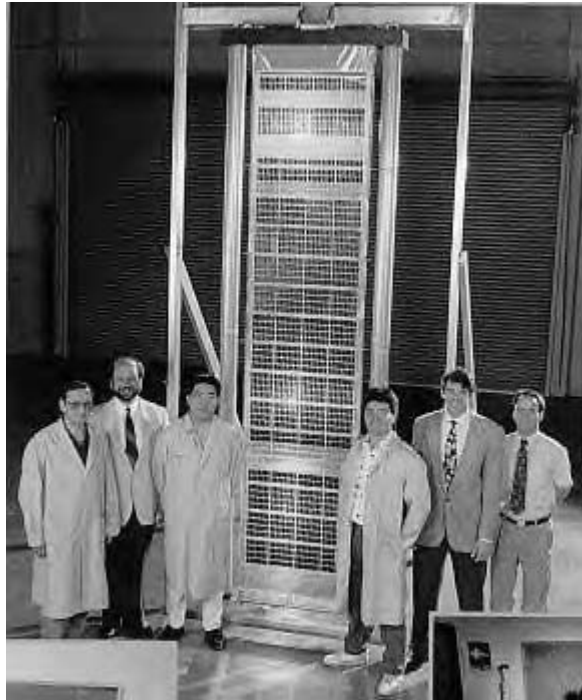


Figure 2.3 L'Garde Inflatable Strut Solar Panel

unfurl solar panels often have problems in the deployment sequence. If the solar panels do not fully deploy, a satellite could quickly become useless to its users. It's thought that inflatables will be able to be made much more reliably so that there will be fewer problems on orbit.

There are many applications for inflatables currently being developed. Applications such as solar arrays, communication systems, human habitats, planetary surface exploration, radar and reflective arrays, solar concentrators, solar shades, and many more[26]. However, there are many obstacles to their being used operationally, such as their rigidization, inflation, and control of their vibration and damping. They must also be able to have a long enough operational lifetime in

space where radiation, solar pressure, and many other factors are important. The rigidization and inflation techniques are still being developed. It will be important to have inflatable space structures as stiff as possible and to control their motion if possible while on orbit and this thesis is focused on this last factor.

2.3 Vibration and Modal Testing Theory

Vibration is the study of the repetitive motion of objects relative to a stationary frame of reference.[25] The vibrational properties of devices are often the limiting factors in their performance. In large space-based optical membrane devices, this is especially important. It is important that the vibration levels encountered be anticipated and brought under control.

Vibrations occur because of the interaction between potential and kinetic energy. A vibrating system must have a component that stores potential energy and releases it as kinetic energy in the form of motion (vibration) of a mass.[25] The motion of the mass then releases kinetic energy to the mechanism storing the potential energy. Structures can have many degrees of freedom and can become quite complicated. Vibrating systems are usually simplified by a simple system of masses connected by springs and dash pots or simple beam theory. The goal of vibration analysis is to be able to predict the response of a vibrating system. Therefore, it is necessary to derive the equations of motion and solve the differential equation(s). Figure 2.4 is a representation of a simple mass-spring-dash pot example. Assuming

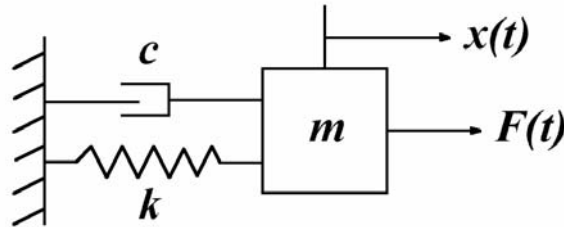


Figure 2.4 Single Degree of Freedom System

that the system only moves in the direction of the spring and that it does not exceed the linear range of the spring , this system can be represented by the equation:

$$m\ddot{x} + c\dot{x} + kx = F(t) \quad (2.1)$$

where m represents the mass, c is the damping coefficient, and k is the stiffness coefficient, \ddot{x} denotes the acceleration, or the second time derivative of the displacement, \dot{x} denotes the velocity or first time derivative of the displacement, x is the displacement, and F(t) is some input forcing function driving the system.

It has been shown [25:5] that for a periodic function $F(t)$, the motion $x(t)$ can be described by the equation

$$x(t) = A\sin(\omega_n t + \phi) \quad (2.2)$$

where A is the amplitude or maximum value of the function, and ϕ is the phase which determines the initial value of the function. The constant ω_n is used to represent the frequency at which the motion of a system repeats itself, and is called the *natural frequency*. The relationship between frequency, mass, and stiffness is[25]

$$\omega_n = \sqrt{\frac{k}{m}} \quad (2.3)$$

the frequency in hertz (Hz), denoted by f_n , is related to the frequency in radians per second by

$$f_n = \frac{\omega_n}{2\pi} \quad (2.4)$$

It is convenient to define the critical damping coefficient, c_{cr} , by

$$c_{cr} = 2m\omega_n = 2\sqrt{km} \quad (2.5)$$

Furthermore, the non-dimensional number ζ (zeta), called the damping ratio, is a function of the damping coefficient, mass, and the natural frequency. It has the following relationship:

$$\zeta = \frac{c}{c_c r} = \frac{c}{2m\omega_n} = \frac{c}{2\sqrt{km}} \quad (2.6)$$

With damping, the damped natural frequency ω_d is

$$\omega_d = \omega_n \sqrt{1 - \zeta^2} \quad (2.7)$$

Equation 2.1 can now be rewritten in a form that is called mass normalized as follows:

$$\ddot{x} + 2\zeta\omega_n\dot{x} + \omega_n^2 x = f(t) \quad (2.8)$$

where $f(t) = F/m$

The same type of modelling can be applied for a system consisting of a beam as shown below in Figure 2.5.

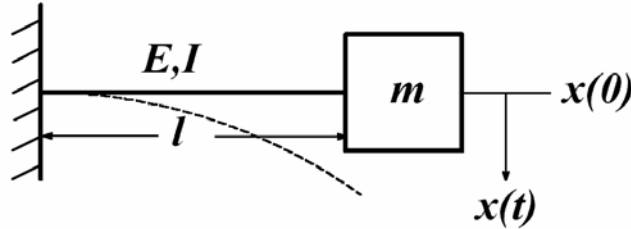


Figure 2.5 Single Degree of Freedom System - Beam Bending

The solution for the above system, which is a Single-Degree-of-Freedom, undamped system response to a harmonic excitation,[25:210] becomes

$$m\ddot{x} + kx = F\cos\omega t \quad x(0) = x_0, \quad (2.9)$$

$$\dot{x}(0) = v_0 \quad (2.10)$$

has the solution:

$$x(t) = \frac{v_0}{\omega_n} \sin \omega_n t + \left(x_0 - \frac{f_0}{\omega_n^2 - \omega^2}\right) \cos \omega_n t + \frac{f_0}{\omega_n^2 - \omega^2} \cos \omega t \quad (2.11)$$

where $f_0 = F_0/m$, and $\omega_n = \sqrt{k/m}$, and x_0 and v_0 are initial conditions.

2.4 Frequency Response Method

Euler's formula for trigonometric functions relates the exponential function to harmonic motion by the complex relation

$$Ae^{(j\omega t)} = A \cos \omega t + (A \sin \omega t)j \quad (2.12)$$

where $j = \sqrt{-1}$. Therefore, $Ae^{j\omega t}$ is a complex function with a real part of $A \cos \omega t$ and an imaginary part of $A \sin \omega t$. $Ae^{j\omega t}$ represents a harmonic function and can be used to describe a forced harmonic motion as the complex equation

$$m\ddot{x}(t) + c\dot{x}(t) + kx(t) = F_0 e^{j\omega t} \quad (2.13)$$

The real part of the complex solution corresponds to the physical solution $x(t)$. By assuming that the complex particular solution of the equation above is of the exponential form

$$x_p(t) = X e^{j\omega t} \quad (2.14)$$

where X is a complex constant that must be determined. Substituting yields

$$(-\omega^2 m + cj\omega + k)X e^{j\omega t} = F_0 e^{j\omega t} \quad (2.15)$$

The term $e^{j\omega t}$ can be cancelled because it will never be zero.[25] Consequently, the expression above can be rewritten as

$$X = \frac{F_0}{(k - \omega^2 m) + (c\omega)j} = H(j\omega)F_0 \quad (2.16)$$

The term $H(j\omega)$ can now be defined as the *frequency response function (FRF)* as follows

$$H(j\omega) = \frac{1}{(k - \omega^2 m) + (c\omega)j} \quad (2.17)$$

Rearranging the equations yields the following solutions

$$X = \frac{F_0}{[(k - \omega^2 m)^2 + (c\omega)^2]^{1/2}} e^{-j\theta} \quad (2.18)$$

where

$$\theta = \tan^{-1} \frac{c\omega}{(k - \omega^2 m)} \quad (2.19)$$

Substituting the value for X into the equation yields the solution

$$x_p(t) = \frac{F_0}{[(k - \omega^2 m)^2 + (c\omega)^2]^{1/2}} e^{-j(\omega t - \theta)} \quad (2.20)$$

Using the Laplace transform to solve the frequency response function defined above, yields

$$(ms^2 + cs + k)X(s) = F(s) \quad (2.21)$$

where $F(s)$ denotes the Laplace transform of the driving function. This equation can be manipulated to yield

$$\frac{X(s)}{F(s)} = \frac{1}{ms^2 + cs + k} = H(s) \quad (2.22)$$

The ratio of the Laplace transform of the output (response) to the Laplace transform of the input (driving force) for the case of zero initial conditions is denoted $H(s)$ and

is called the transfer function of the system. Since the Laplace transform variable s is a complex number, i.e., $s = j\omega$, the transfer function becomes

$$H(j\omega) = \frac{1}{k - m\omega^2 + c\omega j} \quad (2.23)$$

It can be clearly seen that the frequency response function of the system is the transfer function of the system evaluated along $s = j\omega$ [25]. The transfer function for set of experimental data will be used for the vibration analysis in determining the natural frequencies and damping ratios.

2.5 Dynamic Analysis of Inflated Beam Structures

2.5.1 Previous Inflatable Beam Experimental Results. There has been research conducted on inflatable structures and how to model them since the 1960's. NASA and others conducted research on inflatables in the early years of the space program in order to minimize weight and maximize capability. Of particular interest is work being done on the design and analysis of inflatable space structures by John Main. In Main's work [28], the theory on the relationship of inflatable beams and how wrinkling in the material effects damping is developed. One application that he looked at was an astronaut's space flight suit glove. The fingers of the gloves can be looked at as a simplified inflatable, cantilever beam. Main[28:83] used soft fabric beams for his model and work, not the rigidized beams of this study, however, the simplifying assumptions and model prediction should still be valid.

2.5.2 A Dynamic Analysis of Inflated Beam Structures. The focus of Main's investigation [29] was to determine the damping mechanisms active in structures constructed from inflated cylindrical beams, develop a practical modeling method for complex structures, and examine the difficulties in predicting 0-G dynamic behavior from ground tests. An Euler-Bernoulli model of the inflated beam was used to determine the distributed damping coefficients from modal tests. A

comparison of the modal ground tests and of testing aboard the NASA KC-135 low gravity simulator aircraft were made.[29]

Main et al.[28] developed a method of inflated beam analysis by modeling an inflated cantilever beam with the nonlinear wrinkling behavior of the fabric accounted for by assuming that the beam material could carry no load when the longitudinal stress in the beam dropped below zero. This model results in a differential equation of bending for the beam that is identical to the Euler-Bernoulli solution if the fabric modulus (longitudinal direction) (E_l), is expressed in units of load per unit width, and the beam fabric is not wrinkled:

$$\frac{d^2y}{dx^2} = \frac{M(x)}{E_l I} \quad (2.24)$$

where r is the beam radius, ν the Poisson's ratio, $\frac{d^2y}{dx^2}$ is the beam curvature, M is the applied moment, and $I = \pi r^3$. [29:1035]

Main's work[29] supports the approximation that elastic beam flexural modes can be used to estimate the lower natural frequencies of the inflated beam. It is unclear however, what the specific mechanisms are that govern the damping of the beams.

Possible sources of damping in the inflated beam include viscous damping from moving through the outside air, viscous damping from motion and compression in the enclosed gas, and damping from the stretching of the beam fabric. Clough and Penzin[6] developed a dynamic beam model from Euler-Bernoulli beam theory that includes two damping mechanisms, a purely viscous damping term and a longitudinal strain rate damping term. The partial differential equation that was developed to describe the flexural vibration of the beam is

$$\mu \frac{\partial^2 y(x, t)}{\partial t^2} + EI \frac{\partial^4 y(x, t)}{\partial x^4} + C_s I \frac{\partial^5 y(x, t)}{\partial x^4 \partial t} + C \frac{\partial y(x, t)}{\partial t} = P(x, t) \quad (2.25)$$

where μ is the beam mass per unit length, $y(x,t)$ the beam displacement as a function of position and time, E the modulus, I the moment of inertia, C_S the strain rate damping coefficient, C the viscous damping coefficient, and P the distributed load.[29]

A method was developed by Cudney and Inman[11] to fit the distributed damping coefficients in the model above to experimentally determined natural frequencies and modal damping ratios. The relationship developed between the experimentally determined and model parameters is

$$2\zeta_n\omega_n\mu = C + C_S I\beta_n^4 \quad (2.26)$$

where ζ_n is the modal damping of the n th mode, ω_n the natural frequency, I the beam moment of inertia, and β_n the cantilever beam theoretical eigenvalue for the n th mode. The distributed damping parameters are found by determining experimentally the natural frequencies and modal damping ratios (ω_n and ζ_n) over a range of modes. The equation is then put in X-Y form with the X values being $I\beta_n^4$ and the Y values being $2\zeta_n\omega_n\mu$. The moment of inertia I is defined above, and the eigenvalues for various beam boundary conditions are known analytically. A least-squares regression is performed on the set of points, yielding the viscous damping coefficient (C) as the Y intercept, and the strain rate damping coefficient (C_S) as the slope.

To use in the above equations for the modulus, the material properties of the beam fabric from experimental data can also be estimated. The effective material modulus can be determined for each mode of vibration from the following expression:[29:1036]

$$E_n = \frac{\mu l^4 \omega_n^2}{I\beta_n^4} \quad (2.27)$$

One of the difficulties of characterizing the damping behavior of the 1st mode is likely due to the low frequency and high damping. Because of the high modal damping, the beam may not be vibrating long enough in the 1st mode to be fully

Table 2.1 Summary of Main's Omega and Zeta values

Mode	Theoretical β_i	5 cm (4psi)	
		Omega (Hz)	Zeta(%)
1	1.875	6.26	0.09
2	4.694	42.72	0.08
3	7.855	121.6	0.17

characterized. It has been noted that modal damping ratios are historically very difficult parameters to estimate.[29:1038] For Main's tests, it was found that at low transverse fabric stress levels (small radius, low pressure), that the fabric behaves viscoelastically. It appears to stiffen as the frequency increases. This was expected because creep behavior was exhibited by the fabrics in the static tests. It was found however, that as the transverse hoop stress (pr) in the fabric increases, the fabric begins to exhibit rate softening behavior. The specific mechanism for this rate softening was not determined.[29:1039] Shown in Table 2.1 are the natural frequencies, damping ratios from the experiments, and the eigenvalues (β_i) for a 5cm diameter beam. The beams used by Main did not have a tip flange/mass, and they were made of a rubber-like material. It is expected that using the stiffer, rigidized beams with a tip flange, that the natural frequencies will shift to higher frequencies.

Large differences were found between the modal damping parameters measured in the 0-G and 1-G tests. In the tests of the 5-cm beam and the inflated solar concentrator, the damping was significantly higher in the 0-G tests than in the 1-G tests. However, this was not shown for the 8-cm beam test. The authors propose that perhaps the 5-cm beam experienced some wrinkling, whereas the 8-cm beam was stiff enough that it did not.[29:1042-43]

There are different factors that effected the damping of the beams. Viscous damping was expected to be higher in the 1-G tests because of the differences in air density between the 1-G ground tests and the 0-G tests in the aircraft. The viscous damping term reflects the air mass moved during each cycle and the mass is a function of the air density. In the aircraft at altitude, there is approximately

40% less air than at sea level. The difference in the mass of air moved helped cause the damping in the 8-cm beam to be higher in the 1-G tests than in the 0-G tests. A second effect that added to the damping in the 1-G tests was the stress in the fabric of the 8-cm beam. In the 0-G tests, the only forces acting on the fabric were pressurization forces, so the stress was very uniform. In the 1-G tests, the beam was hung horizontally. The weight of the beam itself caused the beam to bend. In the 0-G tests, the beams remained unwrinkled. Therefore, the decreased stress on the bottom of the fabric beam caused a contribution to the increased damping in the 1-G tests.[29:1043]

The authors found that the strain rate damping in the fabric did increase as the stress in the fabric decreases, but once the stress in the fabric dropped below the wrinkling point, those regions no longer contributed to the structural damping at all. The significant result of the tests is that even the slight geometry changes between the 1-G and 0-G tests had a dramatic effect on the system damping, especially if the geometry changes were significant enough to cause wrinkling in the fabric. When the fabric wrinkled, the effect was to reduce overall system damping. One result of the dynamic tests that was not expected was the internal pressurization level of the beam had no discernible effect on the beam damping. Beam damping appeared to arise principally from the motion of the beam through the outside air and the stretching of the beam fabric as the beam deformed.[29:1044]

The results of the experiments showed that ground tests can result in estimates of damping ratios that are high because of effects of the atmosphere on viscous damping. Ground tests can also result in damping estimates that are too high or too low due to the changes in the stress distribution in the fabric. Although these findings are important, the inflatable beams that will be used with RIGEX should be of a large enough diameter and sufficient stiffness that no wrinkling should occur. This should eliminate one of the major problems that Main encountered. However, it is still expected that viscous damping will be a major factor on the damping ratios.

2.5.3 Improved Beam-Bending Model for Inflatables. Continuing with his work, Main *et.al.* improved his model for beam-type bending of space-based inflated membrane structures. The value of the longitudinal stress resultant (N_l) in the beam fabric due to externally applied moments and the beam internal pressure is assumed to vary linearly across the beam thickness and is shown as follows from Equation 2.28 [30:122]

$$N_l = N_{l0}\left(\frac{1 + \cos\theta}{2}\right) + N_{lm}\left(\frac{1 - \cos\theta}{2}\right) \quad (2.28)$$

where N_{l0} and N_{lm} are the longitudinal stress resultants and θ is measured around the circumference of the beam from the point at which $N_l = N_{l0}$.

The differential equation of bending for the inflated beam can now be written as follows for both the unwrinkled and wrinkled stages of bending for the inflated beam element:

$$\frac{d^2y}{dx^2} = \frac{M}{E_l \pi R^3}, \text{ for } M < \frac{\pi p r^3}{2}(1 - 2\nu_l) \quad (2.29)$$

$$\frac{d^2y}{dx^2} = \frac{M - 2\nu_l p r^3 \sin\theta_0}{E_l r^3[(\pi - \theta_0) + \sin\theta_0 \cos\theta_0]}, \text{ for } M > \frac{\pi p r^3}{2}(1 - 2\nu_l) \quad (2.30)$$

The rigidized beams that will be used for RIGEX should not be susceptible to wrinkling, except during the heating and inflation phase. The beams will be tested after they are rigidized; therefore, wrinkling will assumed to be zero.

2.6 Summary

A short history and description of gossamer structures was presented in this chapter. Modal testing theory and the frequency response method were discussed. A dynamic analysis of inflated beam structures was reviewed. The research done by Main suggests that Euler-Bernoulli beam theory can be used for the bending modes.

The next chapter outlines the experimental methodology, test setup, and a beam theory analytic model will be developed and used as a comparison to the test data.

III. Experimental Methodology

The environmental challenges and high cost of conducting experiments in space drive the need for developing an analytic model that can predict how experiments on the ground (i.e. in gravity) will behave in the zero-g vacuum of space. The ultimate goal of the RIGEX project is to be able to develop an analytic model to predict how inflatable space structures will behave in space. Several steps are required to accomplish this. Experimental data will first be taken on the ground in ambient conditions, then in a vacuum, and finally on orbit in the Space Shuttle.

The purpose of this experimental testing is to determine the natural frequencies of vibration and the damping ratios at those frequencies on the ground. It is necessary to characterize the inflatable beams as fully as possible in order to be able to accurately build an analytic model. The initial tests were conducted in ambient conditions on a damped vibration testing table using a shaker for excitation. Comparisons were made on the trial repeatability, beam orientation, excitation level, pressure levels in the beam, temperature, and ambient and vacuum conditions. These comparisons determined the parameters important to the vibrational characteristics of the beams.

PZTs will be used for excitation in the flight tests that will be conducted in the future. Therefore, the second form of testing utilized Piezoelectric Transducers (PZTs) for excitation. The PZTs were used for excitation on the shaker, a test stand on the vibrations table, and they were used for testing in the vacuum chamber. The PZT tests on the test stand and in the vacuum were designed to determine repeatability of the experiment with the RIGEX equipment.

There are many challenges in determining the modal properties of the inflatable beams. The beams that were manufactured are thin shelled cylinders that are made of a 3-ply material that is made with a material that softens when heated and rigidizes when chilled. Vibration in the beams consist of many modes, such as bending,

torsional, and longitudinal. However, only the bending modes were considered for this research.

3.1 Inflatable Beams Description

The inflatable beams were constructed by the L'Garde Corporation of a proprietary carbon fiber 3-ply material which softens in heat and rigidizes in cold temperatures. The material was designated "L5" for identification by the company. The beams have a tip and base flange, as shown in Figure 3.1. The beam assembly is shown in the "Z" folded configuration and in the inflated configuration. The beams were manufactured by the L'Garde Corporation specifically for this experiment. L'Garde is still conducting research in the use of and manufacture of inflatable structures. As such, there are always difficulties with manufacturing new/experimental products. The beams average 20 inches in length (as measured from tip to base flange) and are roughly 1.5 inches in diameter. A detailed description of the material properties are shown in a later section in this chapter. The short beams have a length to diameter (L/D) of approximately 14. It is expected that future optical space structures will have struts with a very high length to diameter ratio in order to maximize the focal length and minimize the structure weight. Therefore, a set of beams having an approximate L/D ratio of 33 were also tested. The long beams were tested to see how the increase in L/D effected the results and if the natural frequencies were shifted to lower values. To keep the beams organized, a simple numbering system was devised. The short beams are numbered "S" 01-06, and the long beams are numbered "L" 01-03. In order to consistently keep the orientation of the centerline of the beams aligned with the z-axis, the base flange "thru" holes were numbered from one to four as shown in Figure 3.2. For the experiment, a specific orientation of the beam was specified for each test. The specified number was placed closest to the shaker, or facing towards the test stand. For example, S02-1 is short

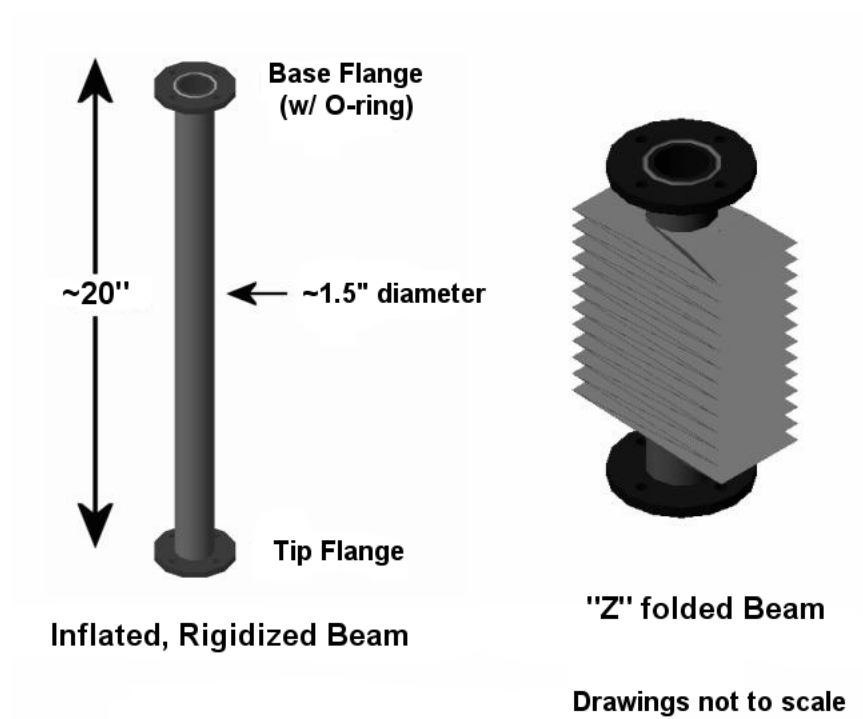


Figure 3.1 Diagram of Inflatable Beams (Short Beam)

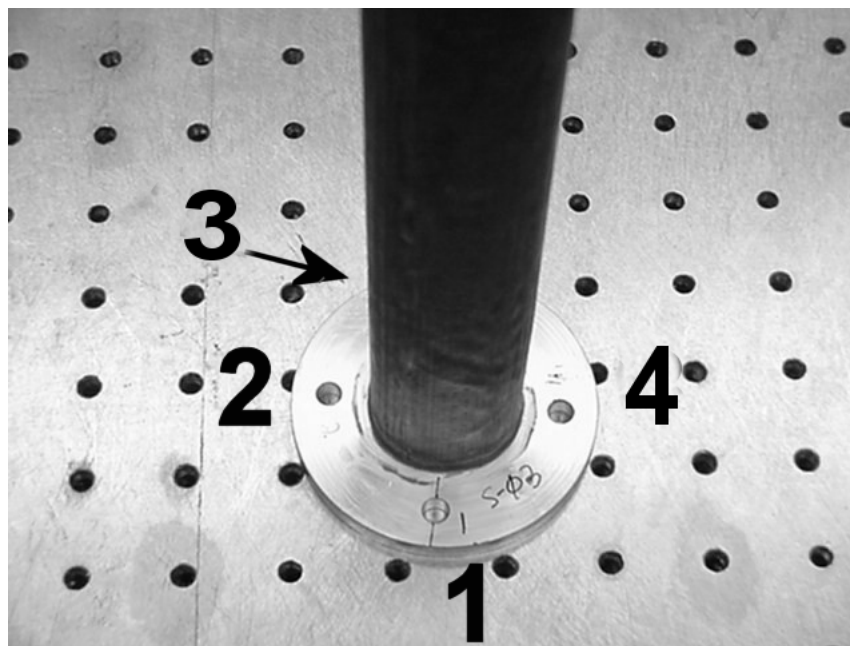


Figure 3.2 Diagram of Inflatable Beam Numbering

beam number 2, with the base flange hole number 1 bolted closest to the shaker arm on the base plate.

3.1.1 Beam Irregularities. The beams were inspected for quality and function before testing. Beams S01 and L02 were found to leak when pressurized and were not used in the experiment. The first problem discovered for the remaining beams were the base and tip flange surfaces not being parallel to each other, i.e. the beam was not mounted perfectly perpendicular on the flanges. Figure 3.3 shows four of the short beams aligned with the base flanges touching on the flat vibrations table. Figure 3.4 shows the difference in length, as well as the fact that the tip flanges are not touching like the base flanges are. The length of the beams varied; however,



Figure 3.3 Four of the short beams with the base flanges in line and touching.

due to the fact that they were not perpendicular, an average length of 20 inches was used for all of the beams. The actual length was $20 \pm 1/4$ of an inch. The beam length was reduced by the length of the tip flange inside the tube due to the fact



Figure 3.4 Close-up of the 4 short beams. Note the gap between the tip flanges.

that the bending would occur between the flange structures. All of this combined to effect the amount of the tip inertia and the the natural frequencies. This was taken into account in the analytic model by using an average value for the beam properties and neglecting the minor differences in the different beams.

The second, and most notable irregularity was the surface of the beams. The beam fabric had many irregularities and inconsistencies. Figure 3.5 shows just one example of the beam surfaces.

It was consistent for all of the beams that there were some irregularities. Overall, it can be said that beams S03 and L01 were the “smoothest” beams with the fewest irregularities. Beams S02, S05, S06, and L03 were in poor condition with many irregularities in the beam surface. Beam S04 had what appeared to be several “valleys” or areas of uneven distribution of the outer layer that ran most of the length of the beam. Figure 3.6 shows a comparison of a “smooth” beam surface and one with irregularities. Some photos were taken with “negative” lighting to enhance the surface features. Appendix B includes detailed pictures of the irregularities for all of the short beams.



Figure 3.5 Beam surface closeup of irregularities.

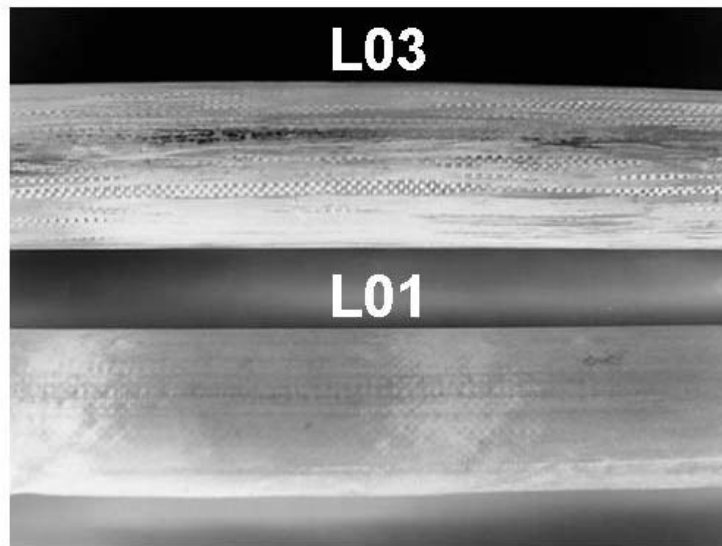


Figure 3.6 Surface comparison of smooth and irregular beam surface (Beams L01 and L03)

3.1.2 Material Properties. Due to the proprietary material used for the beams, not all of the material properties are known. Young's Modulus (E) was given as reasonable value from L'Garde. All of the beams have an average diameter of approximately 1.5 inches. A set of 6, 20 inch ("short") beams were purchased. A set of 3, 48 inch ("long") beams were also manufactured. Table 3.1 lists the material and equipment properties used for the experiment.

Table 3.1 Equipment Physical Properties

Property Description	Value	Units
PZT Mass	7.15	grams
PZT Width	2	inches
PZT Length	5 3/4	inches
Accelerometer Mass	8.34	grams
E-Z Clip Mass	1.55	grams
Aluminum Base Flange Mass	74.02	grams
Aluminum Tip Flange Mass	74.6	grams
Beam Material Thickness (H)	.015	inches
Young's Modulus (E)	9.5E(6)	lbf/in*sec ²
	1.69E(8)	N/m ²
Moment of Inertia (I)	8.275E(-9)	m ⁴
Material Density (ρ)	8.64307E(2)	kg/m ³

Table 3.2 lists the properties that were measured for the short beams. All of the short beams have an average beam length of 20 inches, or .508 meters and an average diameter of 1.5 inches, or .037 meters. Note that beam S01 was not used for the experiment due to a leak at the base flange. The long beams have an average length of 48 inches.

Table 3.2 Short Beam (2-3) Physical Properties

Property	S02	S03	S03 w/ PZT	Units
Beam Diameter (avg.)	1.55	1.57	.	inches
Total Beam Mass (M)	199.13	194.9	214.92	grams
Short Beam (4-6) Physical Properties				
Property	S04	S05	S06	Units
Beam Diameter (avg.)	1.42	1.53	1.38	inches
Total Beam Mass (M)	197.79	190.34	197.64	grams

Using Main's[28] assumption that $I = \pi r^3 H$ (moment of inertia) for the inflatable beams, results in an approximate value of $I = 8.275 \times 10^{-9} m^4$. Using I and an average length of 20 inches for the short beam and subtracting the length of the flanges in the tube (.75 inches) to determine the actual bending length of the beam, results in a tip inertia (J) of 0.171 kg/m^2 . Using an averaged length of 48 inches, the tip inertia (J) for the long beams was calculated as 1.057 kg/m^2 .

Table 3.3 Long Beam Physical Properties

Property Description	L01	L03	Units
Beam Diameter (AVG)	1.43	1.59	inches
Total Beam Mass (M)	245.02	247.25	grams

3.2 Experimental Procedure

The experimental procedure consists of three major areas. The first was conducting tests in ambient conditions using the shaker in order to characterize the modal properties of the beams. The shaker was used due to its ease of use and availability; however, it was determined later that it did create additional modes that complicated the analysis. The second set of tests used the PZTs for excitation. Since PZTs will be used on the flight test part of the experiment, it is necessary to determine how well the PZTs will work, and if valid data can be produced. The third portion is to compare the test data with an analytic prediction. Listed below are the steps that were taken to conduct the experiment.

1. Determine physical properties of test specimens and what equipment will be need and what/how experiments will need to be conducted.
2. Setup equipment for testing and data acquisition. Calibrate accelerometers and other equipment.
3. Develop an analytic model for the inflatable beam.
4. Conduct vibration testing in ambient conditions using the shaker mounted on the test stand:

- (a) Short Beams
- (b) Long Beams
- (c) Short Beam with PZT mounted

A short beam was then selected to have the PZTs mounted on it for further testing.

5. Conduct vibration testing using the PZTs for excitation on the shaker on the test stand.
6. Conduct vibration testing using the PZTs for excitation on the test stand.
7. Conduct vibration testing using the PZTs for excitation in the vacuum chamber in ambient pressure.
8. Conduct vibration testing using the PZTs for excitation in the vacuum chamber in a vacuum.
9. Conduct vibration testing using the PZTs for excitation in the vacuum chamber in a vacuum while heating to temperatures near that for inflation/folding of the beams.
10. Determine the modal properties (natural frequencies and damping ratios) using the Eigenstructure Realization Algorithm (ERA) and Polytec Scanning Vibrometer (PSV) software.
11. Determine what parameters effect the modal properties and identify the bending modes.
12. Compare the experimental natural frequencies to the analytic model.

The following sections will present the details of the equipment setup, the software tools used for analysis, the model development, and a test matrix showing what tests were performed on each beam. A short description of the program used to create the data for modal analysis is discussed. The last section presents an analytic model for the beams using the PZT for excitation. Chapter 4 will present

the results of the vibration testing and the modal analysis. Chapter 5 will present a discussion on the relationships determined from the modal analysis and comparison to the analytic model.

3.3 Experiment Equipment and Setup

To determine the natural frequencies and damping ratios, the inflatable beams were excited and measurements were taken using a tri-axial accelerometer located in the tip of the beam. A laser vibrometer was also be used. The signal data was processed in order to create a frequency response function (FRF) so that the required modal data could be determined.

A diagram of the experiment setup is shown in Figure 3.7. As shown in the diagram, a Windows 98 personal computer(PC) is used to control the experiment. The excitation signals are generated by a software program on the PC which sends the signal to a Hewlett Packard (HP) VXI Plug and Play system which is the interface between the computer and the rest of the experiment equipment. The output signal from the HP is sent through an amplifier, after which, the electronic signal is converted to a physical excitation by means of an Electro-Seis[®] Model 113-LA Shaker. The test structure undergoes a physical response which is measured via a tri-axial accelerometer on the tip of the beam. The accelerometer outputs a signal that is passed back to the computer via the HP system. The accelerometer mounted on the base of the shaker arm is passed through a PCB signal conditioner before it is passed to the HP system. BNC (Bayonet Neill-Concelman (the inventors), also referred to as coaxial cable) connectors were primarily used for the cabling and connectors from the various pieces of equipment. The same basic system is used for the testing in the vacuum chamber. A detailed description of the equipment and their setup is presented in the following sections.

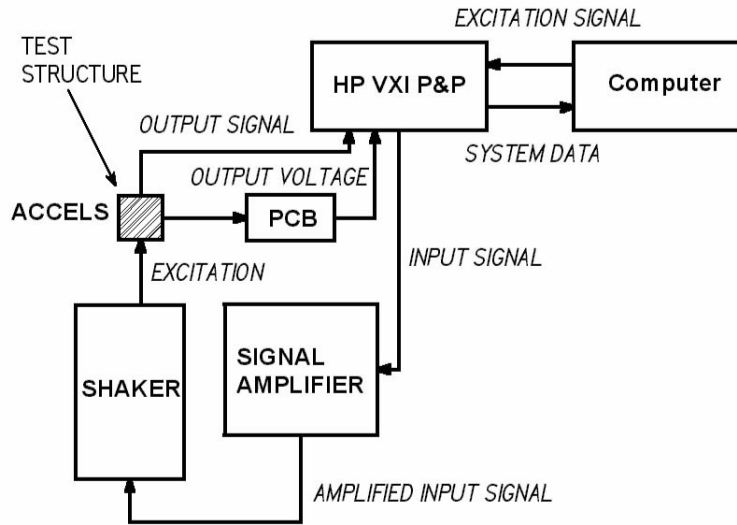


Figure 3.7 Experiment Setup

3.3.1 Data Acquisition. The initial testing used the HP system for data acquisition. The flight test will use a data acquisition card on the PC 104 computer. The testing on the HP system is the baseline system. Future research will compare the results of the ground system with the PC 104 acquisition system. Figure 3.8 shows the HP system. The user interface to the acquisition system is a program by Data Physics Corporation: *SignalCalc 620*. There are several test types that are available in SignalCalc, a Transfer Function test was used. Each beam was setup as a separate test. The X,Y, and Z direction signals from the accelerometer were connected to Channels 2, 3, and 4 of the HP 8 Channel input, ICP/Voltage board. The velocity signal from the laser vibrometer system was connected to Channel 5. The accelerometer, mounted on the arm of the shaker, was connected to Channel 8 and used as the reference signal for the transfer function (TF) or frequency response function (FRF). Figure 3.9 shows the graphical user interface (GUI) of the SignalCalc program. The program allows the various channels being recorded to be selected, as well as the sensitivity, and units to be input. Various generators can be used for the signal for driving the shaker and PZTs. The channel parameters must be defined.



Figure 3.8 Hewlett Packard System

The active channels being used, described above, were selected. The sensitivity of each channel was input after the equipment was calibrated. The calibration values are shown in a later section. The range in engineering units (EU) is entered, along with the sensitivity in mV/EU. The mV/EU is the sensitivity (millivolts/measured unit) of the sensor feeding the channel. The EU is specified for each channel. The accelerometer has units of acceleration (g), and the vibrometer units of velocity (m/s). The vibrometer sensitivity which is given as 25 per 1000 m/s, was converted to mV per EU as follows:

$$\begin{aligned}
 \text{conversion} &= \frac{1000mV}{\frac{25 \frac{m}{s}}{1000}} \\
 &= 40,000 \frac{mV}{m/s}
 \end{aligned}$$

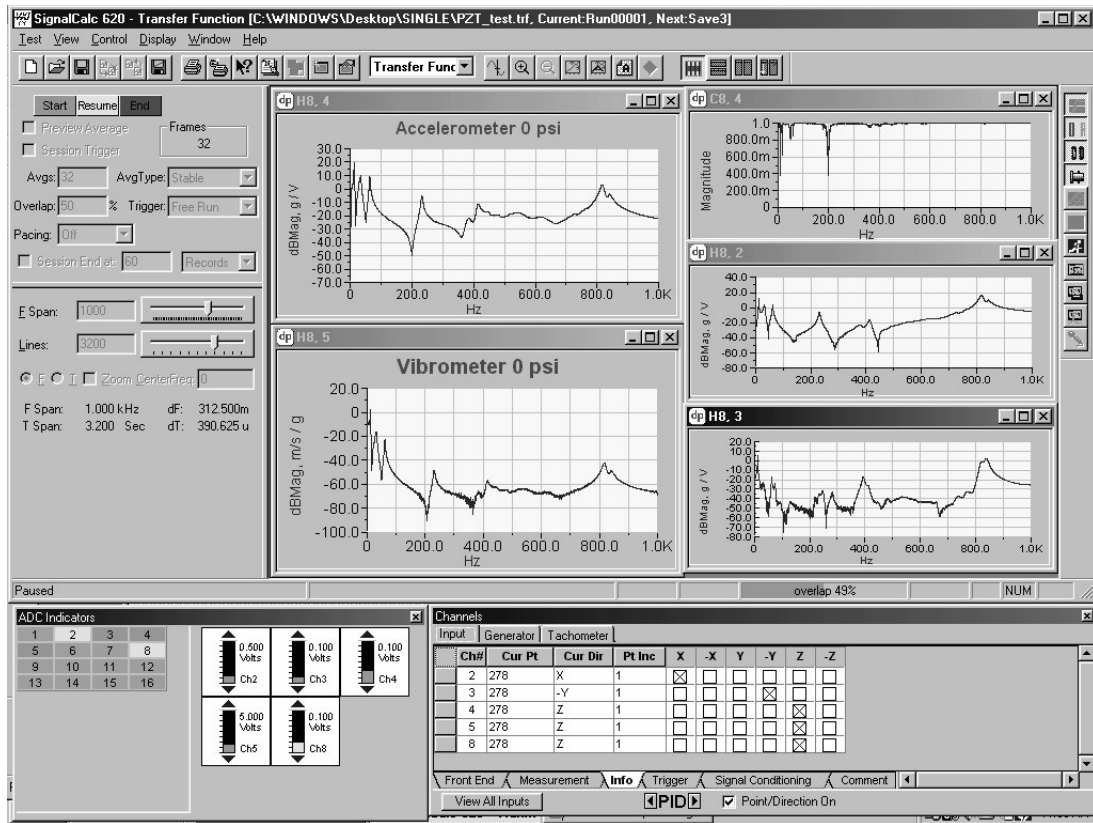


Figure 3.9 SignalCalc 620 Main GUI Screen

This conversion allowed the vibrometer units to be mV per EU (m/s). The direction (which axis) was recorded in the comment field.

The reference channel allows one input channel as the reference against which all other channels may be compared in the Transfer Function tests for creating the FRF and coherence results. For the shaker tests, an accelerometer was mounted on the end of the shaker arm, at the base of the beam, and was used as the reference channel because the entire beam is being displaced by the shaker arm. The PZT tests will use the signal from the HP system that is driving the PZT as the reference signal.

The conditioner type must also be specified as one of the channels parameter. Direct (used for the vibrometer) is used for a voltage input (direct wire from BNC to digitizer module input), and ICP (Integrated Circuit Piezoelectric® input

for accelerometers and other transducers with internal electronics. ICP provides a direct signal line from the BNC to the digitizer module but injects a 4 mA constant current source on the central pin conductor to power the transducer. The coupling must be specified, and AC rather than DC coupling was selected due to the system configuration.

In order to conduct the analysis of the signal data, a window, or “weighting function” is applied to the time-data prior to performing a fast fourier transform (FFT). A Hanning window is generally used for broadband signals, and was selected and used throughout the experiment.

The signal generator must be specified. Several signals were considered, a sine wave, random, burst random, and pseudorandom. The sine wave will allow a larger voltage when used with the PZTs, however, it did not produce “clean” results on the shaker. After some trial and error, the random signal was found to produce the best results with the least amount of noise. The amplitude of the excitation signal that was used is discussed in Chapter 4.

The measurement parameters used for the tests were consistent throughout the experiments. Since the data being collected has noise in it, averages of each sample time was used. Selecting “stable averaging” sums the selected number of constituents, weighting each with equal importance; the average is automatically normalized to the number of constituents currently acquired. Several different number of averages were tested, from 10 to 64. 32 averages was selected because it allowed enough time for the noise to be averaged out and provide a clean data sample; increasing the number of averages about 32 showed no significant improvement. SignalCalc allows an overlap to be used with the averages. The overlap field allows the maximum permissible overlap between frames averaged as a percentage of T_{span} , the frame length. Overlap when analyzing continuous signals allows recovery of the information lost due to the windowing process. A 50% overlap was selected, a common value that is used in testing.[12]

In order to conduct a test, there are several sampling parameters that must be specified. The following relationships are used in SignalCalc:

$$\begin{aligned} T_{span} &= Blocksize \times dT \\ F_{span} &= Lines \times dF \\ dF &= 1 \div T_{span} \\ Lines &= Blocksize \div 2.56 \end{aligned}$$

where,

- T_{span} : the time duration of each frame or capture window (seconds)
- F_{span} : the upper frequency of all computed spectra (Hz)
- dT : the time resolution: time difference between adjacent sample points (sec)
- dF : the nominal frequency resolution, the difference between adjacent frequency points (Hz)

Several frequency ranges were used during the experiments, ranging from 100 Hz to 1000 Hz. The equipment being used limits the most reliable range to approximately 200 Hz, and the bending modes of interest occur primarily under 300 Hz. However, it was of interest to sample out to 1000 Hz in order to characterize what the beam was doing at the higher frequencies. Most of the testing used a F_{span} of 1000 Hz, with 3200 lines being used, resulting in a T_{span} of 3.2 seconds, a dT of 0.00039062, and a dF of 0.3125 Hz. This provided a satisfactory level of resolution for data collection.

Using the *SignalCalc 620* program, the transfer function, coherence, and time history signals were saved for each signal, for each trial. The time history files were saved as ASCII text files designated as **Xx**, for example: Xxsv00001.txt. The last time-history of duration T_{span} with a resolution of dT as measured from channel X involved in the average. The (complex) transfer functions (or FRF) between process input **Xx** and process output **Xy** with resolution dF (frequency span), were saved as ASCII text files designated as **Hxy**: Hxysv00001.txt. Channel 8 (accelerometer

mounted on the shaker arm) is used for the reference channel, which is then compared to Channels 2,3,4, or 5. The transfer function would be created for Channels (8,2), (8,3), (8,4), or (8,5) for the acceleration in the X, Y, Z, and vibrometer velocity at a given point. The coherence function between inputs \mathbf{Xx} and \mathbf{Xy} over the duration T_{span} with a resolution dF was saved as \mathbf{Cx} : Cxysv00002.txt.[12] A routine was written in MATLAB® to convert the ASCII files into the MATLAB® .MAT file format.

3.3.2 Driver Description. To excite the beams for the modal testing, an APS Model 113 ELECTRO-SEIS Shaker was used. The Model 113 is a long stroke, electrodynamic shaker, to be used for exciting and studying the dynamic response characteristics of structures in the seismic frequency range. The unit employs a permanent magnet and is configured such that the armature coil remains in a uniform magnetic field over the entire stroke range. The drive power for the shaker is obtained from a low frequency power amplifier. An APS Model 124 DUAL-MODE Power

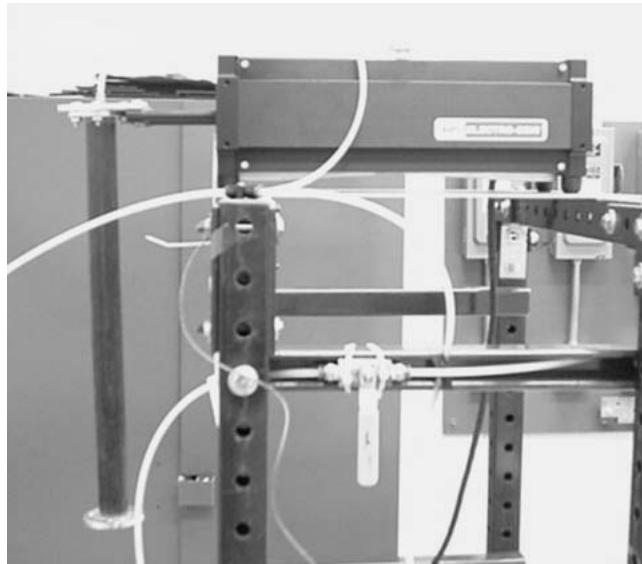


Figure 3.10 Electro-Seis® Model 113-LA Shaker with a Short Beam mounted.

Amplifier was used on the signal from the HP system before being sent to the shaker.

Figure 3.10 shows a short beam bolted to the shaker that was mounted on a test stand that was bolted to the table.

The effective linear frequency range for the shaker is 0-200 Hz. The first couple of bending modes should be within this frequency range. However, test data will be taken from 0 - 1kHz. Although the force and velocity envelope will drop off significantly above 200 Hz, test data was able to be collected, although its accuracy should be view with some skepticism. However, it was found that exciting to 1kHz did not cause a significant degradation of the data collected.

The laser vibrometer was used on the shaker with a beam mounted on the arm. The laser point was place on the center of the beam flange that was attached to the baseplate. The APS Model 124 DUAL-MODE Power Amplifier was set on both voltage and current with the following results.

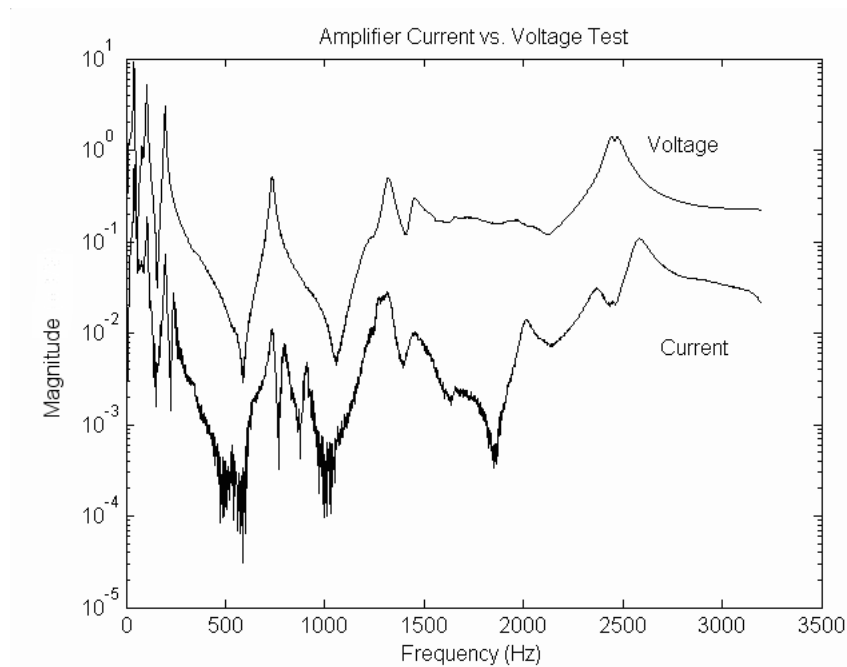


Figure 3.11 FRF of Amplifier Test on S02

It can be seen from Figure 3.11 that the FRF (of a short beam) of the current plot drops off much faster than the voltage source. The voltage plot also is much

cleaner, i.e. with very little noise. Therefore, the voltage selection was used for the power amplifier.

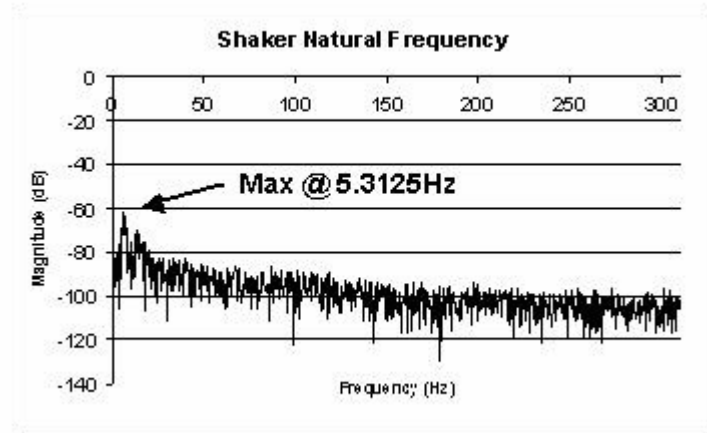


Figure 3.12 FRF of Shaker with a Mounted Beam

The laser vibrometer was used to collect a transfer function at a point on the end of shaker arm. The mobility FRF shown in Figure 3.12 shows a peak at approximately 5 Hz for one of the short beams. This very low mode is most likely due to the rubber bands in the shaker. This mode appeared in all of the short beams and long beams that were mounted on the shaker. This mode can be disregarded as not being one of the bending modes of the beams.

The second driver that will be used are specially manufactured PZTs. The PZTs were manufactured by NASA so that they are flexible and will be able to be put on the curved surface of the struts. The PZTs are adequate to meet the test frequency range from 0 to 1000 Hz. The PZTs will be placed near the base of the beams in order to provide excitation. They will be placed on opposite sides and actuated so that they provide bending in the same direction at the same time. They are mounted approximately one inch from the top of flange to insure that they are above the portion that that beam is adhered to on the inside. An excitation signal of several hundred volts can be used to actuate the PZTs. An amplifier was used; however, voltage was limited to approximately 40 Volts due to the fact

that a random signal generator was used. A voltage of approximately 140 was obtained using a sinusoidal wave generator; however, too much noise was created in the transfer function. Pictures of the PZT mounted on the short beam are shown later.

3.3.3 PZT adhesives. Due to the fact that beams will be used in a vacuum and must withstand very high and low temperatures, a special adhesive had to be found. Micro-Measurements M-Bond 300 is a special-purpose, two-component polyester adhesive used for strain gage bonding. It cures at approximately $20^{\circ}C$ and is operational up to $+150^{\circ}C$. This makes it ideal for use with the PZTs in the vacuum chamber where the temperature will be approximately $+100^{\circ}C$. However, while possessing a high shear strength, which is the primary requirement for a good strain gage adhesive, the M-Bond 300 has a relatively low peel strength compared to other M-Bond adhesives. Although the PZTs are flexible, bonding them to the beams proved challenging. Due to the high operating temperature rating and only 1-2% elongation after it cured, it seemed ideal for use and was used on beam S03. Beam S03 was selected because the lower third of the beam (near the base) had a smooth surface and few irregularities when compared to the other short beam. Figure 3.13 shows the base end of Beam S03. The first attempt was made using M-Bond 300, Batch 6679, Control Number 066. It failed to properly bond near the lead wire tabs and the PZT began lifting off due to the tension in the PZT. The PZT was easily peeled off.[14]

The second adhesive that was selected was M-Bond GA-2, a 100%-solids epoxy system for use with strain gages and special-purpose sensors. It is rated to an operational temperature of $+95^{\circ}C$. The GA-2 with Hardener 10-A has approximately 10% to 15% elongation capabilities when cured for 40 hours at $+20^{\circ}C$. M-Bond GA-2, Batch 6685, Control Number 0295E was used. The beam was allowed to cure for more than 48 hours.[15] Mounting the PZT was very difficult because the mixed adhesive was very viscous. The PZT was applied with the adhesive, then wrapped

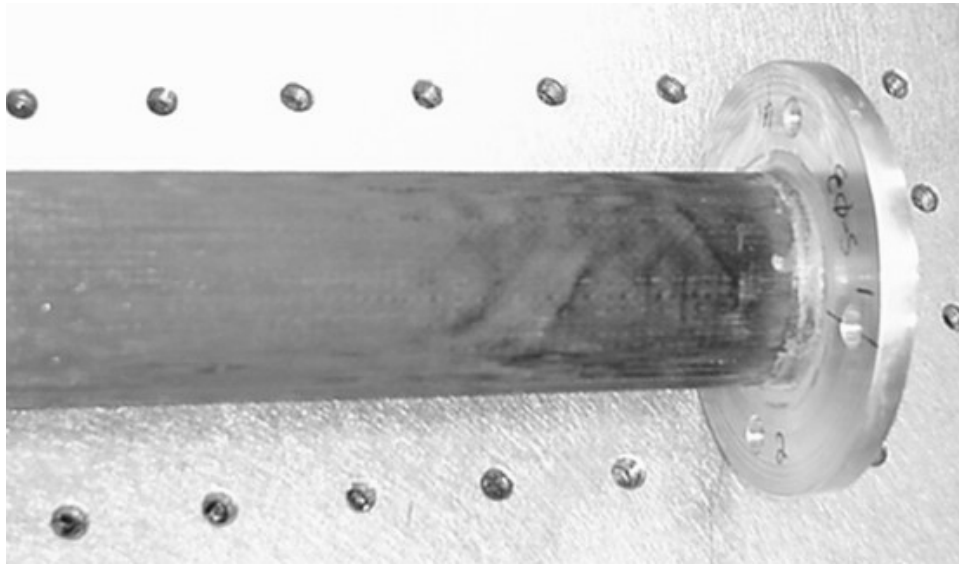


Figure 3.13 Closeup of base end of beam S03

with mylar tape to secure it to the beam. Figure 3.14 shows beam S03 with the PZT mounted near the base of the beam. The PZT is approximately one third the length of the beam. The PZTs were able to be mounted so that they have contact over their entire surface with the beam. There was some seepage onto the beam that can be seen in Figure 3.15. The PZT was mounted approximately one inch up from the base flange to ensure that it was above the part of the flange that the beam was attached to. The PZTs were mounted opposite of each other so that they could be actuated together to provide bending in the same direction. The cured adhesive is stiff and rigid, and is almost the one third the length of the beam. This change slightly changed the bending properties of the beam, which was reflected in a shift in the natural frequencies and a change in the damping ratios. The beam was tested to ensure that the PZTs worked correctly with good results.

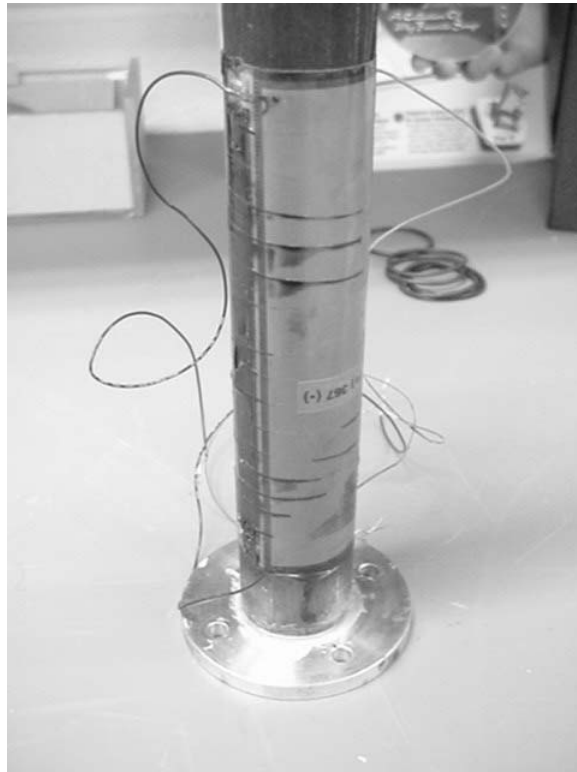


Figure 3.14 Beam S03 with PZT installed.

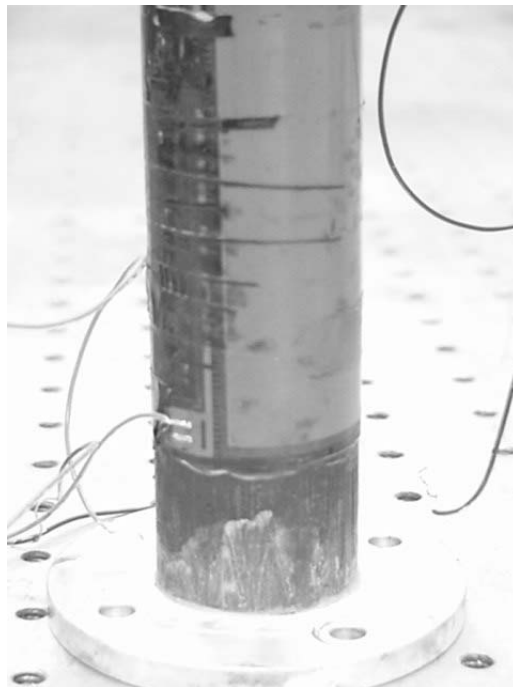


Figure 3.15 Closeup of the PZT on S03

3.3.4 Sensor Description. The response of the beams to excitation was measured three different ways. The first was an accelerometer mounted vertically on the end of the shaker arm, in-line with the centerline of the beam. The accelerometer utilized was an ENDEVCO® model 2250A-10. The accelerometer had a nominal sensitivity of 10 mV/g, a range of $\pm 500g$, and a frequency range of 1-8000 Hz.[17] The accelerometer was mounted to detect the acceleration along the Z-axis as shown in Figure 3.16. The accelerometer was placed as close to the centerline of the beam as possible, this was limited by the nut on the bolt used to mount the beam.

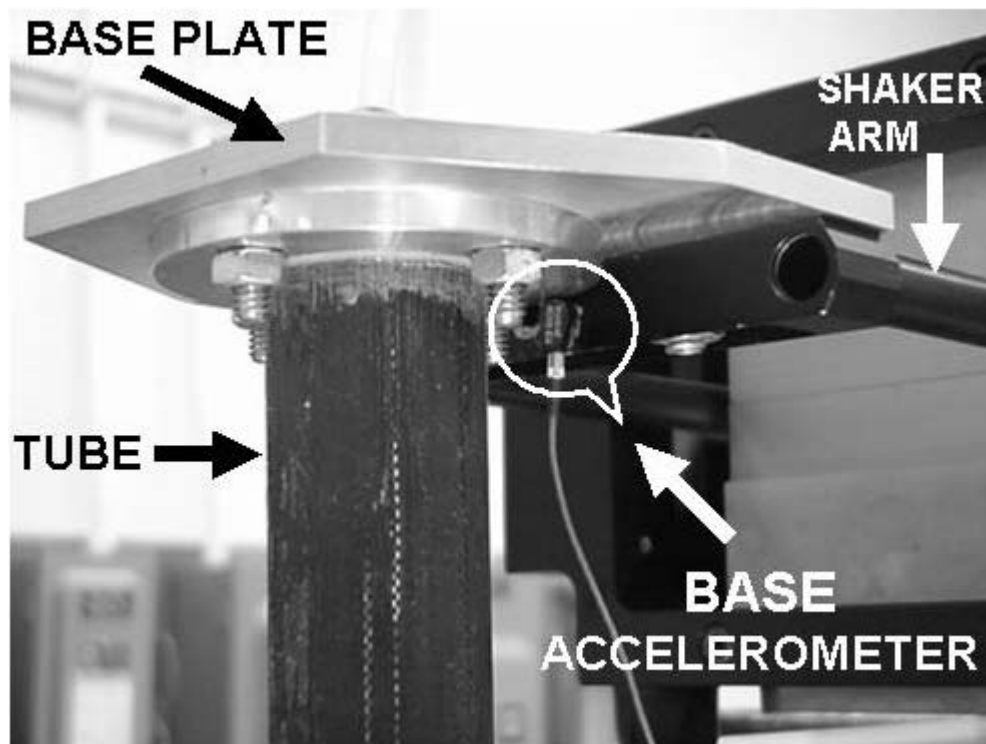


Figure 3.16 ENDEVCO 2250A – 10 Accelerometer shown mounted on the shaker arm.

The second accelerometer (placed in the tip flange of the beam), was the ENDEVCO® Model 63B-100: a lightweight triaxial piezoelectric accelerometer with integral electronics, designed specifically to measure modal responses in three orthogonal axes. The accelerometer incorporates three independent internal signal conditioners operating in constant current mode. The signal ground is isolated from

the mounting surface. The 63B-100 has a voltage sensitivity of 100 mV/g. The 63B is has an effective operating range of -55°C to $+125^{\circ}\text{C}$. The 63B is a .562 inch cube.

Figure 3.17 shows the Model 63B-100 tri-axial accelerometer. Note that there is a clip that can be used for mounting. The clip was only used for the PZT tests. The accelerometers were attached to the structure with a thin layer of modal wax. This attachment method is valid for frequencies between 0 and 2000 Hz.[2] This experiment is well within the usable range.

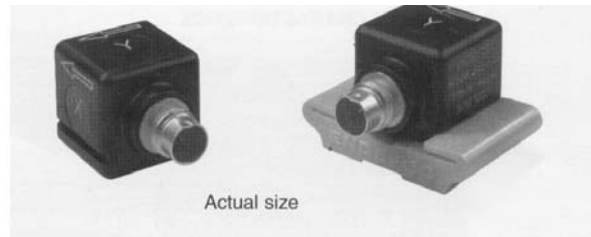


Figure 3.17 ENDEVCO 63B-100 Accelerometer. The Σ Z-mount clip is on the right. Note that the accelerometer is NOT the actual size.

The frequency response of the unit is limited to 1 kHz when the Σ Z-mount is used. Figure 3.18 shows the typical response curves for the 63B. [16] The Modal 63B

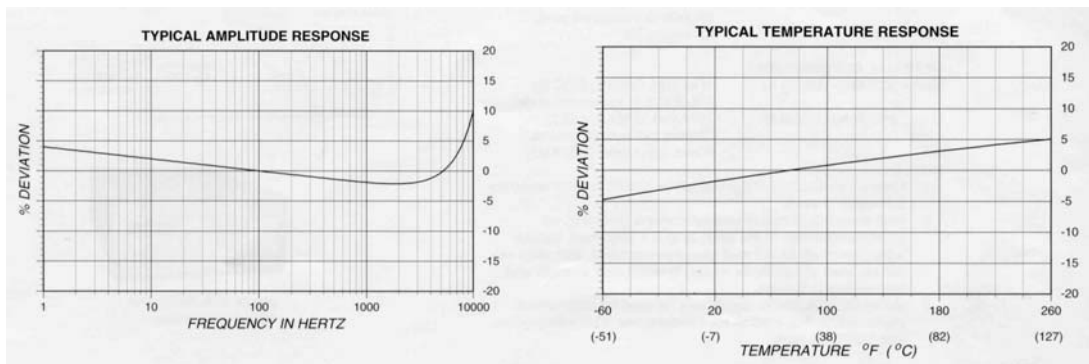


Figure 3.18 Typical Amplitude and Temperature Response

is designed to withstand typical handling in the laboratory environment; however, it should be further studied to ensure that it will meet the rigors of launch into space.

It is important to note the direction of the excitation and the orientation of the accelerometer. Figure 3.19 shows the axis alignment for the experiment.

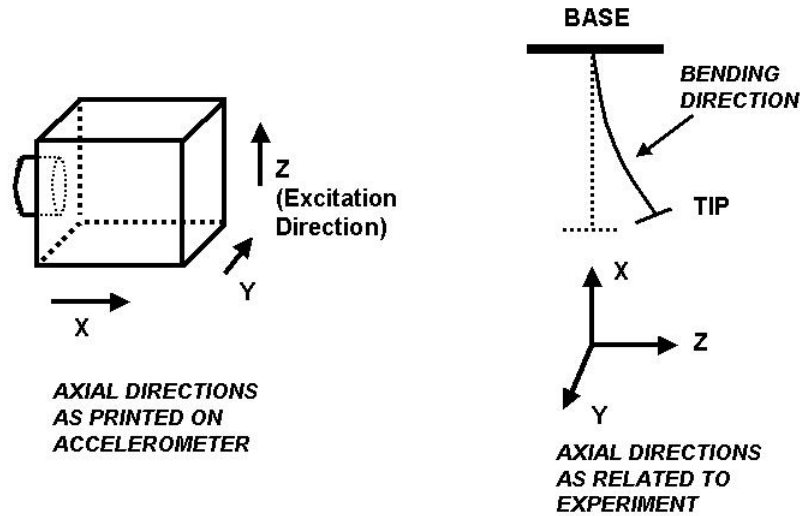


Figure 3.19 Accelerometer Axis Alignment

The third method of measuring the response was the Polytec Scanning Vibrometer (PSV) 300 used for the ambient tests. The PSV measures and analyzes vibrations. The PSV program records a time signal of the vibration (velocity) for each scan point. The time signal is sampled with a certain frequency for a certain time. The recorded signal consists of a discrete number of sampling values. The program uses the FFT procedure (Fast Fourier Transformation) in order to generate the corresponding frequency spectrum. Figure 3.20 shows the PSV 300.

To record a test, in the acquisition mode, several steps were taken. The first was to physically align the vibrometer to be as close to the vertical height of the scan point as possible. The vibrometer was also moved as far away as possible in order to keep the angle of the laser as small as possible. Large angles deflect the laser and poor readings result. The vibrometer was placed approximately 20 feet from the test stand. Once the strut was mounted onto the test stand, a coordinate



Figure 3.20 PSV 300 Laser Vibrometer

system was created using the PSV software. This allowed the scan points to be properly aligned for each test article. The number of scan points in the mesh and the type of mesh were then specified. Two different meshes were used, rectangular and triangular. Figure 3.21 shows a sample of a rectangular mesh. The vibrometer builds a three-dimensional model of the test piece; therefore, three scan points were used across the beam to give the model some depth. The number of points down the beam varied, with 15 being the minimum and 50 being the maximum number of points in the vertical direction. Typically, 50 to 80 scan points were used, which took from 1.5 hours to 4 hours for the vibrometer to complete a scan. Figure 3.22 demonstrates a triangular mesh that was used on a few tests. Changing the type of mesh did not result in any different results of identifying the modal properties. Once the scan is complete, the presentation mode can be used in PSV to view the results as shown in Figure 3.23. The program allows the model to be rotated about the

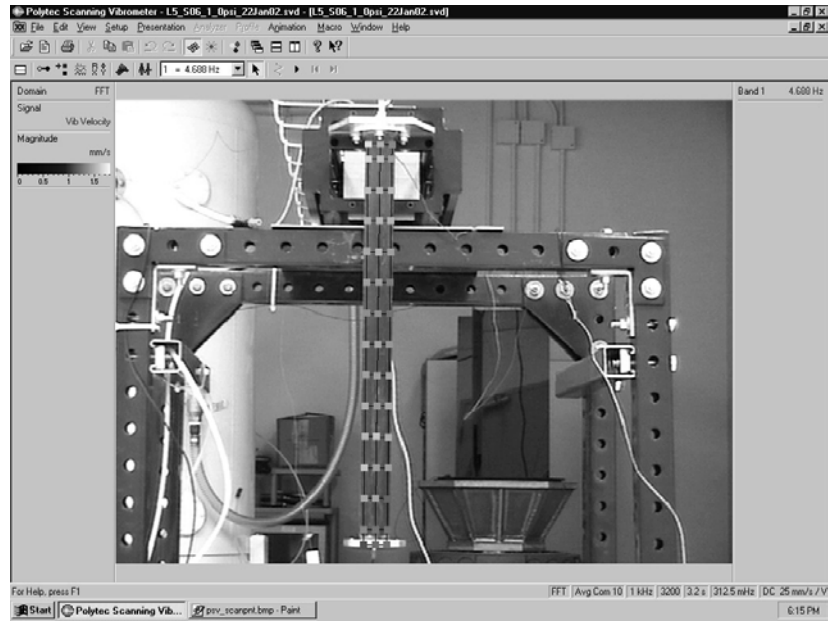


Figure 3.21 PSV Rectangular Mesh Scan Points

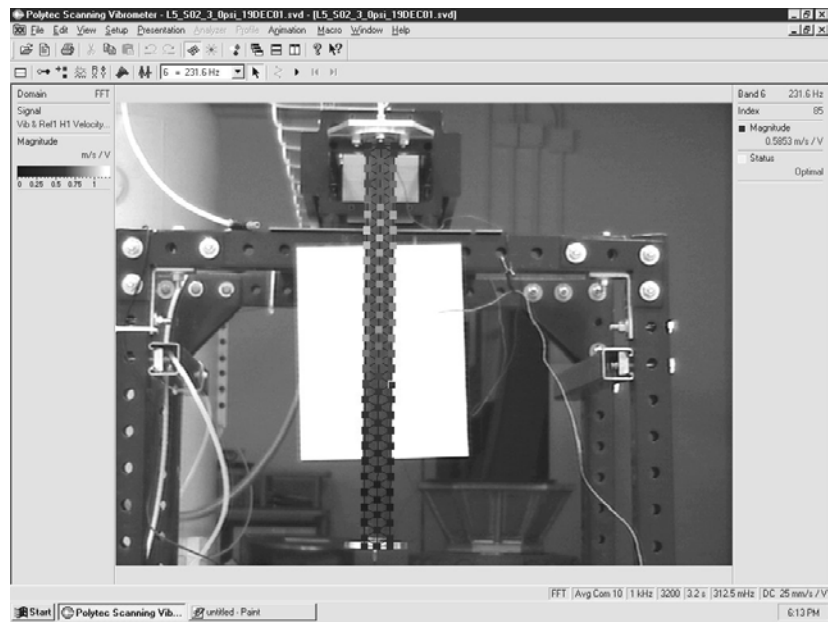


Figure 3.22 PSV Triangle Mesh Scan Points

three axis, to view the FRF, and to calculate the frequency bands/peaks. This data was then exported to be used as a comparison to the accelerometer data. During the

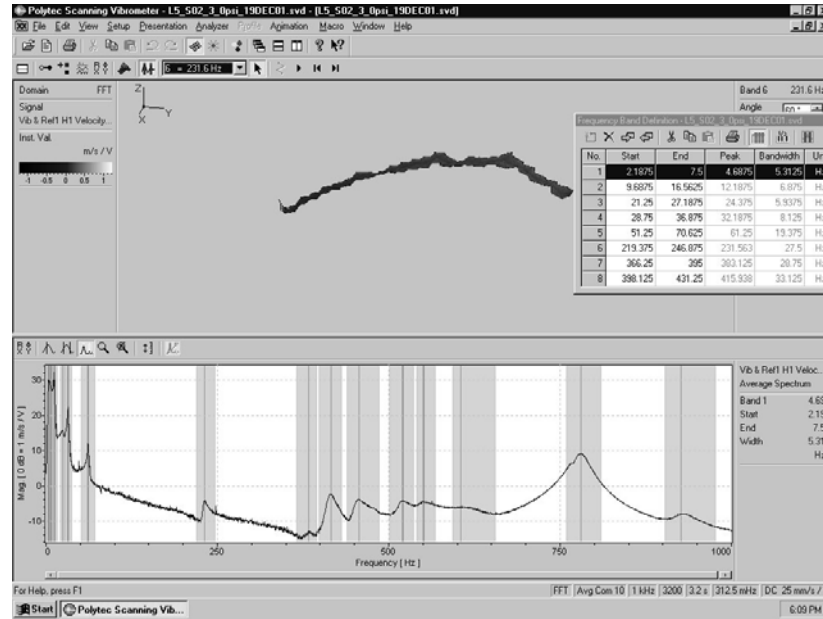


Figure 3.23 PSV GUI

testing using the accelerometers on the shaker, a single scan point was placed along the centerline on the edge of the tip flange of the beam. This is the “vibrometer” data point that was recorded in SignalCalc on Channel 5. Note that for contrast to better be able to align the coordinates on the black colored beams, white notebook paper was taped behind the beams.

3.3.5 Accelerometer Calibration. A comparison calibration (standard versus test) was utilized to determine the sensitivities of the accelerometers used in this experiment. The equipment setup can be seen in Figure 3.24. The shaker used was a MB Dynamics Model Cal 50, fifty pound shaker (as seen on the left). Excitation signals from the HP system were amplified by an MB Dynamics Model SS530 amplifier (as seen on the right) before being sent to the shaker. The standard accelerometer and its power supply (the small box between the shaker and amplifier) are the components of a PCB Piezotronics Model 394A10 vibration calibration

system, which has an average sensitivity of 99.79mV/g for 10 to 1000 Hz. The test accelerometer was mounted on the standard accelerometer with modal wax.

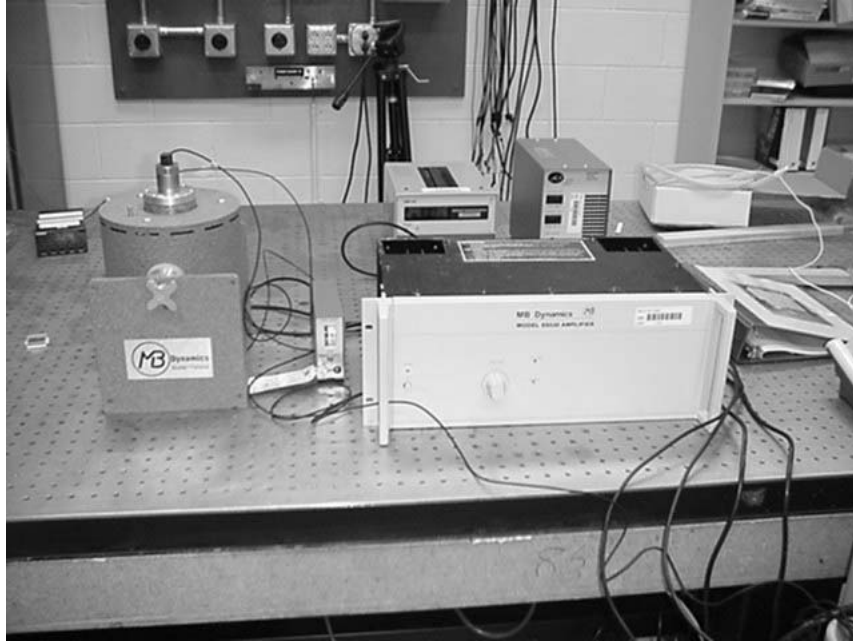


Figure 3.24 Accelerometer Calibration Setup

SignalCalc was used to provide a random signal with bandwidth of 1 kHz was utilized as an input to the shaker. The digitized knob on the amplifier was set to one click before its middle setting. The channel range for the standard accelerometer was set at $\pm 1V$ and the channel range for the ENDEVCO[®] accelerometer was set at $\pm 0.1V$. Data was sampled at a rate of 3200 Hz. 32 averages were used for each data set with a 50% overlap. The FRF and coherence between the two accelerometers were compared. The RMS value of the sensitivities used throughout the experiments are shown in Table 3.4. Each axis of the tri-axial accelerometers were tested. Tri-axial accelerometer 10964 was the one that was used for the experiment, 10966 was a spare accelerometer. The PSV sensitivity used is also shown.

Table 3.4 Accelerometer Sensitivities

Description	Channel	Sensitivity mV/EU	Unit (EU)
10966 X axis	not used	101.8	g
10966 Y axis	not used	98.77	g
10966 Z axis	not used	100.1	g
10964 X axis	2	98.51	g
10964 Y axis	3	99.50	g
10964 Z axis	4	98.92	g
18906	7	10.09	V
Vibrometer	5	40K	m/s

3.3.6 Vacuum Chamber Setup. A chamber was manufactured to produce a near-vacuum pressure. A vacuum pump was connected to the chamber and allowed to pump continuously during the testing. The chamber, shown with the heater canister and a short beam, can be seen in Figure 3.25. The chamber was larger enough to mount the beam and heater canister inside, along with the test equipment. The chamber achieved a “vacuum” of 0.15 psi after approximately ten minutes. This is not a vacuum; however, it did provide a significant change in the pressure around the beam from 14.3 psi to .15 psi.

The vacuum chamber was designed to have access through holes in the bulk-head where different plates can be attached. A grounded plate was made with four BNC connectors to be used with the accelerometers. The X, Y, and Z axis signals from the accelerometer used a separate channel. The fourth connector was a spare. To drive the PZTs and to provide power to the heaters, two plates were made with two sets of positive and negative connectors through the plate. These two “power” plates were mounted as far away as possible from the BNC connector plates to reduce the noise created by the field created by the current running through the wires. A plate was also made to allow thermocouple and barometer wires into the chamber. Two different valves control access to chamber: one to the hose that leads to the vacuum pump, and one to allow ambient air into the chamber. Another plate was used to provide access to a beam for pressurizing the beam. O-rings and vacuum grease were used to seal all of the plates against the bulkhead. A torque wrench



Figure 3.25 Vacuum Chamber with heating canister and Beam S03

was used to ensure proper seal of the plates. Attempts were made to ensure that all wires, equipment, adhesives, etc., were manufactured to withstand at least $+100^{\circ}\text{C}$ and to not outgas in a vacuum.

Inside the chamber, a test stand was bolted. A cross member allowed a bracket to be mounted across the chamber. A base plate with a short beam attached could then be mounted inside. Wires for the accelerometer, PZTs, thermocouple, and the heaters were run on from the bulkhead to the equipment. The heater canister (described in the following section) was attached to the bracket. No wires were

allowed to touch the beam or the heater canister. A picture of the inside of the vacuum chamber is shown in Figure 3.26.

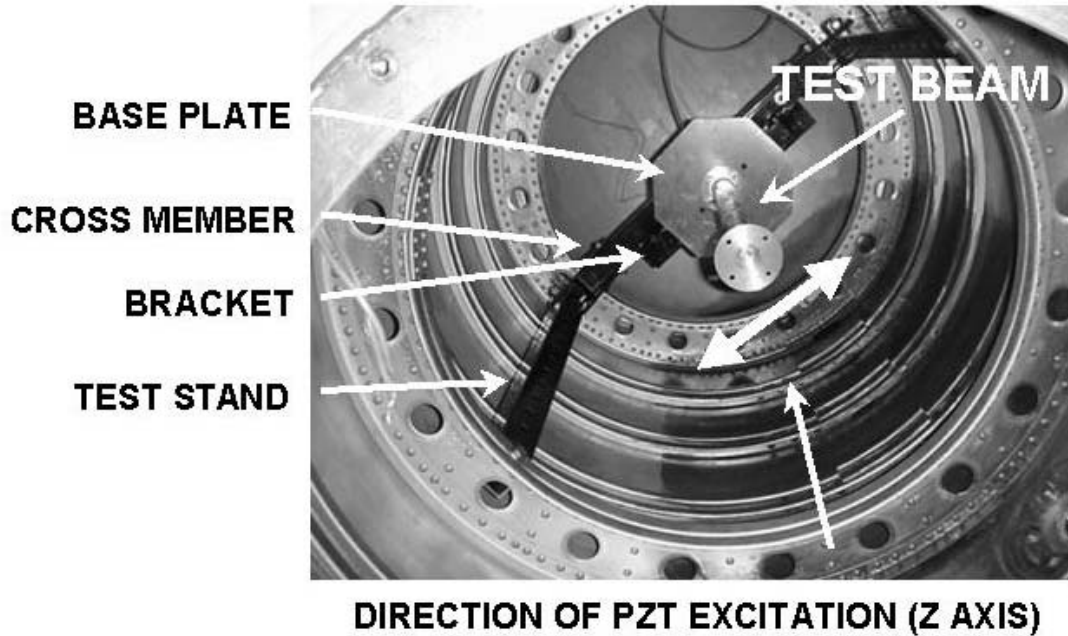


Figure 3.26 Vacuum Chamber Setup (Internal View)

3.3.7 Heaters. The heaters required for the RIGEX experiment must fit inside the small spaces and be light weight. The beams will be heated to approximately $+100^{\circ}\text{C}$ in order to simulate heating them in the ovens to be soft enough to be inflated. When in a vacuum, the beams will only be softened using radiated heat. On the RIGEX flight test experiment, the heaters will be used in the small confined area of the ovens to heat the beams. For the vacuum chamber, the beams will not be folded, and they are not confined. The solution was to use Minco ThermofoilTM heaters placed on the inside of a canister, hereafter called the “heater canister”.

The ThermofoilTM heaters are thin, flexible heating elements consisting of an etched-foil resistive element laminated between layers of flexible insulation.[34] Their thin profile gives close thermal coupling between the heater and the heat sink. The flat foil element of the heaters transfers heat more efficiently, over a larger surface

areas than round wire. The ThermofoilTM heaters stay cooler than wire, which results in a higher allowable watt density, and a faster warmup. Kapton insulated heaters were selected, because they have already been flight qualified under NASA specification S-311-P-079.[34] An example of a kapton insulated MINCO heater is shown in Figure 3.27. The heaters typically weigh only 0.25 grams per square inch

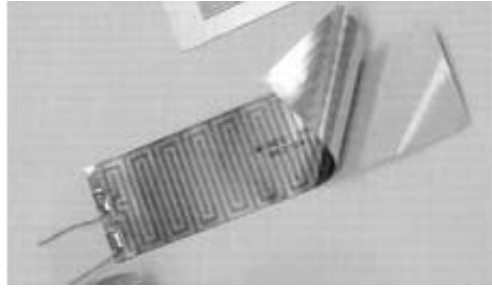


Figure 3.27 Example of a Minco ThermofoilTM heater

and measure just 0.010" thick over the element.[34] This weight and space savings is critical for the constraints placed on the experiment. The Kapton insulated heaters when used with aluminum backing, have low outgassing and have an effective operating range of $-200^{\circ}C$ to $+150^{\circ}C$. [34] The heaters (product number HK15718) that were custom ordered, are 12 inches wide and 20 inches long. Four of them were used to line the inside of the canister. They were placed length wise (20" side is vertical), requiring two of them on each half of the inside. This provides a total surface heating area of 1408 square inches surrounding the beam. Approximately 7 inches at the top of canister and 3 inches on the bottom are not covered by the heaters to provide room for the bracket and other hardware.

During testing, the test beam was bolted to a crossbar inside the vacuum chamber so that the beam was in the center of the heating canister. The heating canister provided an even source of heat through radiation. The canister was made of 0.08 inch thick aluminum that is approximately 14 inches in diameter and 35 inches tall as shown in Figure 3.28.



Figure 3.28 Heating Canister

The heaters were installed using a pressure-sensitive adhesive (PSA) film. Minco #10 PSA aluminum backing adhesive was used. It has an operating temperature range of -54°C to 150°C . It also has low outgassing and is easy to apply by peeling off the back film and pressing it down.[33, 34] Although difficult to tell in a black and white figure, Figure 3.29 shows the heating canister with the ThermofoilTM heaters installed to the inside of the canister.

To power the heaters, a very simple system was used. A thermocouple was placed approximately 0.25 inches from the surface of the beam in the center of the canister to monitor the temperature. A power source was used with a dial that controlled how many amps were used. The four heaters were connected in series, with each having a resistance of 7.6 Ohms (Ω). Figure 3.30 shows a simple layout of the system supplying power to the heaters.



Figure 3.29 Heating canister with MINCO Thermofoil™ heaters installed

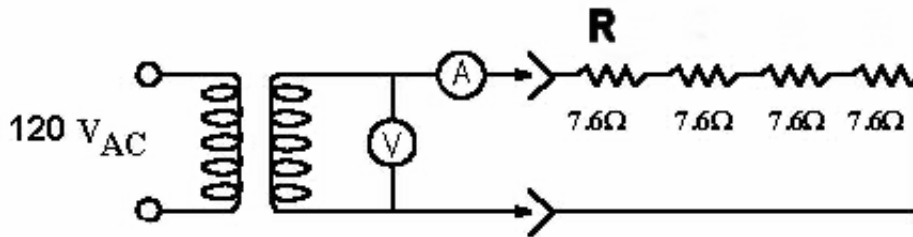


Figure 3.30 Wire Diagram of Heater Power System

Using the following equations, the current and power can be computed:

$$Current = V/R = 3.95 \text{ Amps} \quad (3.1)$$

$$Power = V^2/R = .431 \text{ Watts} \quad (3.2)$$

where the voltage (V) is 110 volts, and the total resistance (R) is

$$R = 7.6 \times 4 = 30.4\Omega \quad (3.3)$$

At approximately 0.5 psi in the vacuum chamber, using 3.75 amps, the heaters were able to achieve a temperature of $+100^{\circ}C$ in approximately 20 minutes. The power was then backed down to 3 amps where it maintained a stable $+100^{\circ}C$ for an hour. $+95^{\circ}C$ was obtained by heating the chamber to $+100^{\circ}C$ and then drawing 2.1 amps to maintain $+95^{\circ}C$.

3.4 Analytic Beam Model

An analytic beam model must be developed for use with the PZTs. The development of the following model was provided by the Thesis Advisor[1]. The model is for a beam with a PZT mounted on it, where the width of the PZT is less than half the circumference of the beam.

3.4.1 Kinematics of Deformation. The beams are assumed to deform such that they undergo deformation consistent with beams. Consequently, the following can be written:

$$u(x, t) = u_0(x, t) - R w_0(x, t) \quad (3.4)$$

$$w(x, t) = w_0(x, t) \quad (3.5)$$

where R is the radius of the beam. The strain in the beam due to deformation will only be axial, defined as:

$$\epsilon_x = u_{0,x} + R w_{0,xx} \quad (3.6)$$

The axial and transverse deformations will be un-coupled; therefore, the axial component will be neglected.

3.4.2 Energy. Using energy methods, the equations of motion for the beam being excited by the PZT will be derived. The strain energy of the beam will

be

$$U = \frac{1}{2} \int_0^L \int_0^{2\pi} \sum_{i=1}^k H^i [E_{xx}(\epsilon_x^2 - \epsilon_x v_x^{(i)})] R d\theta dx \quad (3.7)$$

The piezoelectric forcing function can be defined as follows:

$$v_x^{(i)} = \begin{cases} 0 & -\theta_1^{(i)} < \theta < \theta_1^{(i)}, \\ v_x^{(i)} & \theta_1^{(i)} < \theta < \pi - \theta_1^{(i)}, \\ 0 & \pi - \theta_1^{(i)} < \theta < \pi + \theta_1^{(i)}, \\ -v_x^{(i)} & \pi + \theta_1^{(i)} < \theta < 2\pi - \theta_1^{(i)}. \end{cases}$$

Integration with respect to θ can now be performed on equation 3.7.

$$U = \frac{1}{2} \int_0^L H^i [E_{xx}^{(i)} R^3 \pi [(w_0'')^2 + 4R^2 \pi w_0'' \cos(\theta_1^{(i)}) v_1^{(i)}]] \quad (3.8)$$

The kinetic energy is given by:

$$T = \frac{1}{2} \int_0^L \sum_{i=1}^k H^i \rho^{(i)} w_0^{tt} 2\pi R d\theta dx + J(w_0(L)^{tx})^2 + M(w_0(L)^t)^2 \quad (3.9)$$

where J is the inertia at the tip due to the tip mass, M. The axial deformation has been neglected. The potential energy due to the axial loading is given by:

$$V = \frac{1}{2} \int_0^L (w_0')^2 dx \quad (3.10)$$

Finally, the work due to an external force can be expressed by:

$$W = F(t)w(t) \quad (3.11)$$

3.4.3 Equations of Motion. Using Hamilton's Principle, the equations of motion can now be found:

$$\int (\delta U + \delta V + \delta W - \delta T) dt = 0 \quad (3.12)$$

The equation of motion results in:

$$EIw_0'''' + mw_0'' = 0 \quad (3.13)$$

where the “ ’ ” denotes the order of the derivative, with the boundary conditions:

at $x = 0$

$$w_0 = 0$$

$$w_0' = 0$$

and at $x = L$

$$EIw_0''' + F - Mw_0^{tt} = 0 \quad (3.14)$$

$$EIw_0'' + Jw_0^{xxtt} = 0 \quad (3.15)$$

where

$$EI = \sum_{i=1}^k E_{xx}^{(i)} H^{(i)} R^3 \pi \quad (3.16)$$

$$m = \sum_{i=1}^k 2\pi R H^{(i)} \rho^{(i)} \quad (3.17)$$

These equations were solved using a Rayleigh-Ritz approximation.

3.4.4 Analytical Results. For the cantilever beam with a tip mass and tip inertia, a series of quasi-comparison functions was chosen as the Ritz basis. The mode shapes are similar to those for both clamped-pinned (even series terms) and clamped-slider (odd terms). The chosen series is:

$$w_0 = \sum_{i=1}^n q_i(t) (\cosh(\beta_i x) - \cos(\beta_i x) - \sinh(\beta_i x) + \sin(\beta_i x)) \quad (3.18)$$

$$= \sum_{i=1}^n q_i(t) \phi_i(x) \quad (3.19)$$

where

$$\beta_i x = \frac{2i+1}{4}\pi \quad (3.20)$$

Substituting Equations 3.18 - 3.20 into Equations 3.8 - 3.10, and taking the variation of the resulting energy functional, the equations of motion can be found. The mass and stiffness matrices are defined as:

$$[M_{ij}] = \int_0^L m\phi_i(x)\phi_j(x)dx + M\phi_i(L)\phi_j(L) + J\frac{d\phi_i(L)}{dx}\frac{d\phi_j(L)}{dx} \quad (3.21)$$

$$[K_{ij}] = \int_0^L EI\frac{d^2\phi_i(x)}{dx^2}\frac{d^2\phi_j(x)}{dx^2} \quad (3.22)$$

$$F = \phi_j(L) \quad (3.23)$$

The resulting equation of motion is:

$$[M]\ddot{q} + [K]q = F \quad (3.24)$$

3.4.5 Convergence. This Rayleigh-Ritz approximation using quasi-comparison functions can now be solved to yield the eigenvalues and natural frequencies. These will be compared to the experimental results in the next chapter to determine if the Euler-Bernoulli beam assumptions are valid. The Ritz approximation provides the following relationship for the eigenvalues (λ):

$$\lambda = \text{eigenvals}([M^{-1}][K]) \quad (3.25)$$

The values of omega in hertz are calculated as follows:

$$\omega_n = \frac{\sqrt{\lambda}}{2\pi} \quad (3.26)$$

Table 3.5 Ritz Approximation Convergence for Beam S03

n	Mode 1	Mode 2	Mode 3
1	2.167	N/A	N/A
2	1.422	60.963	N/A
3	1.061	60.96	220.823
4	1.001	60.958	199.18
5	0.997	60.957	197.75
6	0.996	60.957	197.296
7	0.996	60.946	197.356
8	0.996	61.391	197.342
9	0.996	61.073	197.33
10	0.996	61.071	197.256
11	0.996	61.011	197.11
12	0.996	60.981	196.91

To determine the convergence of the quasi-comparison functions used, the natural frequencies of the first three modes were investigated. Table 3.5 shows that the first 12 terms of the Ritz convergence using Mathsoft Mathcad® 2001. The solution was limited to 12 terms because of a numerical limit reached during the convergence iterations of the stiffness matrix. The value for Young's Modulus (E) was estimated based on tests from L'Garde.[1] The first mode at one hertz is below an acceptable level of reliability for the test equipment. The first mode at 1 Hz was not determined by the vibration testing. The modes at 60 and 196 Hz have not fully converged with 12 iterations; however, they provide an approximation that is accurate enough to compare to the test data. The first four modes shapes were calculated and are shown in Figures 3.31 - 3.34. The Ritz approximated the fourth mode around 417.3 Hz.

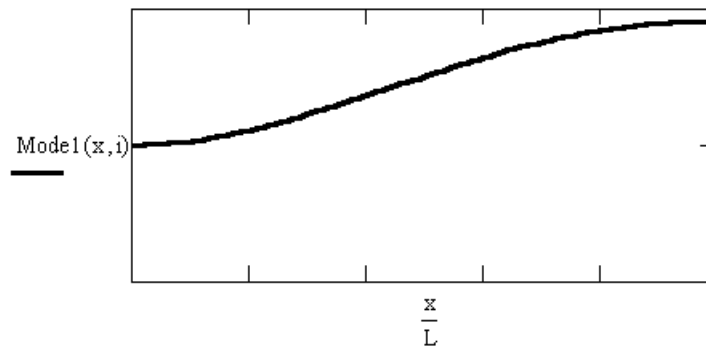


Figure 3.31 1st Bending Mode at 1 Hz

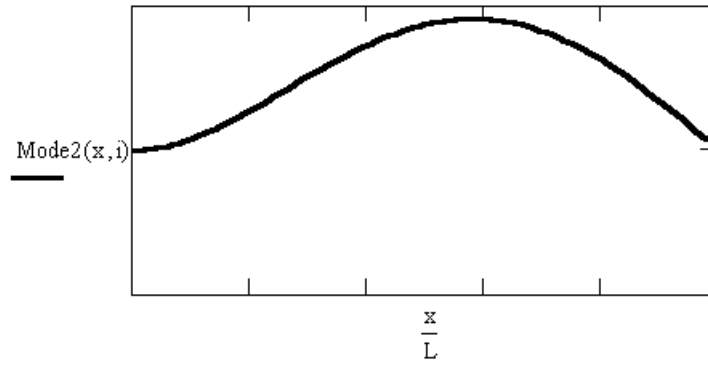


Figure 3.32 2nd Bending Mode at 60.9 Hz

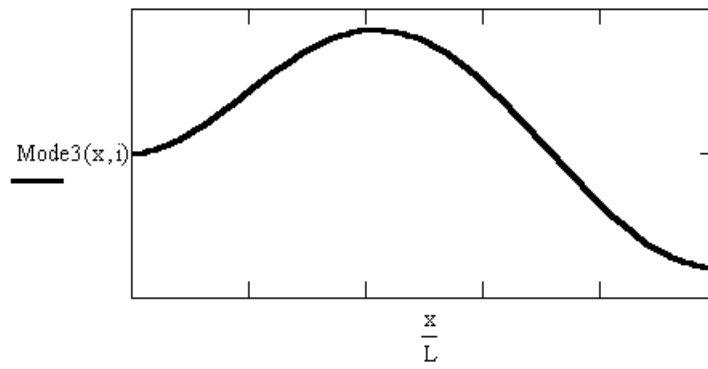


Figure 3.33 3rd Bending Mode at 196.9 Hz

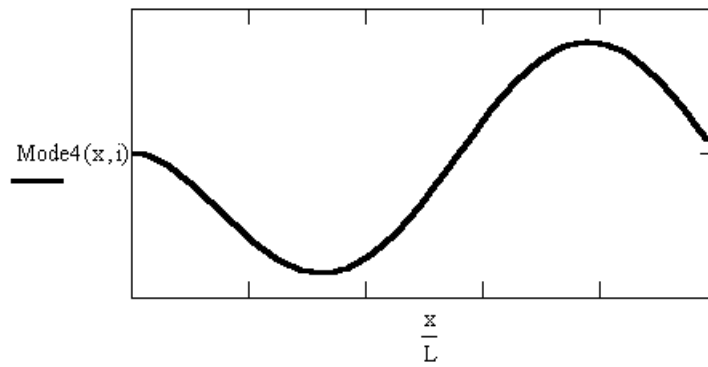


Figure 3.34 4th Bending Mode at 417.3 Hz

3.5 Experimental Vibrations Testing Overview

A test stand was built and bolted to the isolated, damped table in the AFIT Vibrations Laboratory. The shaker was then mounted on top of the test stand. This provides a stable, rigid structure in order to be able to collect the modal data from the test specimens. For all of the testing, the beams were bolted to a base plate using approximately 50 in/lb of torque. The shaker tests utilized a small base plate, while the vacuum chamber required a larger base plate (for mounted requirements). An o-ring was used between the base of the beam and the base plate to ensure an air-tight seal. Figure 3.35 shows the setup of the short beams mounted to the base plate, mounted on the shaker arm that is on top of the test stand bolted to the damped vibrations table. An air line is used to supply positive pressure inside the beam.

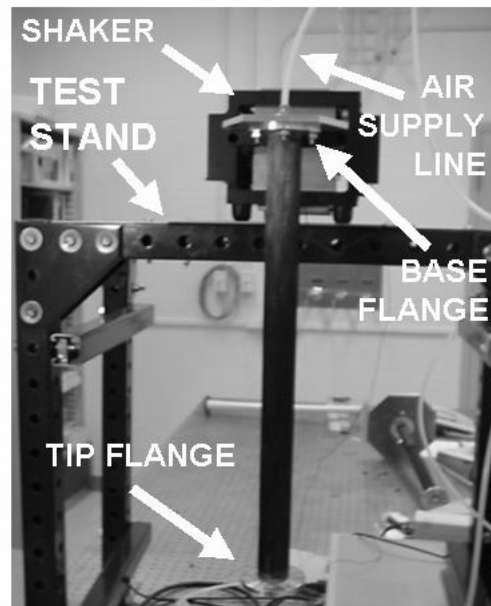


Figure 3.35 Short beam mounted on shaker

Figure 3.36 shows beam S03 with the PZTs, mounted on the larger base plate used in the vacuum chamber, which is subsequently mounted onto the bracket that is used in the vacuum chamber, which is then mounted to the test stand on the table. The PZT can be seen as the light colored rectangular section on the beam near the base base plate. The long beam mounted on the shaker is shown in Figure 3.37.

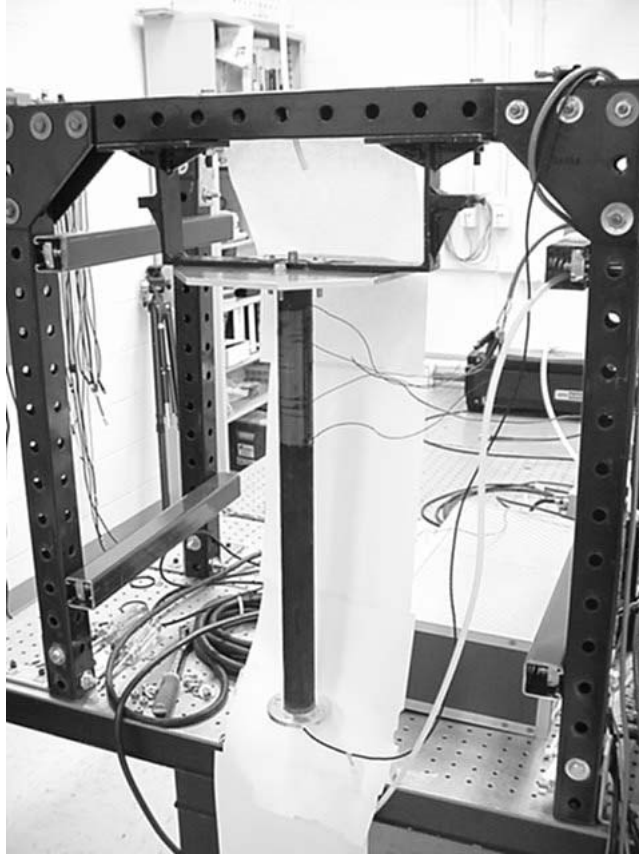


Figure 3.36 Beam S03 with PZT installed.

3.5.1 Ambient Condition Tests. The first set of tests were accomplished in ambient atmospheric conditions utilizing the shaker on the vibrations table. The shaker provided clean data, with the exception of the modes that it imparted to the system. Tests were run on the shaker with a beam mounted in order to determine the modes that the shaker created. The test apparatus has already been described in detail above. All of the available beams (that didn't leak air) were

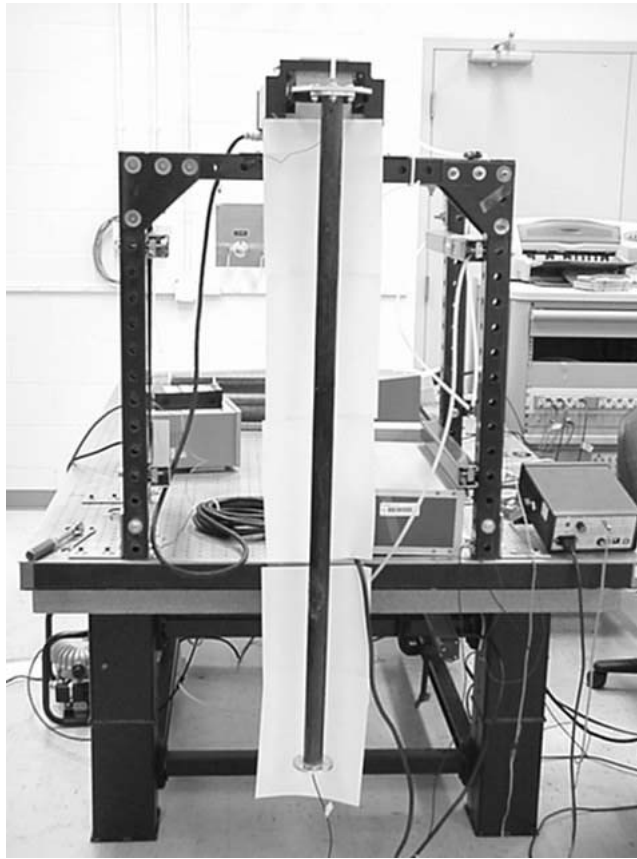


Figure 3.37 Long Beam on the shaker

tested on the shaker in ambient conditions. This included the five short beams, two long beams, and a retest of one of the short beams with the PZTs mounted on it. Three different excitation levels were used to drive the shaker to determine which provided the best results. It was expected that the different excitation levels would not effect the FRF; however, this was checked.

The beams have a seam where the beam material was joined. Two of the beams will be rotated at the four different mounting points to determine if the seam has an effect on the modal properties. Since the beams will be experiencing positive pressure during inflation, several different pressures were tested. Increasing the internal pressure should make the beams stiffer, and shift the natural frequencies and damping ratios. Gage pressures of +0, 2, 4, and 6 psi were chosen. This provided

enough data points to determine a trend if there is one. The laser vibrometer takes a significant amount of time to conduct an entire scan; therefore, scans were only be accomplished at zero and four psi.

The next set of tests were on a short beam (S03) that was chosen to have the PZTs mounted to it. The beam was tested on the shaker, with the excitation being produced by the shaker. The PZTs were then used for the excitation. Finally, the bracket and base plate to be used in the vacuum chamber was mounted on the test stand and the PZTs were used for excitation. After conducting the shaker tests, a excitation level of 300mV was chosen because it produced the best results with the least amount of feedback and noise. If the beams are excited too hard/soft, or at to high/low of a frequency range, the noise levels can become too high to accurately collect data. Table 3.6 shows the shaker test matrix. A bold “**X**” denotes a laser vibrometer scan was also accomplished.

The PZT tests consisted of using the S03 beam with the PZT mounted on it. The beam was tested using both the shaker and the PZT for excitation. Pressures of 0,2,4, and 6 psi were used on the table. Pressures of 0 and 4 psi were used in the vacuum chamber. It is important to note that the excitation direction of the PZT when the beam was mounted on the bracket was perpendicular to the the bracket (it will be parallel in the vacuum tests). This was due to the limitations of the laboratory because the room was narrow and the laser vibrometer would not be able to be used to capture the velocity changes in the z axis direction. This made the FRF of the test stand and the vacuum chamber different due to the different boundary conditions. The FRFs will be shown in chapter 4.

3.5.2 Vacuum Chamber Tests. The next set of tests are in the vacuum chamber. The tests using the PZTs are critical in establishing the baseline modal data for the future flight test experiments. For the vacuum tests, the tri-axial accelerometer used the quick mount clip. The base plate was mounted to the bracket

Table 3.6 Shaker Test Matrix

Pressure Level:	0 psi			2 psi		
Excitation Level:	125mV	300mV	500mV	125mV	300mV	500mV
Beam Orientation (1-4)						
S02-1	x	X	x	x	x	x
S02-2	x	X	x	x	x	x
S02-3	x	X	x	x	x	x
S02-4	x	X	x	x	x	x
S03-1	x	X	x	x	x	x
S03-2	x	x	x	x	x	x
S03-3	x	x	x	x	x	x
S03-4	x	x	x	x	x	x
S04-1		X			x	
S05-1		X			x	
S06-1		X			x	
Excitation Level:	200mV			200mV		
L01-1		X			x	
L03-1		X			x	
S03 w/ PZT		X			x	
Pressure Level	4 psi			6 psi		
Excitation Level	125mV	300mV	500mV	125mV	300mV	500mV
Beam Orientation (1-4)						
S02-1	x	X	x	x	x	x
S02-2	x	X	x	x	x	x
S02-3	x	X	x	x	x	x
S02-4	x	X	x	x	x	x
S03-1	x	X	x	x	x	x
S03-2	x	x	x	x	x	x
S03-3	x	x	x	x	x	x
S03-4	x	x	x	x	x	x
S04-1		X			x	
S05-1		X			x	
S06-1		X			x	
Excitation Level:	200mV			200mV		
L01-1		X			x	
L03-1		X			x	
S03 w/ PZT		X			x	

in the chamber. A first set of tests were accomplished that turned out very poor. There was a lot of cross-talk between the modes and significant noise.

Tests were run with and without the heater canister. It was found that additional modes were being introduced by the heater canister. Figure 3.38 shows the new modes that were added. Rubber gaskets and a viscoelastic damping layer were placed between the bracket and the base plate and the tests were re-accomplished. There was little improvement. Approximately 20 pounds of lead weight were placed on top of the mounted plate in hopes of damping out the additional modes and noise. This also showed little improvement. Finally, approximately one inch of rubber was

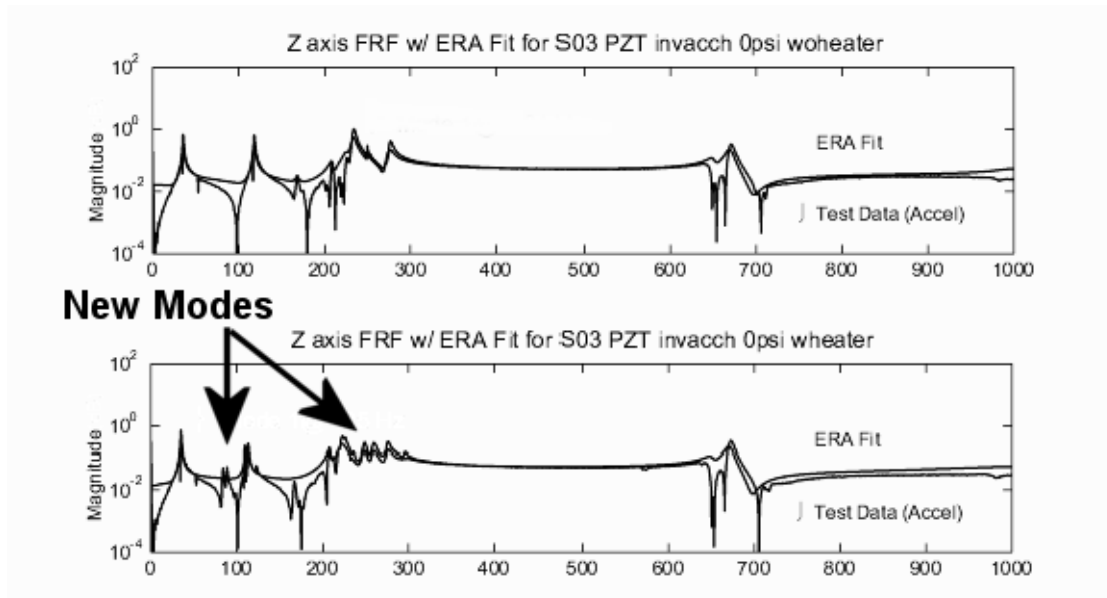


Figure 3.38 Beam S03 in Vacuum Chamber with no damping applied to the structure.

placed between the bracket and the base plate. This produced much better results and this was the final configuration chosen to conduct the remainder of the tests.

The first test in the vacuum chamber used the PZTs for excitation in the vacuum chamber in ambient pressure. The heater canister was used to heat the beam. Tests were accomplished at 25, 35, and 45°C. The next set of tests used the PZTs for excitation in the vacuum chamber in a vacuum. The beam was allowed to vent so that there was a near-vacuum on both sides of the beam walls. It was expected that with the removal of the damping effects of the atmosphere, that the damping ratios would decrease. The heater canister was used to heat the beam from 25°C to 95°C in increments of 10 degrees.

As the beams were heated, they became much softer. The damping increased as the beams were heated. Tests were run at 10 degree intervals to try and establish a trend. The natural frequencies also shifted lower. Table 3.7 shows the testing parameters for the vacuum chamber tests.

Table 3.7 Vacuum Chamber Test Matrix, Excitation level-40V

Temperature	Ambient				Vacuum	
	Pressure Level in Beam					
	0 psi	2 psi	4 psi	6psi	0 psi	4 psi
25 C	X	X	X	X	X	X
35 C	X		X		X	X
45 C	X		X		X	X
55 C					X	X
65 C					X	X
75 C					X	X
85 C					X	X
95 C					X	X

Additional tests for higher temperatures in ambient conditions in the tank were not possible because the heaters did not have the capacity to heat higher than about 50 degrees in ambient conditions.

Figure 3.39 shows beam S03 mounted in the chamber prior to testing. Figure 3.40

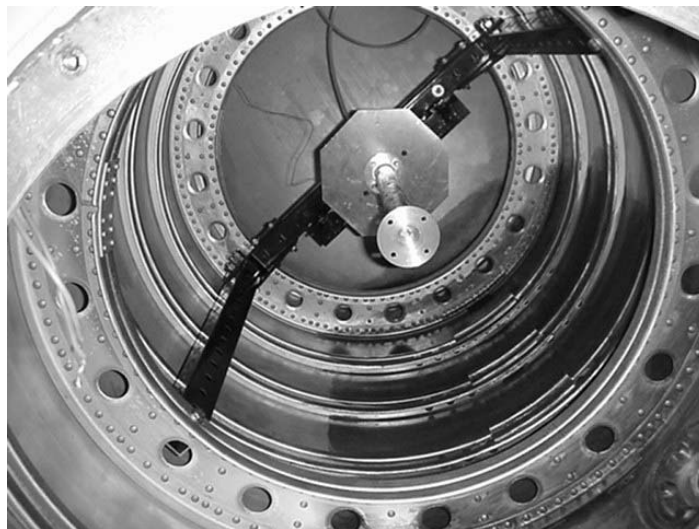


Figure 3.39 Beam in vacuum chamber without the heater canister installed.

shows beam S03 mounted in the vacuum chamber with the heater canister.

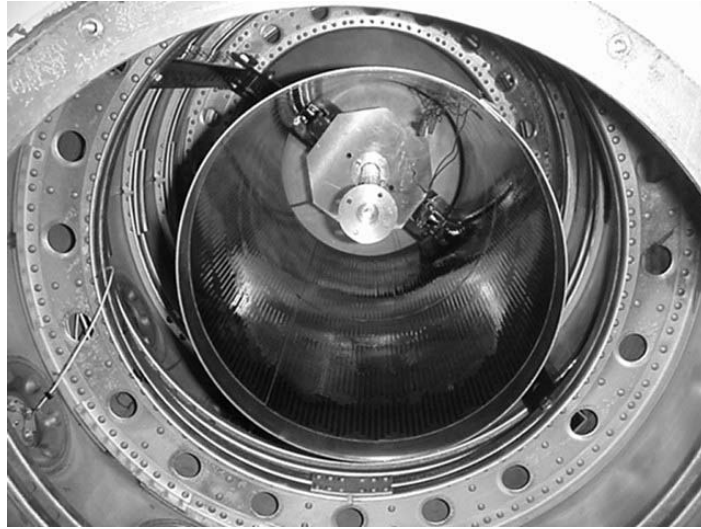


Figure 3.40 Beam S03 in vacuum with heater canister installed.

3.6 Modal Analysis Using ERA

To find the natural frequencies and damping ratios, a program written in MATLAB by then Captain Richard Cobb of the Air Force Research Laboratory[7] was used. The EZERA routine, EZ Eigensystem Realization Algorithm (EZERA), uses a transfer function vector from the vibration testing along with the frequency vector to create a state-space model which can be used to make a curve fit to the FRF and find the natural frequencies and damping ratios.

The eigensystem realization algorithm (ERA) is based on the singular value decomposition of the block Hankel matrix. The original development of the ERA algorithm is given in Juang and Pappa[7]. Figure 3.41 shows user interface with the ERA program, with a sample run. ERA uses FRF data to compute the impulse response functions necessary for ERA from an inverse Fourier Transform on the FRF data.

The LH factor parameter is used to determine the size of Hankel matrix to construct. Typical values range from 6-20. The resulting Hankel matrix $n \times n$. Increasing the LH improves accuracy when using noise corrupted data, at the expense of increased computational burden. A value of 15 was used for the analysis.

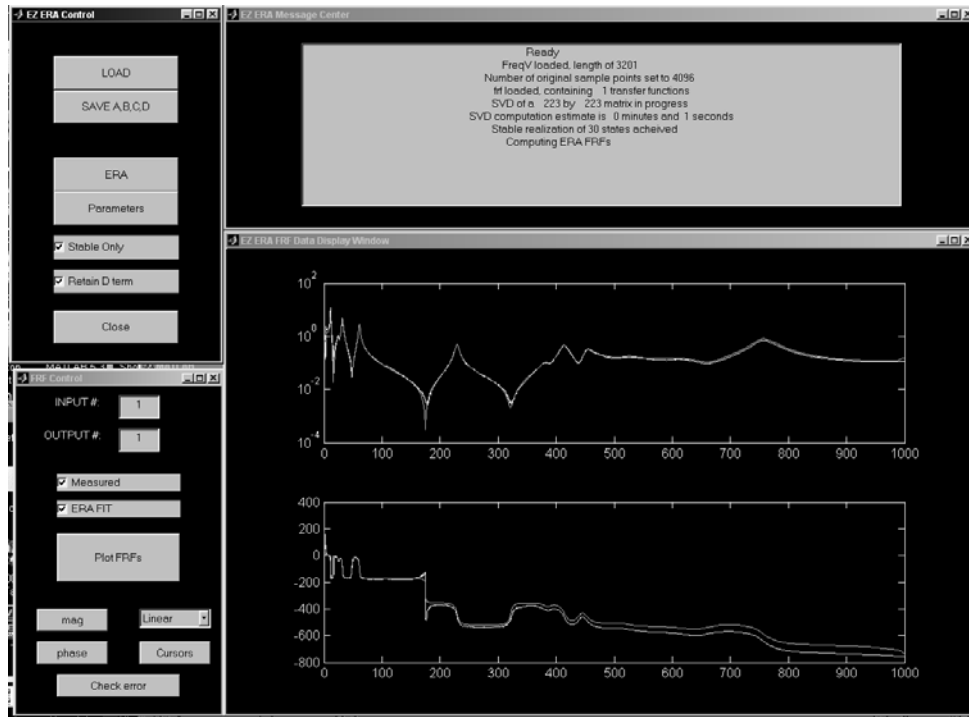


Figure 3.41 ERA Program

The NDPTS parameter is the number of original sample points of the FFT (ie 2^N , 512,1024,2048) set to zero for no padding. Typically, only 80 percent of the data points are contained in the FRF measurement. The remaining 20 percent are discarded because of aliasing. Thus for the 3201 point FFT, the NDPTS was set to 4096 to realize a discrete system with a sample rate which matches the sample rate of the sampled data.

Two variables are required for the program, “fir” and “FreqV”. These two variables are required in the workspace, and were loaded into the workspace using the EZERA control panel. The parameters were adjusted as necessary for each set of data. ERA was performed, along with a curve fit. The program creates the state-space matrices required to calculate the natural frequencies (ω) and damping ratios (ζ). A routine included with the program accomplished these calculations. The resulting ω and ζ values were saved into Microsoft Excel for use in the analysis.

3.7 Summary

In this chapter, the beams were described, and their material properties were presented. The experimental procedure was outlined and a detailed description of the experiment setup was shown. An analytic model for the bending modes of the beam was then developed. A summary of the tests to be performed was listed and the EZERA program was introduced. The next chapter will present the results of the experimental testing.

IV. Experimental Results and Analysis

The results and modal analysis of the vibration testing of the inflatable beams are presented in this chapter. The ambient condition tests conducted using the shaker is presented in the first section. The PZT tests on beam S03 on the test stand are discussed. The long beams are then analyzed, followed by the test stand results. The last section presents the results from the experiments conducted in the vacuum chamber. The bending modes were determined by analyzing the accelerometer and vibrometer FRFs. When analyzing the results, an attempt was made to “line-up” the natural frequencies in the data tables to determine the bending modes.

The following names are used for the remained of the analysis: the tri-axial accelerometer in the tip flange denoted as the “test” or “accel” data, and the laser vibrometer scan point on the centerline of the tip flange is called “vibrometer”. Figure 4.1 shows a sample plot of the FRF of the accelerometer and the vibrometer for beam S02 at 0 psi. The FRF is very similar for all of the short beams mounted on the shaker. The difference in magnitude is due to the fact that the acceleration

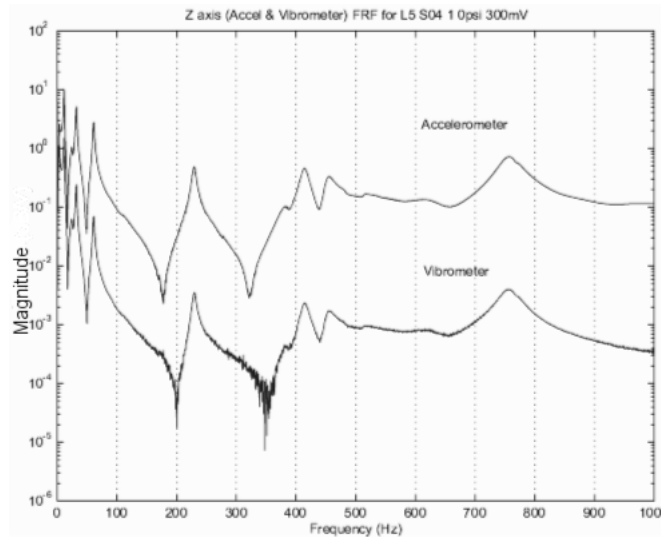


Figure 4.1 Sample of Results from MATLAB of FRF of Accelerometer and Vibrometer

data from the accelerometer is the time derivative of the velocity. The mobility data (velocity) from the vibrometer drops off at 20 dB per decade. However, the figure shows that the accelerometer and the vibrometer generate similar transfer functions and that the peak frequencies are at nearly same frequency. Therefore, the acceleration FRF data from the accelerometer at the beam tip and the velocity FRF data from the laser vibrometer were used for comparisons of the peak frequencies.

Figure 4.2 shows each axis from the accelerometer. The z axis is in the direction of the bending. The graph shows that the lower modes are closely correlated (which are the modes due to the shaker which will be discussed later). The x axis is the vertical direction and is also closely coupled, however, the y axis is not as closely coupled due to the fact that it is measuring acceleration for a motion that is perpendicular to itself.

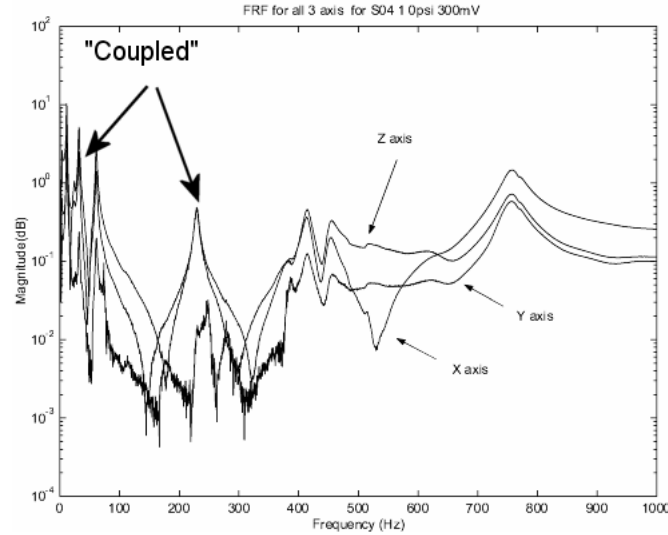


Figure 4.2 FRF for X,Y,and Z axis of S04

The data acquisition system was used to collect the transfer functions of each test. The data was then loaded into EZERA, and a continuous realization using 30-45 states was used to produce the state-space matrices A,B,C, and D. ERA was used to create a curve fit for the magnitude and phase. A routine from ERA was used to calculate the mode number with the corresponding natural frequency (ω) and

the damping ratio (ζ). A routine was written in MATLAB to use in conjunction with EZERA to provide the coherence data and provide the necessary plots. The omega and zeta data for all of the experiments was analyzed using Microsoft Excel. A sample graph of the curve fit done by ERA is shown in Figure 4.3. ERA does a good job of fitting the experimental data.

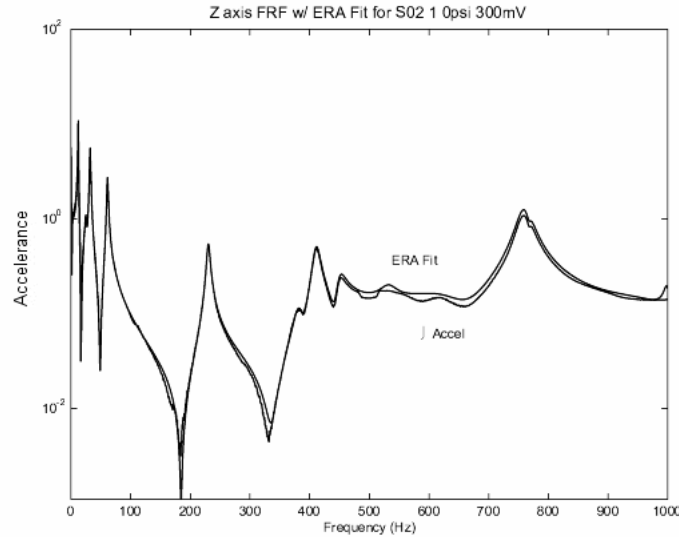


Figure 4.3 FRF ERA fit for S02-1 at 125mV and 0psi

Figure 4.4 shows the FRF (magnitude and phase) and the coherence. The coherence shown compares the reference signal (either the base accelerometer or the excitation signal) and the Z axis of the tip accelerometer. The coherence will always lie between 0 and 1 because it is the ratio of two transfer functions. If the measurements are exactly the same, the coherence should be equal to one. Therefore, the coherence is a measurement of the noise in the signal. If it is zero, the measurement was pure noise, if it is one, it is without the contamination of noise. The coherence was taken versus the frequency span of the transfer function. In the valleys between the peaks, the signal to noise ratio drops off significantly causing a decrease in the coherence. The figure shows that where there is a very low signal that the coherence is very poor.

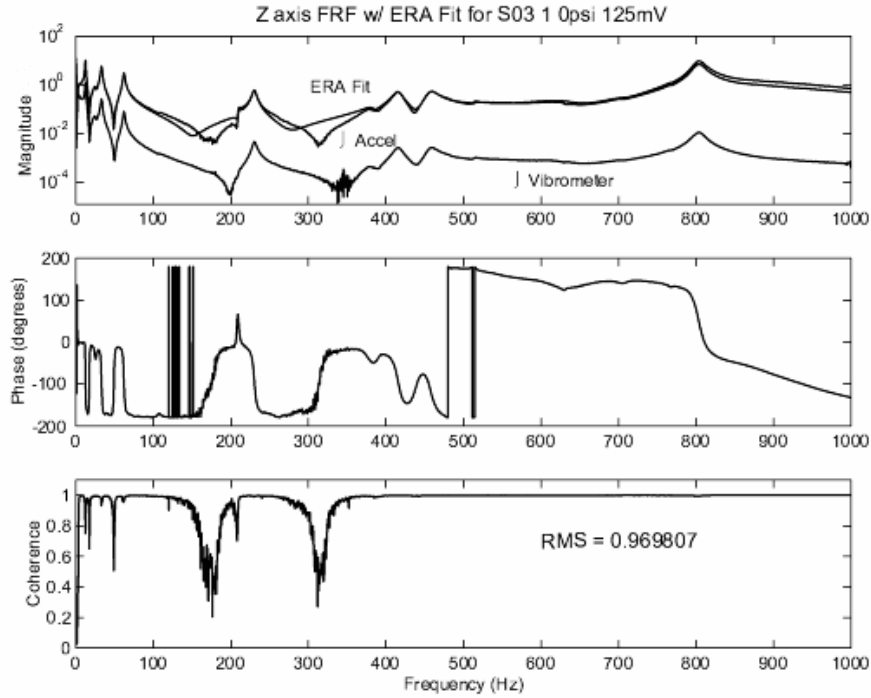


Figure 4.4 Sample of Results for FRF, Phase, and Coherence from MATLAB (using EZERA data)

All of the experiments provided similar results; consequently, only points of interest will be presented, the reader is referred to Appendices for additional data. The figures that follow will be graphed with various frequency spans depending on result being presented; however, all the experiments were acquired using a frequency span of 0 to 1000 Hz.

4.1 Shaker Tests Results

As outlined in Chapter 3, the first set of experiments were in ambient conditions using a shaker mounted on a test stand. This section presents the results for the short beams: S02, S03, S04, S05, and S06. Detailed data will be presented on beams S02 and S03 in order to characterize the beam properties. Representative samples for the remaining beams will be shown. Reference the Appendices for more details and data on the beams.

4.1.1 Short Beams. The five short beams were tested first. The acceleration of the tip and the velocity measurement from the vibrometer were measured. The PSV vibrometer used a scan that took 10 averages at each of the scan points. Between 50 and 130 scan points were used during the testing. By using all of the points together, an averaged transfer function for the beam can be made. The PSV program also renders a 3D model of the test specimen. The peak frequencies for the entire beam model can be calculated and the mode shapes can be determined by observing an animation of the 3D model. Several types of scan point meshes and densities of the meshes were experimented with to find the minimum number of points necessary in order to get an accurate calculation of the peak frequencies. It was noted from the testing that all of the transfer functions are closely correlated for most of the different tests, except for the higher frequencies where there is more damping. Figure 4.5 shows the FRFs from PSV plotted for 0 and 4 psi. The 4 psi curve is annotated, with the 0 psi curve being the other. Due to the noise level and close correspondence, it is difficult to determine the different curves in black and white. In color the two curve lines are more easily discernable. Only in the range of 600 to 800 Hz are the two pressure levels different in the FRF. In this higher frequency, damped region, it is difficult to determine if a “breathing” or torsional mode of the beam is creating this difference.

Table 4.1 is the frequency peak data that was calculated from PSV software. Since the FRFs are somewhat “noisy”, a bandwidth is specified, from which the peak frequency is calculated.

The peak frequencies were calculated for each beam. Table 4.2 shows the results for the testing on the short beams. The first three bending modes are shown. Due to the noise levels, some extra modes were calculated. Beam S02 did not seem to produce the peak frequencies that the other beams did, and was one of the reasons S02 was not selected for testing with the PZTs.

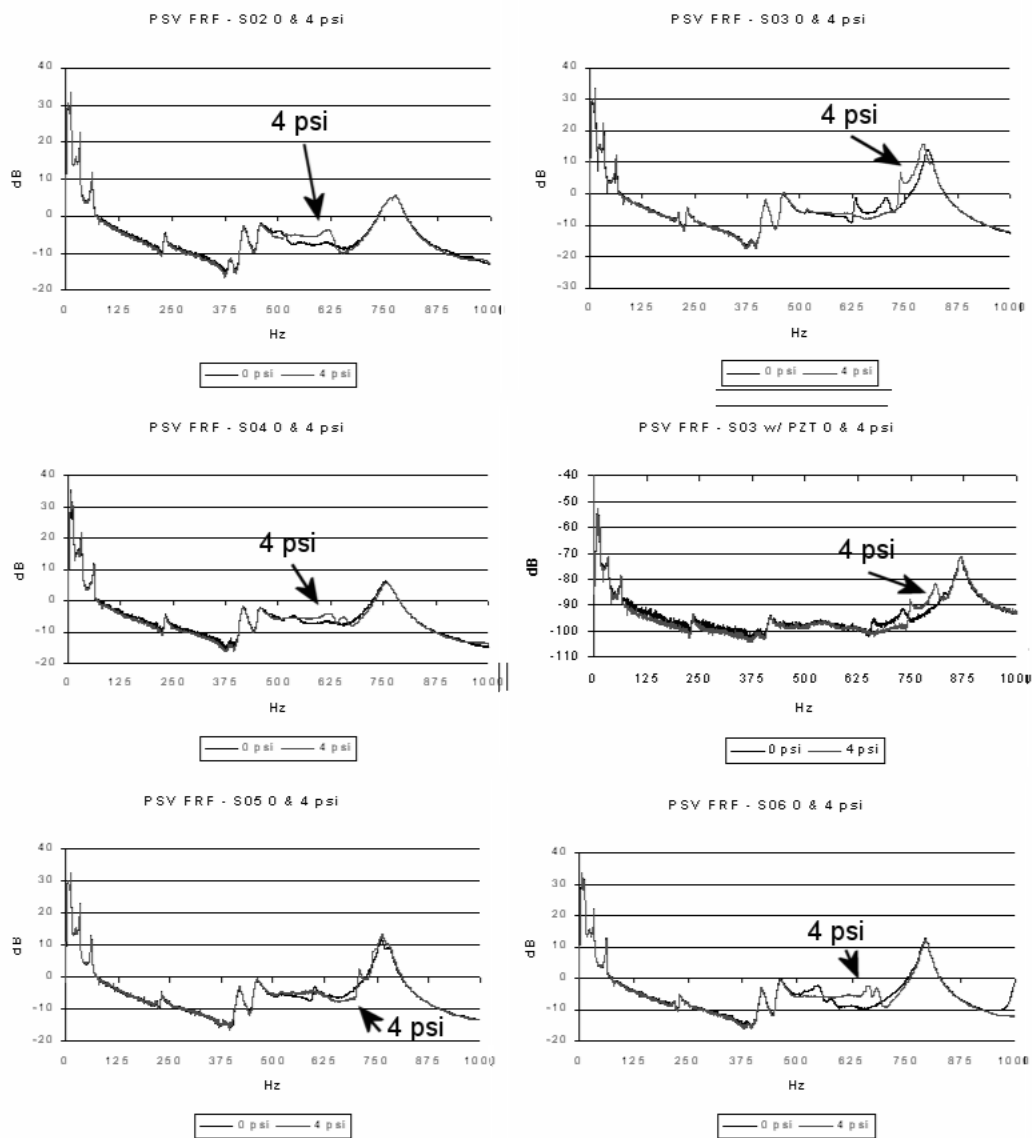


Figure 4.5 FRFs from PSV - Short Beams

Table 4.1 Short Beam Peak Frequency (Hz) calculated from PSV for S02-2 @0 psi

Band	Start	End	Peak	Bandwidth
1	1.5625	8.125	5.9375	6.5625
2	9.0625	17.8125	12.1875	8.75
3	23.4375	39.6875	32.1875	16.25
4	51.25	68.75	61.25	17.5
5	207.813	253.438	232.188	45.625
6	366.875	403.75	387.188	36.875
7	405.938	440.313	418.75	34.375
8	446.25	483.75	459.375	37.5
9	492.188	532.5	503.438	40.3125
10	542.188	575.625	552.5	33.4375
11	590.938	650.625	616.563	59.6875
12	724.063	811.563	775.938	87.5
13	910	973.75	910	63.75

Table 4.2 Short Beam Bending Modes from PSV: Mean Freq. at 0 and 4 psi

	0 psi					
Mode #	S02	S03	S04	S05	S06	Mean
1	32.19	33.13	31.56	33.44	32.19	32.502
2	61.25	61.88	60.63	62.19	60.94	61.378
3	232.19	.	231.25	232.19	230.63	231.565
	4 psi					
Mode#	S02	S03	S04	S05	S06	Mean
1	32.83	32.5	31.88	32.81	33.44	32.692
2	61.88	61.25	60.94	61.25	62.19	61.502
3	231.88	230.94	230.94	230.31	232.19	231.252

The transfer function files from PSV were imported into ERA and MATLAB for processing. ERA produced the natural frequencies and damping ratios. The data was then summarized into tables for easy comparison. Comparison graphs of the results from the data tables were made. Table 4.3, provides an example of the values that were calculated by PSV as compared to the ones from ERA and the accelerometer. It can be seen, as expected, that the peak frequencies have a very small standard deviation. The previous testing showed a close correspondence between the accelerometer and the vibrometer. This comparison shows that two different experimental methods of finding the natural frequencies were successful and the results provided should be considered the true values. Since the mode shapes cannot be determined from the tip accelerator alone, the vibrometer scan must be

used, and the results should be accurate. Once again, the difference between the two pressure levels was negligible.

Table 4.3 Short Beam Omega Values from PSV and ERA at **0 and 4 psi**

Mode#	PSV 0 PSI							
	S02				S04			
	Omega (Hz)				Omega (Hz)			
	PSV	ERA	STDEV	Zeta (%)	PSV	ERA	STDEV	Zeta (%)
1	32.19	32.12	0.05	2.16	31.56	31.63	0.05	2.43
2	61.25	61.26	0.01	1.8	60.63	60.87	0.17	1.67
3	232.19	230.22	1.39	1.19	231.25	229.59	1.17	1.27

The natural frequencies and damping ratios have now been accurately determined for all of the short beams on the shaker. The results from PSV and ERA for the first four modes are shown in Table 4.3. The difficulty is in identifying the bending modes because we do not have the mode shapes for which the experiment was conducted. The PSV 3-D models can be analyzed to try and find the bending modes. This however, proved extremely difficult. The shaker is translating the beam significantly more than the bending displacement of the beam. Additionally, collecting modal data at low frequencies is difficult due to the fact that the lowest detectable limits of the test equipment corresponds with a low frequency mode identified from above. There are several consistent and clear modes at 32, 61, and 232 Hz. These FRFs are very similar to classic cantilever beam FRFs. The following figures show a representation of the model at each mode. The annotations and lines were added for illustrative purposes.

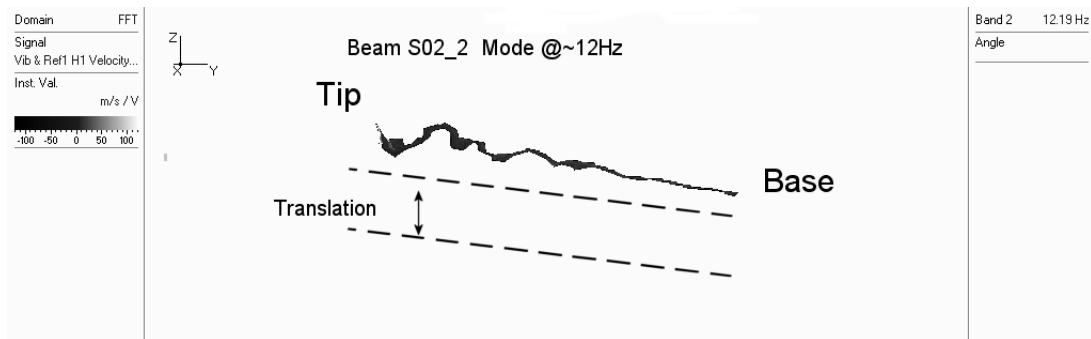


Figure 4.6 PSV 3-D Model @ 12 Hz

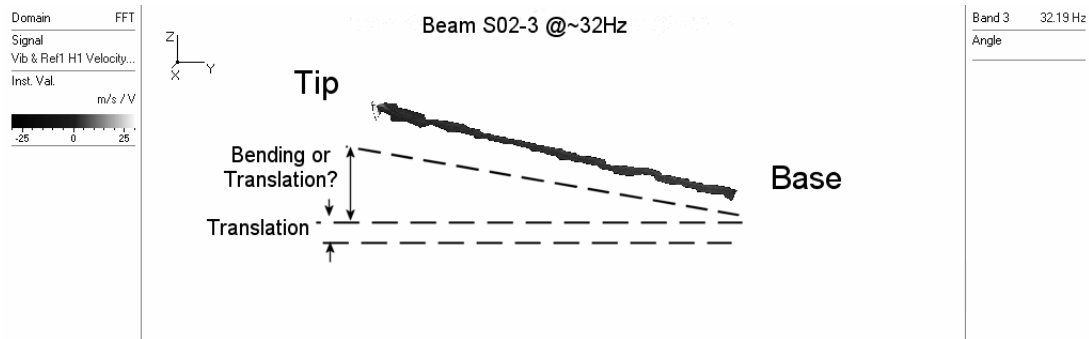


Figure 4.7 PSV 3-D Model @ 32 Hz

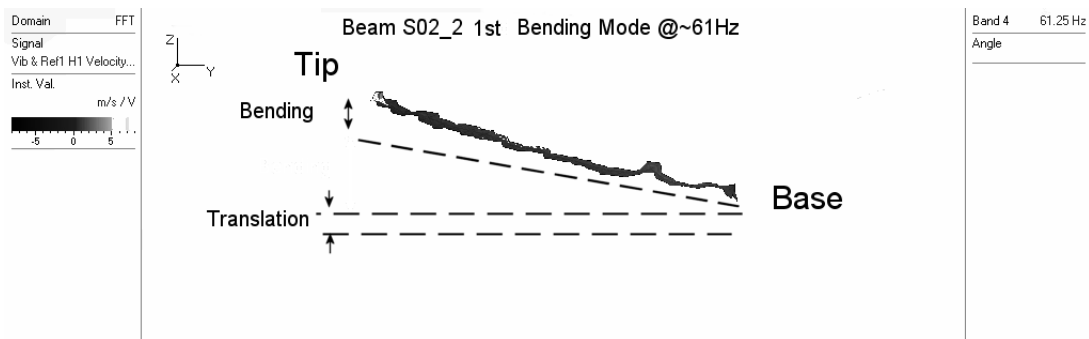


Figure 4.8 PSV 3-D Model @ 61 Hz

The first mode of around 5 Hz was identified early on as being caused by the shaker and is not a bending mode and was not considered. It appears in all of the beams and was disregarded. I have concluded the following from PSV. The 12 Hz mode appears to be a straight translation. The base and the tip move together and there is no bending. Therefore, this is a mode created by the shaker and is not a bending mode. This mode was discarded for the remainder of the shaker tests. The second mode at 32 Hz does show bending properties; however, it is not bending as much as it should for the first mode. It is extremely difficult to tell the difference between the translation and the bending. This does appear to be a candidate for the first bending mode.

The mode at 61 Hz is clearly a bending mode. The base stays nearly stationary while the tip motion is very clear. The mode at 232 Hz is similar to the classic second bending mode of beams. It would appear that the shaker imparts the lower

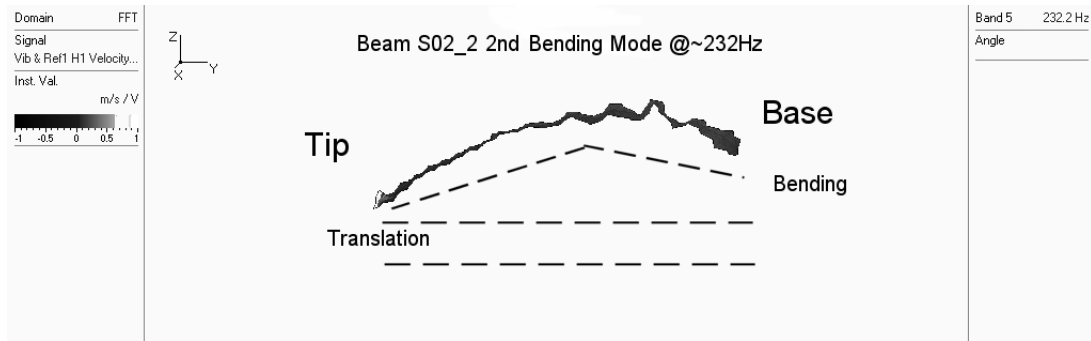


Figure 4.9 PSV 3-D Model @ 232 Hz

“translation” modes. From the 3-D models from PSV, the first two bending modes appear to be at 61 and 232 Hz respectively. However,

Using the peak frequency data and the FRFs, the first three bending modes are at approximately 32, 61, and 231 Hz. The 3-D models at 32 and 61 Hz do not clearly show the bending of the beam as they should appear from the modes shapes predicted by the analytic model. However, using all of the data available, the first three bending modes appeared to be the ones listed above. Beam S03 was selected to have the PZTs mounted to it. One of the primary reasons was the smooth, consistent surface. The PZTs were mounted as described in Chapter 3. The next section discusses the tests run with S03 with the PZTs.

4.1.2 PZT tests with Beam S03 on the Shaker. Using the shaker proved extremely difficult to identify the first two bending modes. PZTs will be used on the flight test; consequently, the remainder of tests will focus on using the PZTs. The beam was tested on the shaker to determine what changes the PZT made. In a later test, the beam was mounted on a test stand on a rigid bracket that was used in the vacuum chamber. This removed the effects from the shaker.

The FRF for the beam mounted on the shaker with the shaker providing the excitation is shown in Figure 4.10. This is very similar to the FRFs of the other short beams. The additional weight and stiffness did not greatly effect the results.

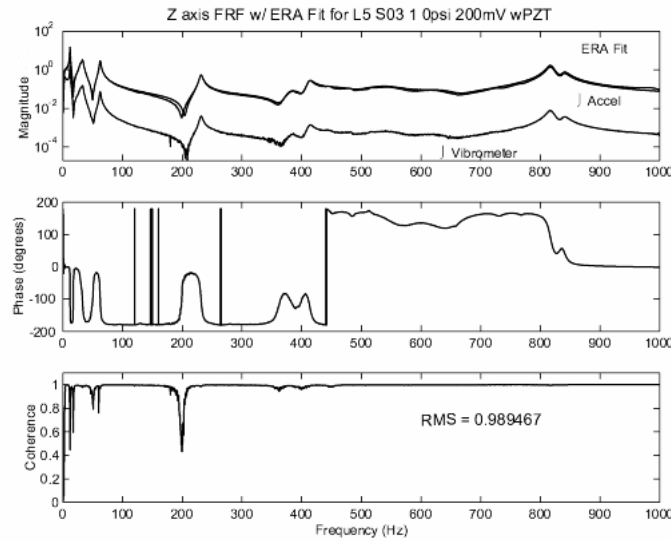


Figure 4.10 Z axis FRF for S03 with PZT on shaker at 4 psi (Shaker exciting)

Test data was collected for the shaker providing the excitation (300mV) for 0,2,4,and 6 psi. With the beam mounted on the shaker, the PZT was used to excite the beam. The FRF, phase, and coherence are shown in Figure 4.11. Data was collected at 0 and 4 psi. The shaker allows the beam to move when the PZT is exciting the beam. Using the PZT for excitation caused a lot of noise at the low frequencies. The FRF is very different. A set of coupled peaks developed around 400 Hz, which is different from the set of smaller peaks that were previously at slightly lower frequencies.

Table 4.4 lists the natural frequency and damping ratio values for the first three bending modes for the two test configurations. The peaks and damping are within a few percent of each other.

Table 4.4 S03 with PZT Omega Values at 4 psi from PSV and ERA

Mode#	Shaker exciting			PZT exciting		
	Omega(Hz)		Zeta (%)	Omega(Hz)		Zeta (%)
	PSV	ERA		PSV	ERA	
1	33.4	33.13	4.85	33.7	31.38	6.28
2	62.5	62.41	1.6	63.4	63.63	3.38
3	231.9	231.43	1.08	230.9	231.3	1.11

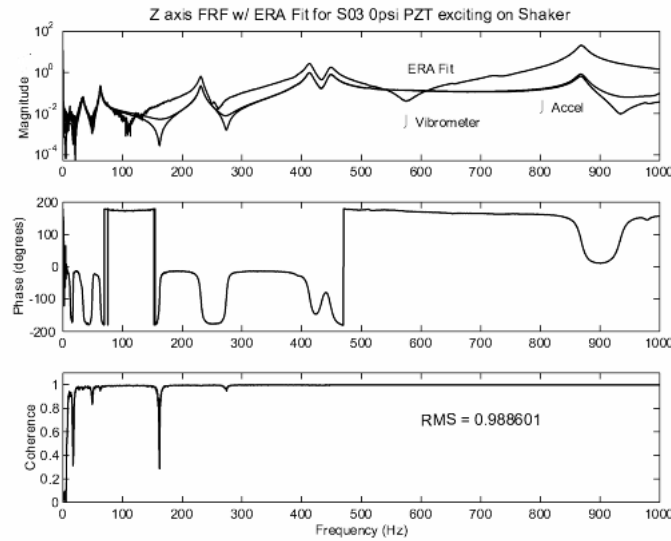


Figure 4.11 Z axis FRF for S03 with PZT on shaker at 4 psi (PZT exciting)

4.1.3 Long Beams. The long beams (L01 and L03) were mounted to the shaker on the test stand. Beam L02 was not used due to a leak in the beam wall. The tests were conducted at 0, 2, 4, and 6 psi. The excitation level had to be reduced to 200mV in order to keep the noise levels low. The FRFs for the long beams are shown in Figure 4.12 at 0psi. The graph shows that the modes are very similar and ERA had no problem fitting the curve to the test data.

Once again, there is very good correlation at the first four modes, with the higher, damped modes losing correlation for 0 and 4 psi, as shown in Figure 4.12. As expected, the higher pressure shifts the frequencies higher. The first three modes are summarized in Table 4.1.3.

It should be noted that the laser vibrometer was too close to the long beam for accurate results. This was due to the physical limitations of the laboratory. Due to the close distance, there was a large angle created when scanning the top and bottom portions of the long beams. This high angle lowers the signal to noise ratio and produces a scan point that is less than optimal and sometimes is only marginal. This skews the model that is made in the PSV program and may explain why the

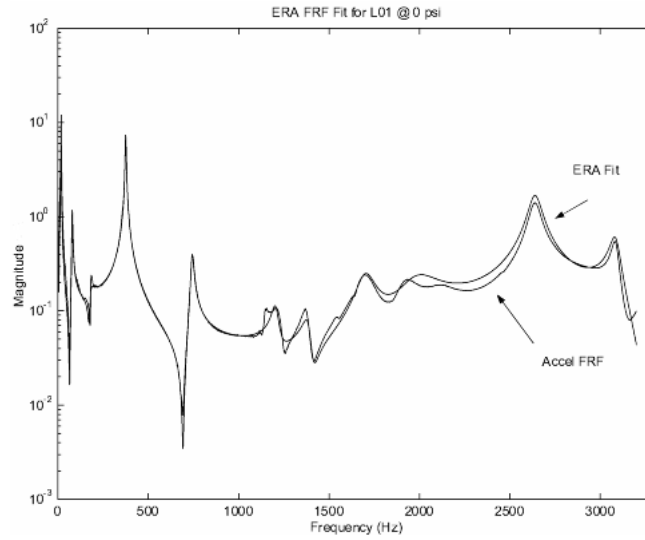


Figure 4.12 FRF ERAfit L01 0psi

Table 4.5 Long Beam Omega Values from ERA and PSV at 0 and 4 psi

Long Beams Bending Modes @ 0 psi						
Mode #	L01			L03		
	Omega(Hz)		Zeta (%)	Omega(Hz)		Zeta (%)
	PSV	ERA		PSV	ERA	
1	5	24.4	2.4	2.5	24.5	1.95
2	116.9	55.4	4.95	115.9	56.8	1.96
3	231.1	117.0	0.7	234.4	115.7	0.46
Long Beams Bending Modes @ 4 psi						
Mode #	L01			L03		
	Omega(Hz)		Zeta (%)	Omega(Hz)		Zeta (%)
	PSV	ERA		PSV	ERA	
1	5	24.4	2.27	5	24.5	2.32
2	117.2	56.7	1.6	116.5	56.95	1.86
3	233.4	116.5	0.65	231.9	116.4	0.46

frequencies do not line up for the bending modes. The modes shown above for the PSV should be viewed with some skepticism. The values from ERA were deemed more reliable and accurate and are assumed to be the correct bending modes. These peak values are lower than the short beams as is expected for the longer beams.

4.2 Test Stand Tests Results

The next step was to mount the beam onto the baseplate and bracket that were used in the vacuum chamber tests. Data was collected at 0 and 4 psi. During the analysis process, the the 0 psi data became corrupted and was not used. The

FRF for the beam mounted on the test stand with the PZT providing the excitation is shown in Figure 4.13. The phase and coherence are also shown. ERA had no problem with the curve fit. The FRF is now quite different. The higher modes are much more damped out and the first three modes are noisy but identifiable. There does appear to be a mode and a lot going on around 700 Hz.

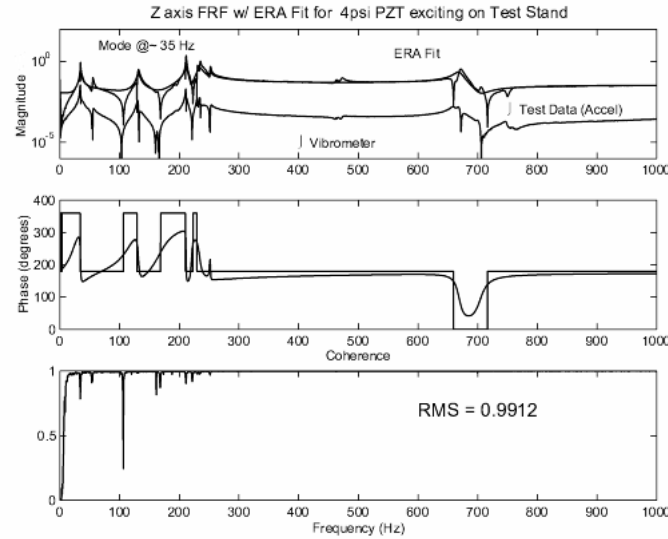


Figure 4.13 Z axis FRF for S03 w/ PZT on Test Stand @ 4 psi (PZT exciting)

This configuration removes all of the effects of the shaker. The test stand is rigid, whereas the shaker allowed significant movement. This should allow the “noise” of the system to be reduced and have only the properties of the beam be a factor. Overall, there is much more noise in the system. Due to the small displacement that the PZT imparts, the data collection was made much more difficult. It should be noted that the PZTs were actuating together (opposite directions) to increase the force being applied to the beam.

Figure 4.14 shows the different PZT test configuration plotted on top of each other. This shows a comparison of how the FRF changed due to the test stand and the different ways of exciting the beam. The plots show that a comparison between the shaker tests and the test stand will not produce accurate results. The

lower modes which in general have a higher magnitude, and the bending modes around 32 and 61 Hz are able to be seen for all of the tests even though they do not correspond exactly. The magnitude of the plots is very low, down to -120 dB. The signal strength was extremely low for the vibrometer when using the PZT for excitation. Consequently, the results are questionable.

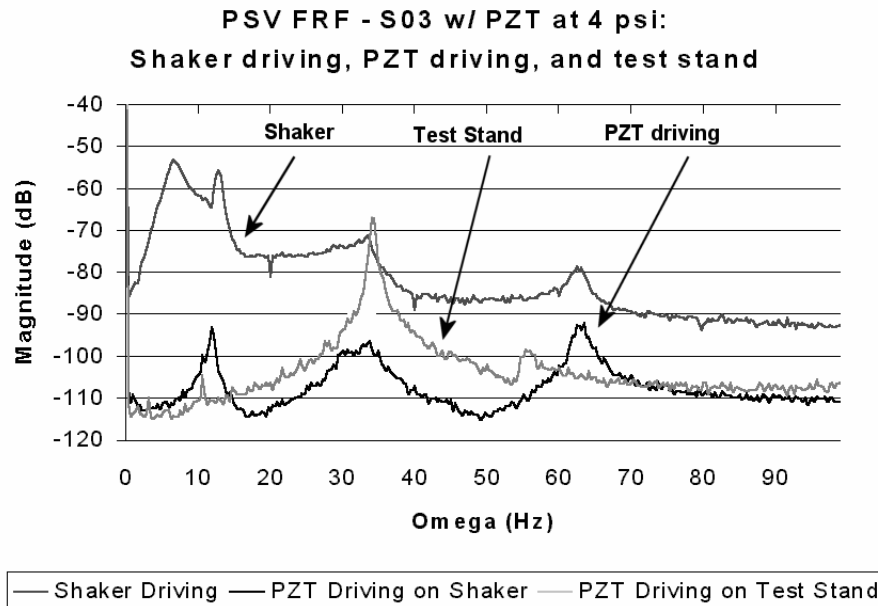


Figure 4.14 Z axis FRF Comparison from PSV for S03 with PZT

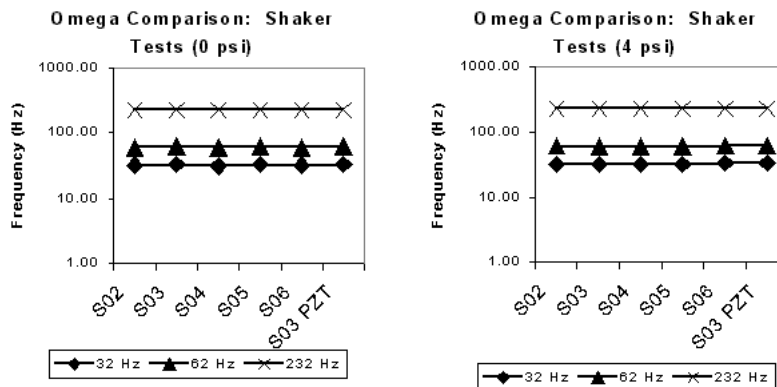


Figure 4.15 Short Beam Comparison of Omega vs Mode

The data collected is presented in the following plots. Figure 4.15 compares the peak frequency for the first three modes of the short beams, using the shaker for excitation. They are almost straight lines and do not show any significant change in the frequency value using the shaker.

The first three modes of 33, 62, and 231 Hz are shown in Figure 4.16 for different methods of excitation. There is almost no change between using the shaker at 0 psi, the shaker at 4 psi, or with the PZT at 4 psi.

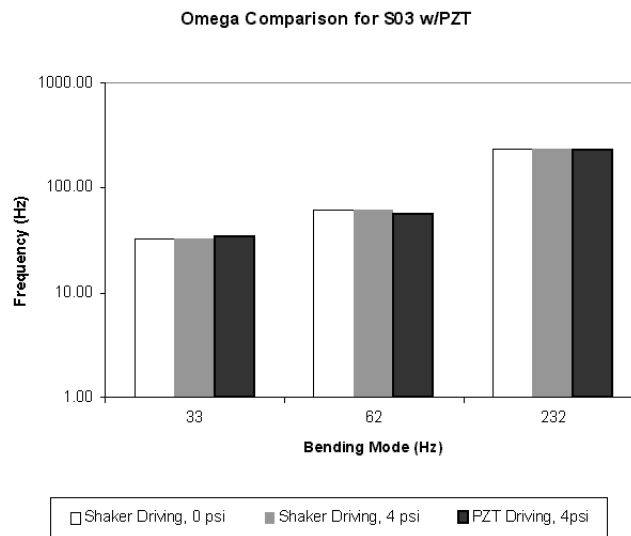


Figure 4.16 Short Beam Comparison of Omega vs Mode for Shaker/PZT driving

The peak frequency and mode numbers are compared for the PZT driving on the shaker and the test stand. Figure 4.17 shows that the after the first three modes, that the values of omega are much higher than that for the beam on the test stand. The significant shift is due to the removal of the shaker arm movement and damping.

The PSV 3-D models were compared to determine the bending modes for beam S03 at 4 psi using the PZT as the exciter on the test stand. This is the configuration that will be used in the vacuum chamber, so identification of the bending modes is critical. The first mode at 34 Hz is acting in bending, with very little torsion. This

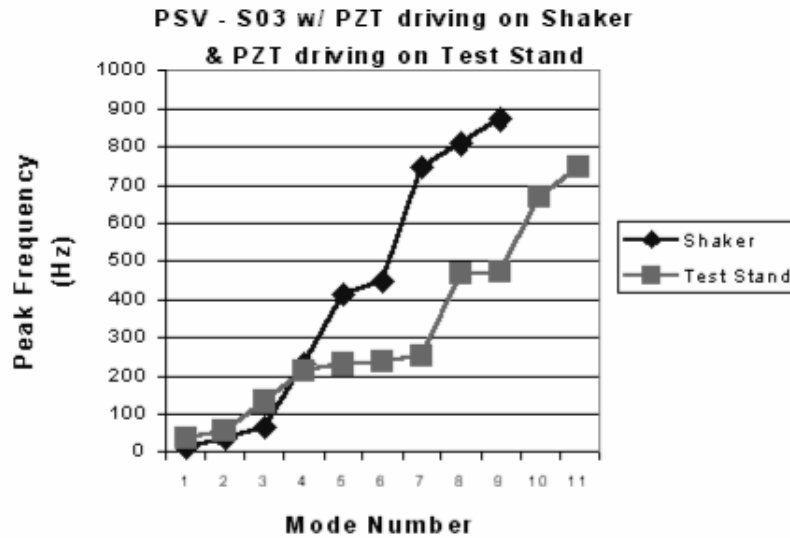


Figure 4.17 Omega vs Mode for Shaker and Test Stand

mode has a zeta value of 1.04%. This is the first bending mode. The second mode at 130 Hz is very similar to the second mode of bending for a beam. There is some torsion acting on the beam, but the mode shape is that of the second bending mode with a damping rate of 1.28%. The mode at 211 Hz is the forth bending mode. There was no torsion, and it behaved exactly as expected for the third bending mode and had a zeta value of only 0.27%. The mode at 230 Hz showed significant motion. The beam was in bending and had a significant amount of twisting. This had a similar mode shape to that of the second bending mode, but with the amplitude greatly reduced and had a zeta value of 0.44%.

The 3-D models show a side view and a lengthwise view. The software program builds a 3-D model that can be rotated in all three dimensions. The scanned points of the mesh that was defined is used to create the model. Any sampled points that were not optimal introduce errors into the model. The different types of modes (bending, torsion, breathing) can be identified by care investigation and comparison of the different peak frequencies. The pure bending modes remain “flat” or horizontal in the pictures, while torsion is shown by the angle of the beam in the different views.

A sampling of the bending modes are shown in the following figures. As can be seen from the figures, identifying the bending modes is extremely difficult and the peak frequencies do not match those of the accelerometer. Therefore, the values of from the accelerometer are probably the true modes and are shown below.

Note that there is very little torsion in the beam from Figure 4.19.

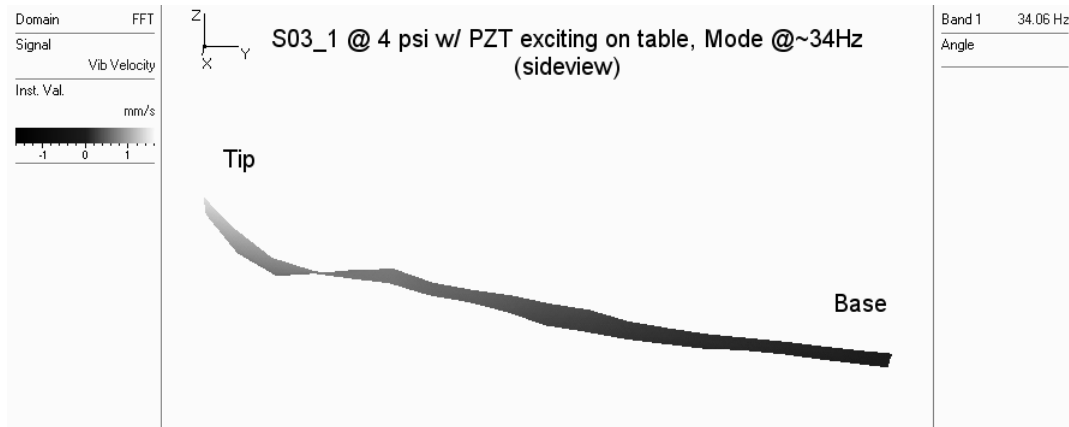


Figure 4.18 PSV - Beam S03 @ 34Hz on test stand with PZT as the exciter (side view)

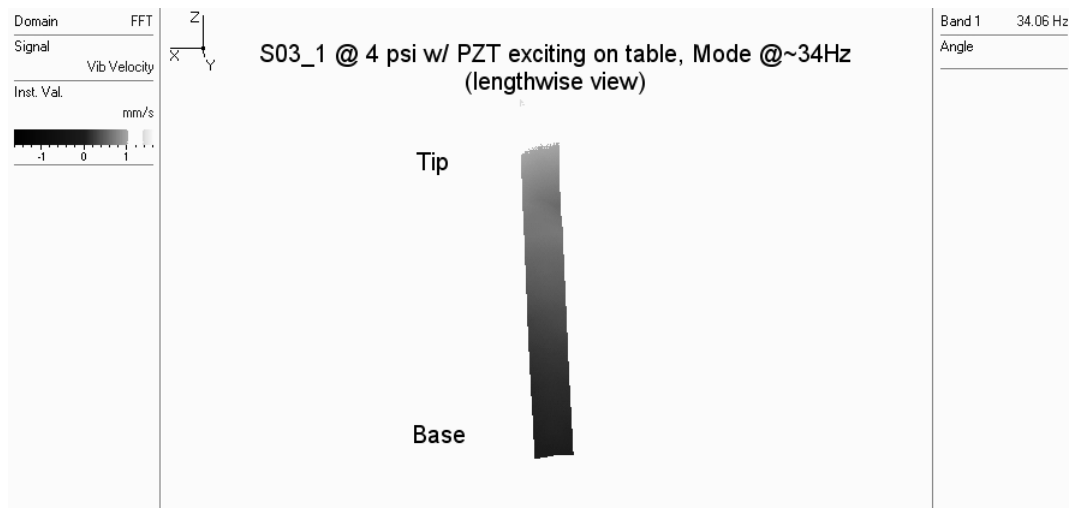


Figure 4.19 PSV - Beam S03 @ 34Hz on test stand with PZT as the exciter (length view)

Although difficult to discern from a single snapshot and not an animation, Figures 4.20 and 4.21 show a bending mode with a slight twisting of the beam.

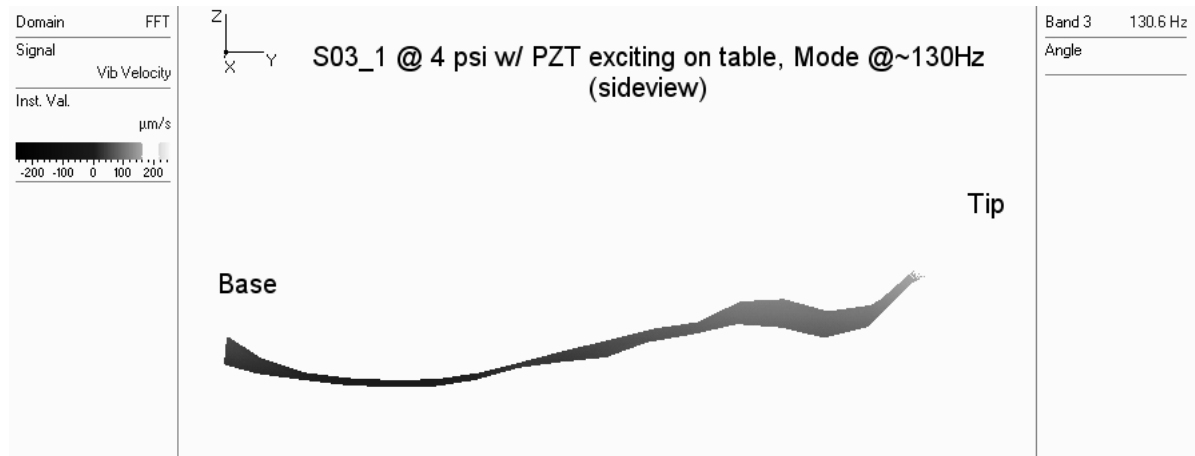


Figure 4.20 PSV - Beam S03 @ 130Hz on test stand with PZT as the exciter(side view)

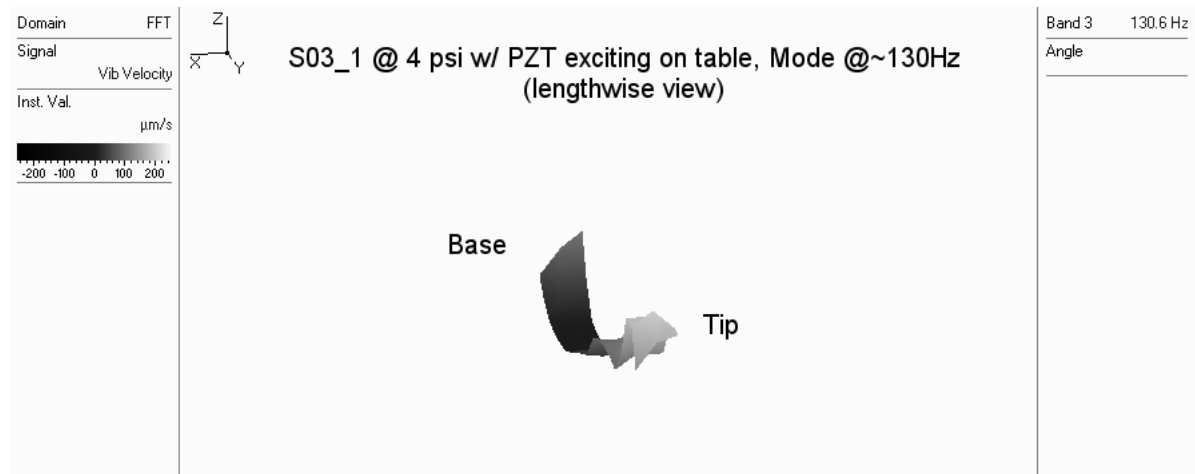


Figure 4.21 PSV - Beam S03 @ 130Hz on test stand with PZT as the exciter(length view)

What appears to be the fourth bending mode is shown in the figures below. Note that there are almost no torsional effects on the beam. This result is close to the prediction of the analytic model.

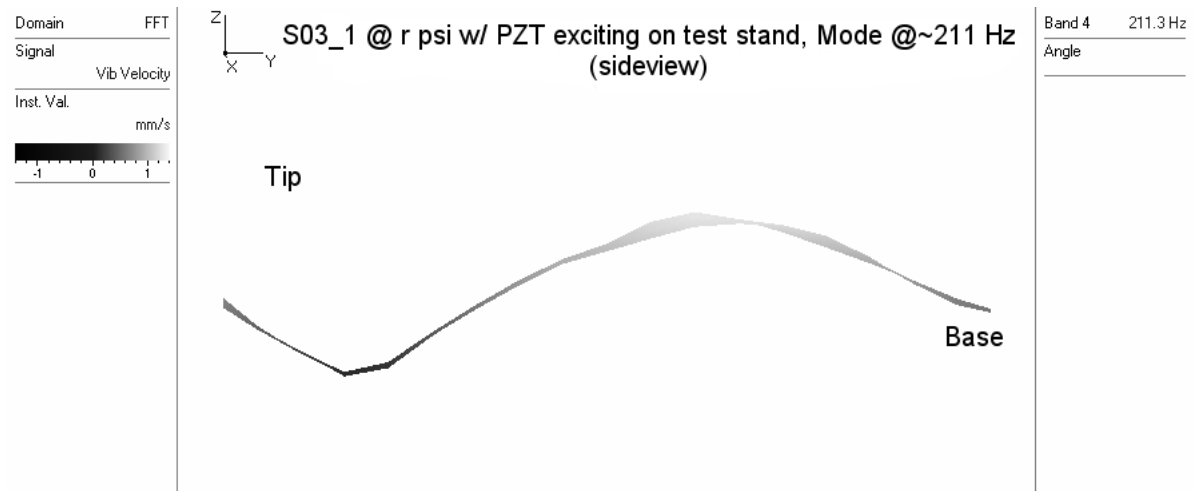


Figure 4.22 PSV - Beam S03 @ 211Hz on test stand with PZT as the exciter(side view)

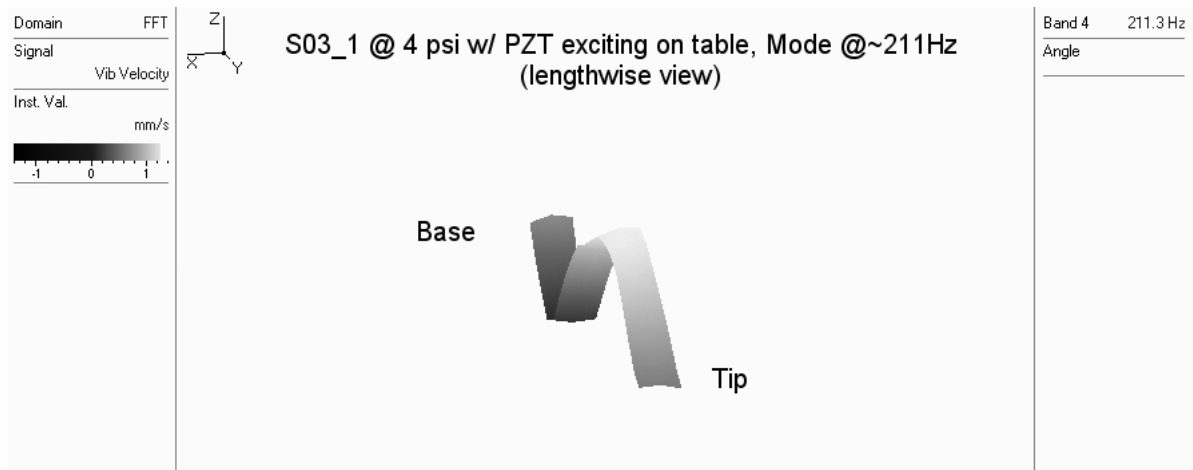


Figure 4.23 PSV - Beam S03 @ 211Hz on test stand with PZT as the exciter(length view)

In Figure 4.24 and 4.25 that there is significant torsional effects on the the beam. This mode is not one of the pure bending modes. These figures are shown as an example of the complicated nature of the modes. This mode near 230 Hz is a bending mode coupled with a torsional mode.

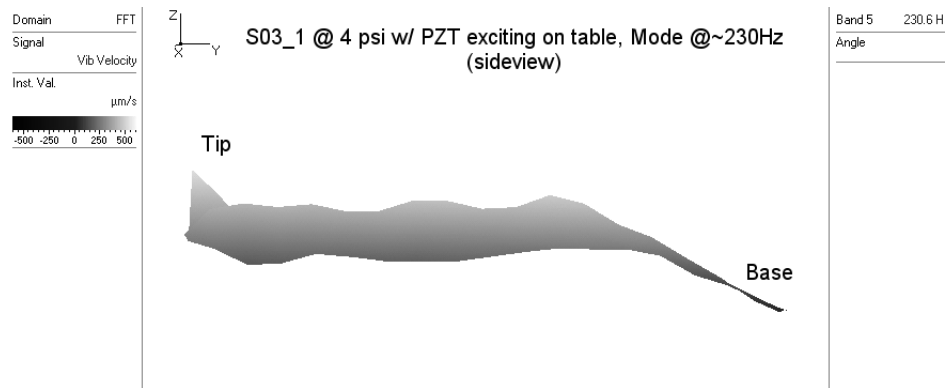


Figure 4.24 PSV - Beam S03 @ 230Hz on test stand with PZT as the exciter(side view)

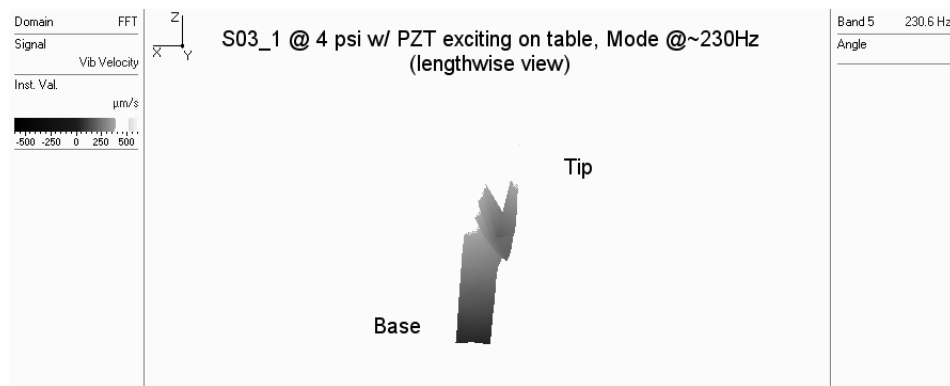


Figure 4.25 PSV - Beam S03 @ 230Hz on test stand with PZT as the exciter(length view)

Table 4-5 lists the values for the natural frequencies for the different PZT tests at 0 and 4 psi. The values were taken from the ERA data because of the low confidence level of the vibrometer data.

Table 4.6 Short Beam Omega Values at 0 and 4 psi for S03 & S03 w/ PZT

Mode#	0 psi		4 psi		
	Shaker Driving	PZT Driving	Shaker Driving	PZT Driving	Test Stand
1	32.76	33.44	32.50	33.44	34.06
2	61.82	62.19	61.25	62.50	55.31
3	229.96	231.88	230.94	231.88	230.63

4.3 Vacuum Testing and Analysis

The final set of tests were accomplished using a vacuum chamber. The beams were mounted to the bracket on the inside. The PZT was used for the excitation. Several changes had to be made to the test setup. The first trials using the PZTs had the beam actuated so that the bending was in a direction perpendicular to the bracket. This introduced a lot of noise. Many new modes were introduced and the FRF was changed significantly. The beam was rotated so that the PZT actuated in a direction parallel with the bracket. This produced a much better result. The increased stiffness decreased the amount of noise and feedback.

It was also discovered that the heater canister produced a mode near 240 Hz. It had significant amplitude to raise concern about the validity of the data. Several methods were employed in order to remove any system feedback and to damp the additionally modes. The final configuration that was selected involved approximately one inch of rubber pads placed between the baseplate and the bracket. This created enough isolation and damping to get good data. The system was tested with both the heater canister and without. The canister is vibrating due to the PZTs and creates noise and additional modes.

Figures 4.26 and 4.27 show the FRF for the beam mounted in the vacuum chamber at 25 and 95C. It is interesting to note that the several lower modes have disappeared and a single distinctive mode appears near 50 Hz. Several locations show pole-zeros resulting in the smaller peaks on the down slope of the main peak frequency. Notice in the higher temperature test that the higher modes are completely damped out.

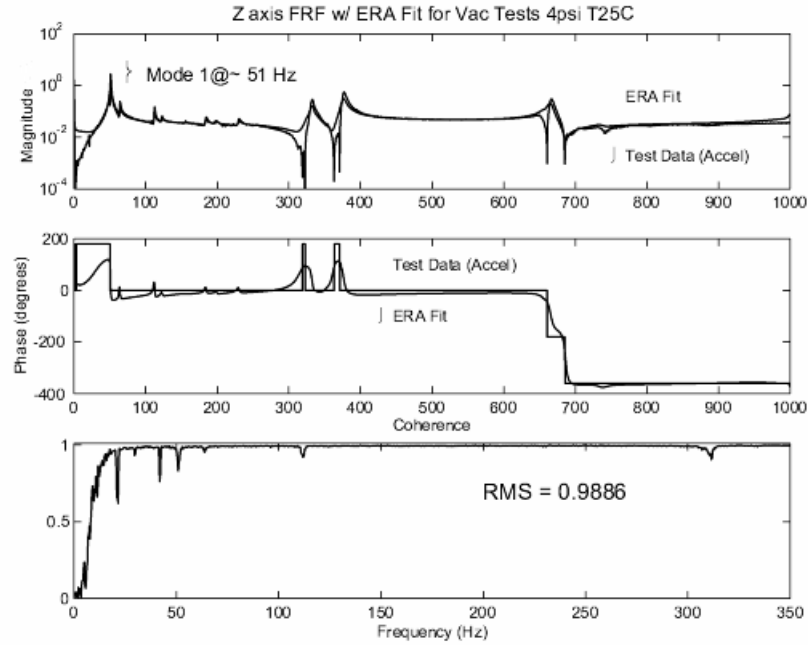


Figure 4.26 FRF for Beam S03 in Vacuum at 25 C

The experimental results are summarized in Table 4.7. The results for the beam in a vacuum with no pressure in the beam and +4 psi in the beam are shown.

Table 4.7 Summary of Vacuum Tests at 0 & 4 psi

Beam w/ PZT in Vacuum - 0psi in the Beam										
Temperature:	25C	35C	45C	55C	65C	75C	85C	95C	MEAN	STDEV
Peak	51.18	51.1	50.81	50.08	49.13	47.74	46.59	45.55	49.02	2.17
Modes (Hz)	64.25	63.78	63.43	62.82	62.61	62.4	62.23	62.15	62.96	0.77
	231.58	231.42	235.05	227.89	229.14	229.26	229.77	222.98	229.64	3.46
Damping	0.74	0.73	0.81	1.24	1.69	1.76	1.76	1.69	1.30	0.48
Ratio	1.18	1.09	1.06	1.4	1.06	1.04	1.07	1.06	1.12	0.12
(%)	1.83	0.77	4.06	3.24	1.53	2.02	1.83	5.88	2.65	1.66
Beam w/ PZT in Vacuum - +4psi in the Beam										
Temperature:	25C	35C	45C	55C	65C	75C	85C	95C	MEAN	STDEV
Peak	50.98	50.92	50.73	50.23	49.33	48.05	46.78	45.77	49.10	2.01
Modes (Hz)	64.09	63.56	63.02	62.72	62.57	62.24	62.19	62.05	62.81	0.72
	.	.	229.53	228.48	227.94	226.81	228.26	227.79	228.14	0.89
Damping	0.77	0.75	0.87	1.08	1.49	1.67	1.71	1.56	1.24	0.41
Ratio	1.28	1.4	1.11	1.04	1.02	0.76	0.61	0.57	0.97	0.30
(%)	.	.	2.22	1.56	1.84	2.2	2.9	2.18	2.15	0.45

The following figures show how the frequency changes with respect to increased temperature. Two frequencies, at 0 and 4 psi, are plotted on each graph for easy comparison. Note that the first frequency, the lower value, is plotted against the

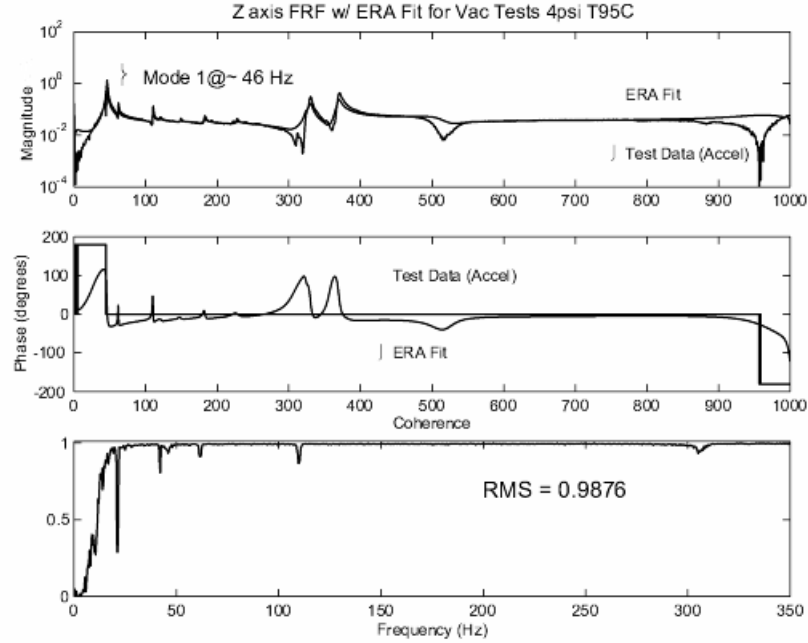


Figure 4.27 FRF for Beam S03 in Vacuum at 95 C

left axis and the higher mode is plotted against the right axis. Figure 4.28 clearly shows the change in the value for each of the modes. The first figure shows a change in frequency between 45 and 65 degrees. This is expected for beams that are being heated. The first mode around 49 Hz shows a slight change in the peak frequency, while the mode that starts around 69 Hz at 25 degrees drops down to around 63.5 Hz. Once again, the effects of the pressurization level of the beam does not seem to be a factor. The damping changes over the temperature range are as expected for the first mode, shown Figure 4.29. The increased heat changes the material properties and makes the beam softer, which is less rigid, and subsequently increases the damping. This occurs between 45 and 65 degrees.

Figures 4.30 and 4.31 show a slight decrease in the amount of damping. The mode around 230 Hz shows a slight increase in the damping.

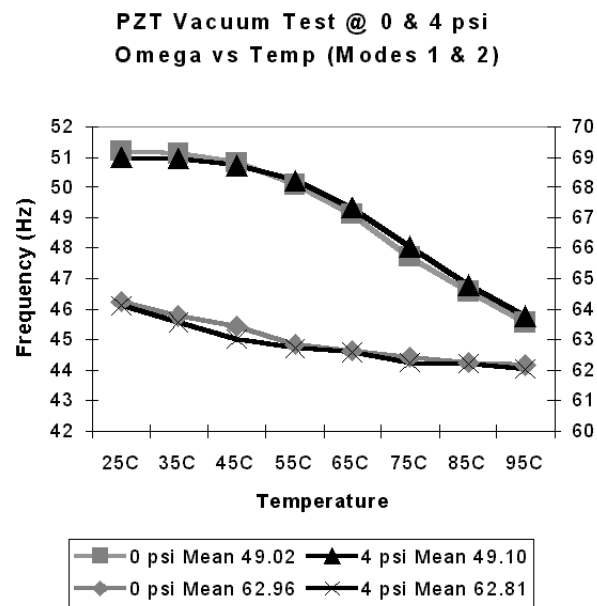


Figure 4.28 Vacuum Comparison of Peak Frequency vs Temperature for Modes 1 and 2

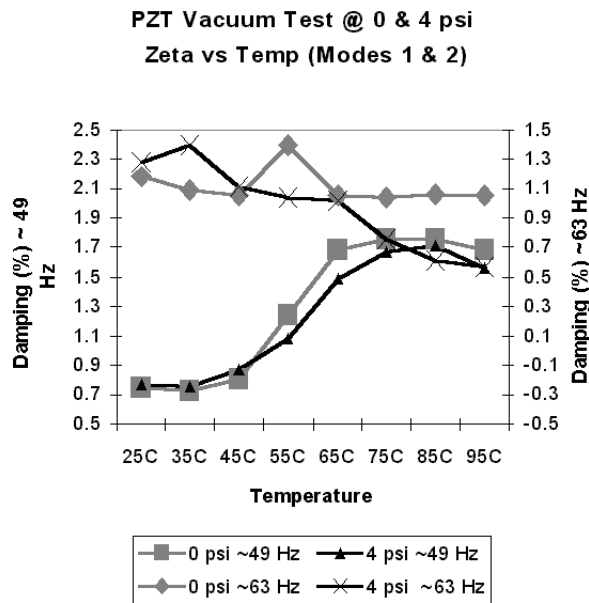


Figure 4.29 Vacuum Comparison of Damping vs Temperature for Modes 1 and 2

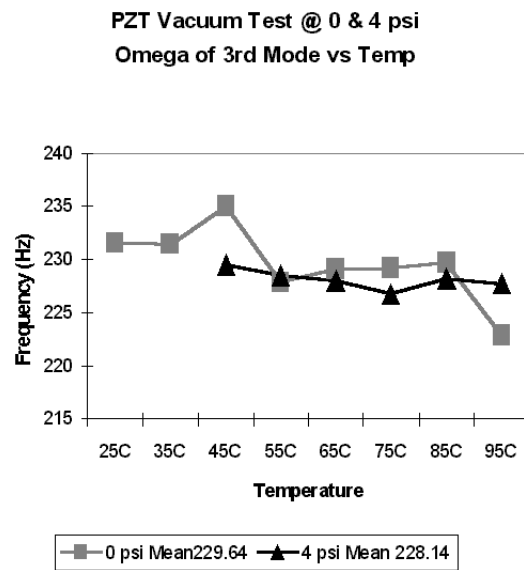


Figure 4.30 Vacuum Comparison of Damping vs Temperature for Mode3

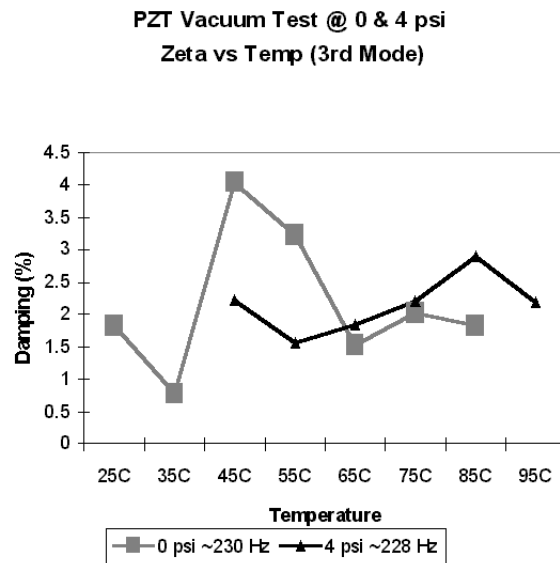


Figure 4.31 Vacuum Comparison of Damping vs Temperature for Mode 3

The next two figures are for 0 psi. Figure 4.32 shows that the natural frequencies are slightly shifted down as the beam gets hotter, softer, and more damped. The natural frequencies are not effected that much by the heat.

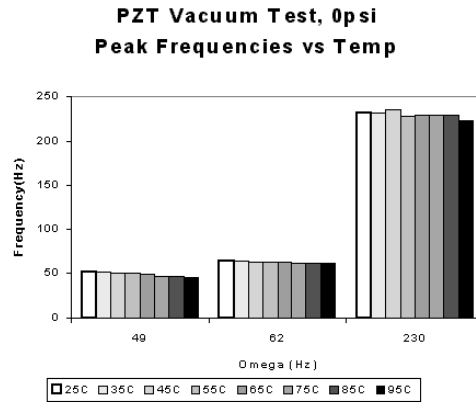


Figure 4.32 Vacuum Comparison of Omega vs Temperature for 0 psi

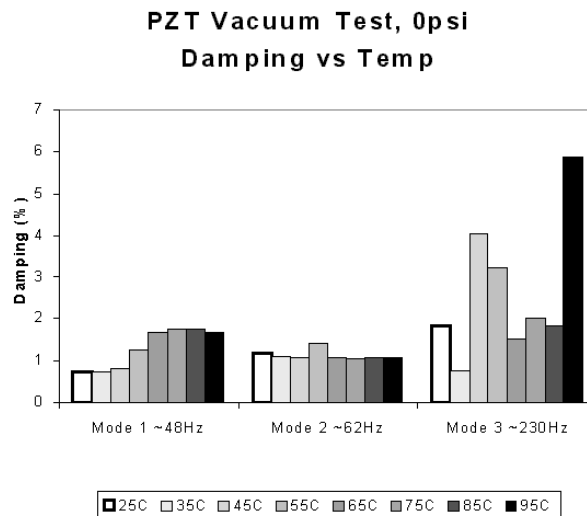


Figure 4.33 Vacuum Comparison of Zeta vs Temperature for 0 psi

The damping for the first mode increase as expected with heating as shown in Figure 4.33. The second mode did not change significantly. The third mode however, varied greatly and without any apparent pattern..

4.4 Comparison to Analytic Results

The different test configurations produced very different results. Comparisons can be made for the tests conducted on the shaker and comparisons can be made between the test stand and the vacuum chamber. However, it is difficult to draw a comparison between the shaker tests and the other tests. The analytic model was developed to predict the bending modes in ambient conditions with the beam clamped to a rigid body. The first mode of 1 Hz that was predicted analytically will not be considered as it is below the reliable threshold for the data collect and cannot be observed. The bending modes that were identified for the beams are similar for the shaker and the test stand; however, they are very different from the analytic prediction and the ambient conditions test in the vacuum chamber. It was expected that the analytic results would have matched closely with the ambient conditions test in the vacuum chamber or on the test stand. The experiments produced reasonable results. The properties of the beams should not change significantly. The different boundary conditions for mounting the beams will slightly change the results. There will be feedback from the structure of course; however, the natural frequencies and the damping ratios of the beam should be consistent. The table shown below summarizes the values of omega in hertz for the first three bending modes for each of the test conditions.

Table 4.8 Summary of Bending Modes for the Short Beams

Mode #	Shaker (PZT driving)	Test Stand	Analytic	Vacuum Chamber	
				Ambient	Vacuum
1	33	32	1	51	51
2	63	63	60	64	64
3	231	231	196	228	232

4.5 Summary

This chapter presented the results of the experimental vibration testing. The mode shapes were difficult to determine from the 3-D model in the PSV program. It was unexpected that the natural frequency modes varied so much between each test

configuration. The heater canister and the vacuum chamber introduced additional modes and noise to the data. The addition of the rubber damping material also effected the data. The analytic model and the experiments are similar, and they are in within a reasonable range for prediction. The FRFs were similar and repeatable between the test configurations. The next chapter will show how each of the test parameters effected the modal characteristics of the beams.

V. Discussion of Results

The results of the test parameters comparisons are shown in the following sections. Comparisons between trials, excitation level, orientation, internal beam pressure, temperature effects, and ambient versus vacuum were made. The beam parameter tests were conducted on the short beams using the shaker. The comparisons are presented, followed by each of the test configurations: shaker excitation , PZT excitation, the beam with the PZT on the test stand, and in the vacuum chamber. Chapter 4 focused on identifying the bending modes; therefore, the other modes were not considered. In this chapter, all of the modes identified, whether they are actual or not are presented to determine how repeatable the test are.

5.1 Beam Characterization Results

Beams S02 and S03 were tested extensively. The excitation levels were changed, the pressure inside the beam was changed, the rotation of the beams was changed for the four possible mounting points, and various laser vibrometer scans were conducted. Three trials for each test were accomplished.

5.1.1 Trial Comparisons. The first parameter to consider was the variation or repeatability between test runs. Figure 5.1 shows three trials run for the same test. The coherence of 0.97 is closely matched between the trials. Figure 5.1 uses the entire frequency span. Since there were no parameters changed, and the tests were only run a couple of minutes apart, it was expected that there would be very little difference between consecutive trial runs. Note that all of the peak frequencies, especially at the lower modes, align almost perfectly. The accelerometer data and ERA were used to produce Table 5.1: the means for three trials on beam S02-1 at 0psi and 125mv excitation level.

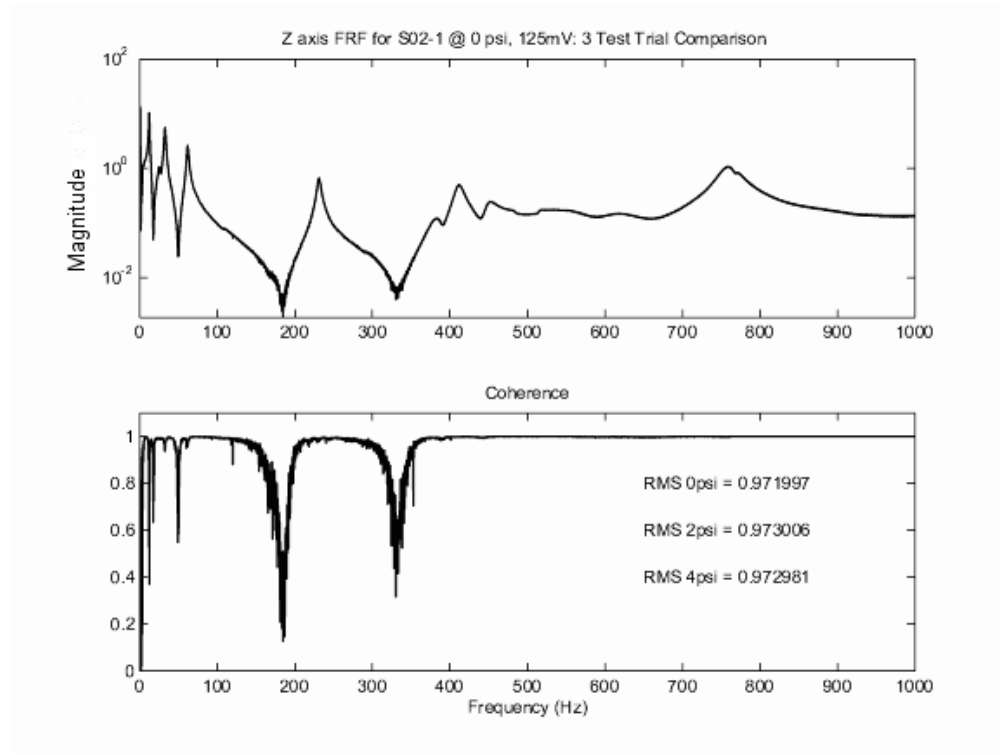


Figure 5.1 Trial Comparison for S02-1 @ 0psi, 125mV

Figure 5.2 compares the damping level against the peak frequency for each of the trials. For the three trials, the peak values are almost identical, as was as the damping level. Several modes have much greater damping than the average of about 1.5% damping. It can be seen that the value of zeta for each of the trials is consistent over the entire frequency span.

Figure 5.3 shows the FRF for 0-1000 Hz for three identical trails on beam S02 utilizing the laser vibrometer. Figure 5.4 shows the FRF for a span of 0-300 Hz. There is more noise introduced into the system using the laser; however, the low mode peak frequencies are clearly discernable. In this example, two of the vibrometer trials are very clean signals and are closely correlated, and there is one trial that is extremely noisy. This could be from the laser being slightly out of focus, the angle from the laser to the scan point changing slightly from a variation in the pneumatically damped table, or a lose BNC connector. The main factor for the noise

Table 5.1 Mean Values for 3 Trials Comparison for S02-1 @0 psi, 125mV

Mode #	Omega Mean	Omega STDEV	Zeta Mean	Zeta STDEV
1	12.19	0.03	2.98	0.53
2	25.71	0.42	6.76	1.03
3	32.39	0.09	2.41	0.16
4	61.65	0.05	1.81	0.01
5	231.10	0.05	0.97	0.02
6	383.45	0.13	1.88	0.01
7	411.40	0.25	1.51	0.06
8	447.78	1.33	1.86	0.25
9	520.64	7.61	8.20	8.80
10	558.92	27.26	4.83	2.43
11	633.79	23.14	9.65	4.32
12	759.01	1.05	1.53	0.27
13	769.13	1.08	0.95	0.75
14	994.14	10.83	2.12	2.39

is that only 15 averages were taken at a single scan point. The vibrometer scans at a very high rate; therefore, more averages could have to be used to get a smoother curve.

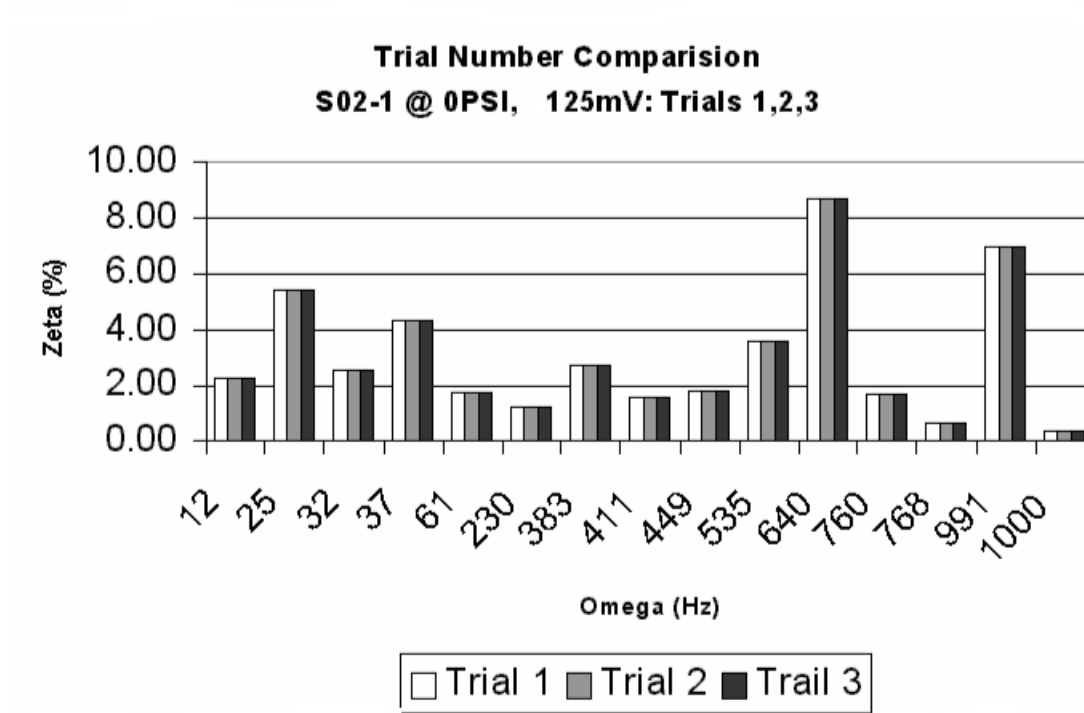


Figure 5.2 Trial Number Comparison: Zeta vs Omega for S02-1

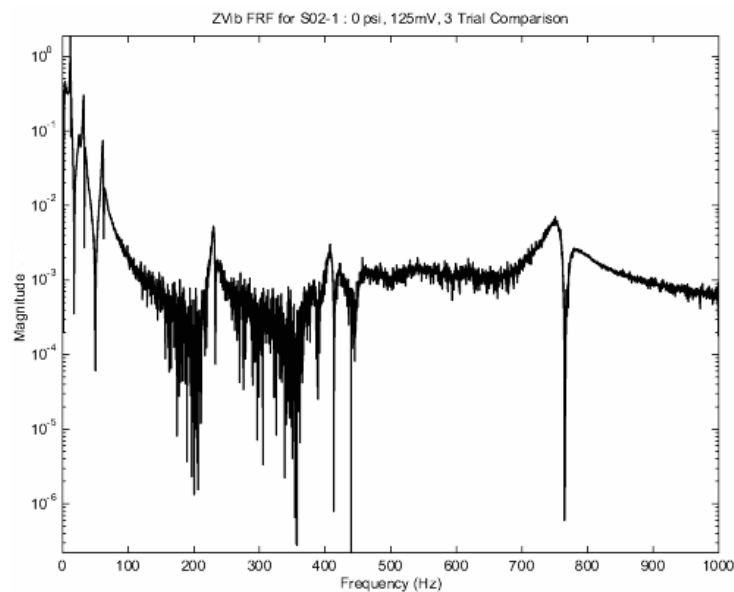


Figure 5.3 Z axis (Vibrometer) FRF Comparison of 3 Trials, S02-1 0psi, 125mV, 1000Hz

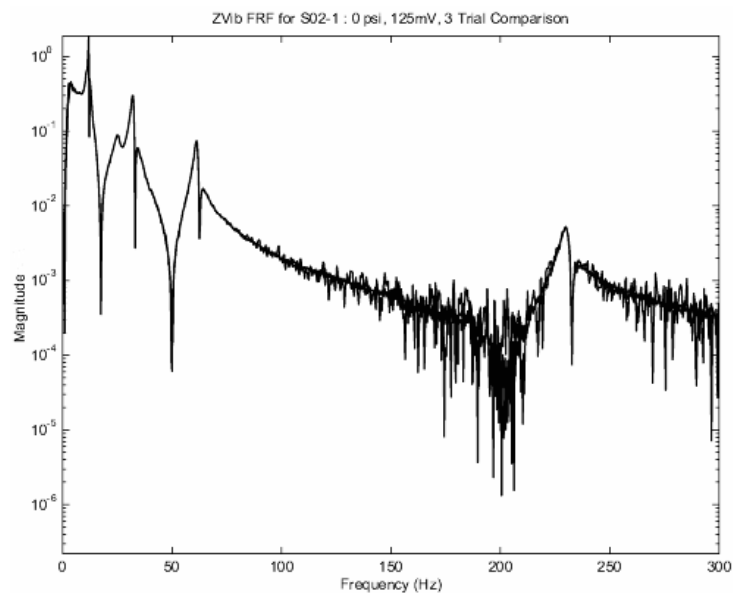


Figure 5.4 Z axis(Vibrometer) FRF Comparison of 3 Trials, S02-1 0psi, 125mV, 300 Hz

A three trial comparison for the X,Y axis was done for the vibrometer. The X axis FRFs match well, while the Y axis lines showed more noise and less coupling. The beam bending was in the z direction, consequently, the vertical x axis is closely coupled with the bending. The “cross” axis or Y, had little displacement or bending in the z direction. Both of these plots showed lots of noise and were difficult to show; consequently, their graphs are omitted.

The basic modal properties of the beams have been shown, along with the plots that are used. It was noted that there was very little change in the data between test runs; therefore, a single test run will be used for the remainder of the analysis(except where noted). However, at least two test runs were accomplished for each test. This greatly reduced the amount of processing time due to the large amount of data collected.

5.1.2 Excitation Comparison. The next step in the methodology was to conduct tests to determine how the variation in excitation, pressure and orientation effects the results. Three levels were chosen for the excitation level: 125, 300, and 500mV. A signal below 100mV or above 550mV produced too much noise and accurate readings were not able to be made. Consequently, the span was divided approximately equally to arrive at the three levels.

Figure 5.5 shows beam S02-1 at 0 psi for the three levels of excitation at a frequency span of 1000Hz. Figure 5.6 is a zoomed in graph for 0 to 100 Hz. The FRF correlation, especially at the peak frequencies is very good. Table 5.2 lists the means calculated for the three levels of excitation: 125, 300, and 500mV. It can be seen that the calculated values do not directly correspond and were aligned in the table for comparison. This calculated data will be used in comparison graphs.

Figure 5.7 compares the damping versus the peak frequency for the three excitation levels. There are modes that clearly have significant more damping. The beams are damped about 1.5%, while the modes near 25, 37, 535, 640, and 991 Hz,

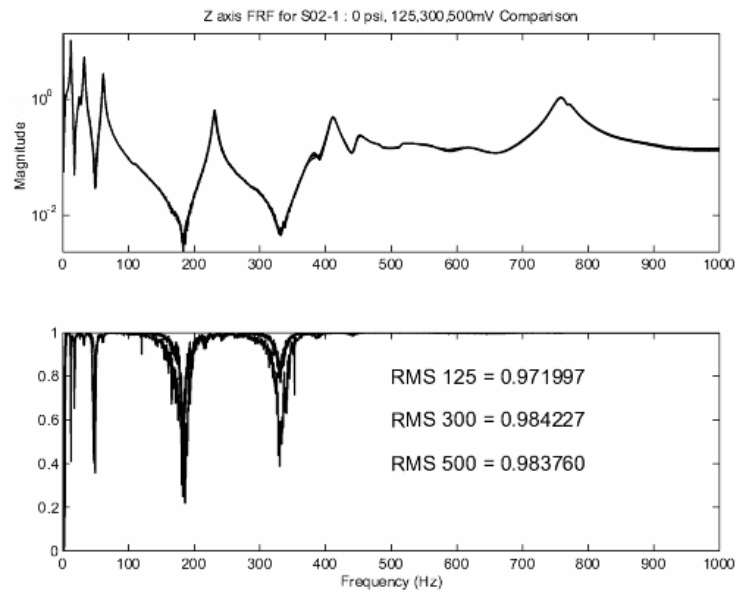


Figure 5.5 Excitation Comparison (**0-1000 Hz**) for S02-1 @ 0psi

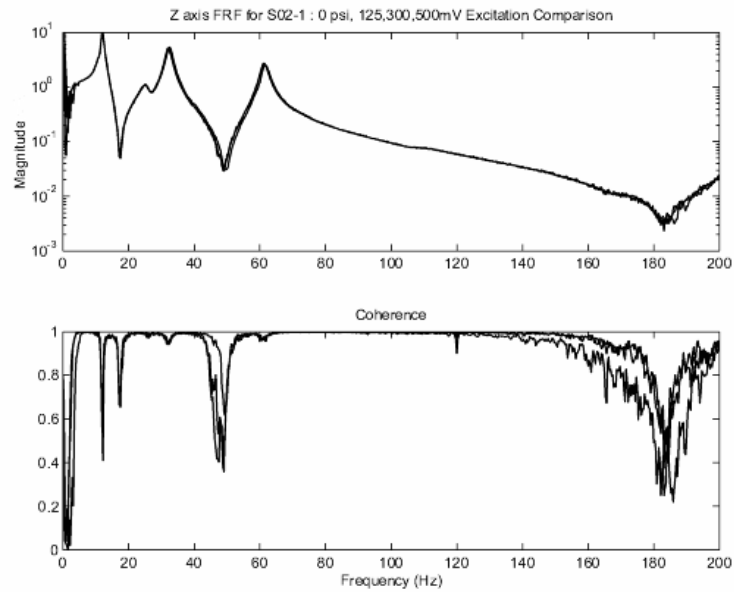


Figure 5.6 Excitation Comparison (**0-200 Hz**) for S02-1 @ 0psi

Table 5.2 Mean Values for Excitation Comparison

Omega Mean			STDEV	Zeta Mean			STDEV
125 mV	300 mV	500 mV		125 mV	300 mV	500 mV	
12.19	12.16	12.17	0.01	2.98	2.68	2.85	0.15
25.71	25.71	25.97	0.15	6.76	7.15	7.60	0.42
32.39	32.06	31.99	0.21	2.41	2.27	2.19	0.11
61.65	61.20	61.18	0.26	1.81	1.71	1.69	0.06
231.10	230.17	230.12	0.55	0.97	1.20	1.21	0.13
.	382.51	381.69	47.15	.	2.34	2.59	56.31
411.40	410.98	410.93	0.26	1.51	1.57	1.56	0.03
447.78	449.25	449.28	0.86	1.86	1.79	1.75	0.06
520.64	533.54	535.61	8.11	8.20	3.31	3.43	2.79
633.79	638.53	632.19	3.29	9.65	8.76	8.95	0.47
759.01	759.65	759.53	0.34	1.53	1.67	1.67	0.08
769.13	768.53	768.68	0.31	0.95	0.60	0.60	0.20
.	981.31	985.93	3.27	.	7.84	8.66	0.58
994.14	999.51	999.53	3.11	2.12	0.49	0.53	0.93

are at least twice as damped. Around 640 Hz, there is approximately 9% damping, or about 6 times the average damping.

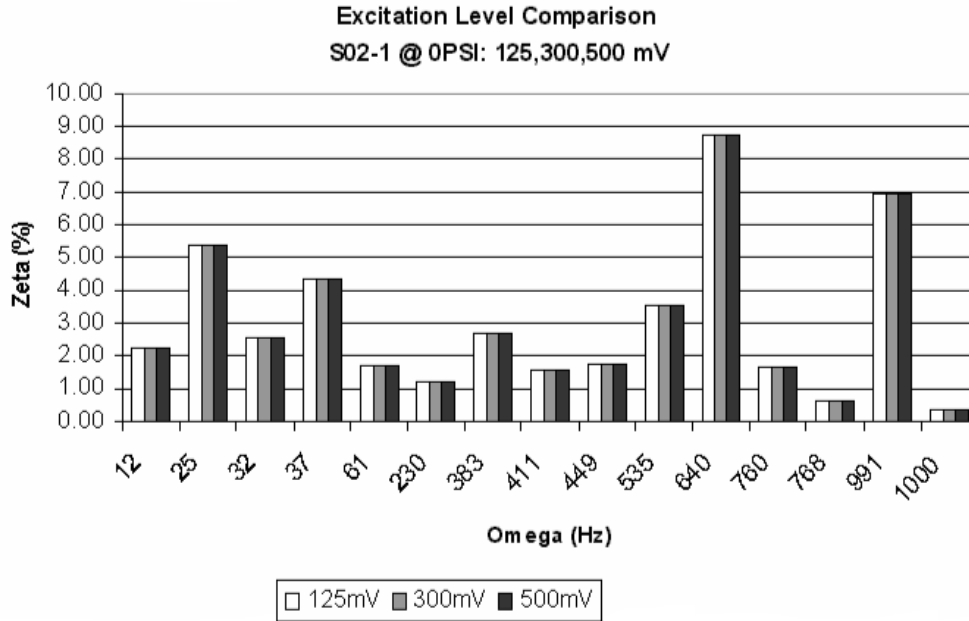


Figure 5.7 Excitation Comparison: Zeta vs Omega for S02-1

5.1.3 Orientation Comparison. The next parameter to be tested was the orientation of the beam. The beams were rotated through positions 1-4 to determine if there was an effect due to the seam or non-symmetry.

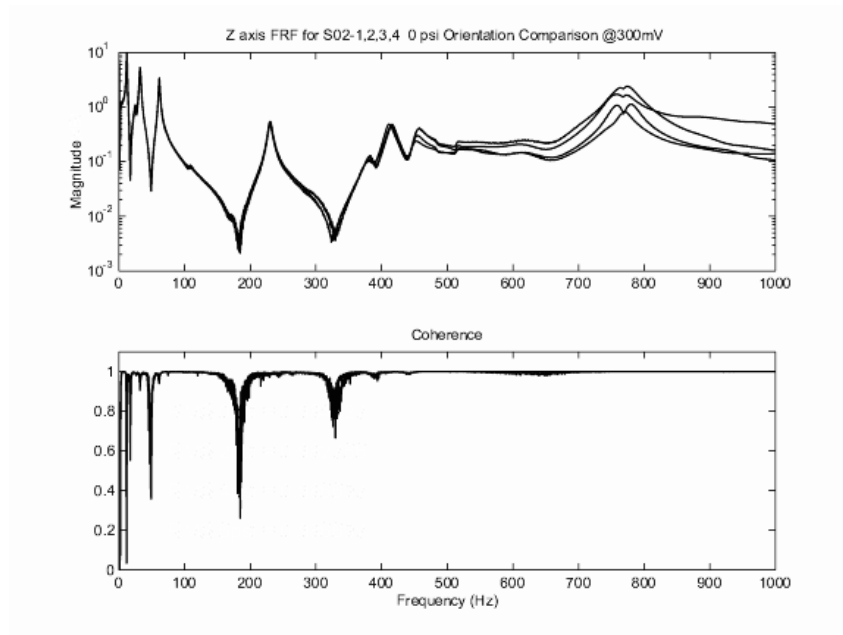


Figure 5.8 Orientation Comparison (0-1000 Hz for S02 @ 0psi,300mV)

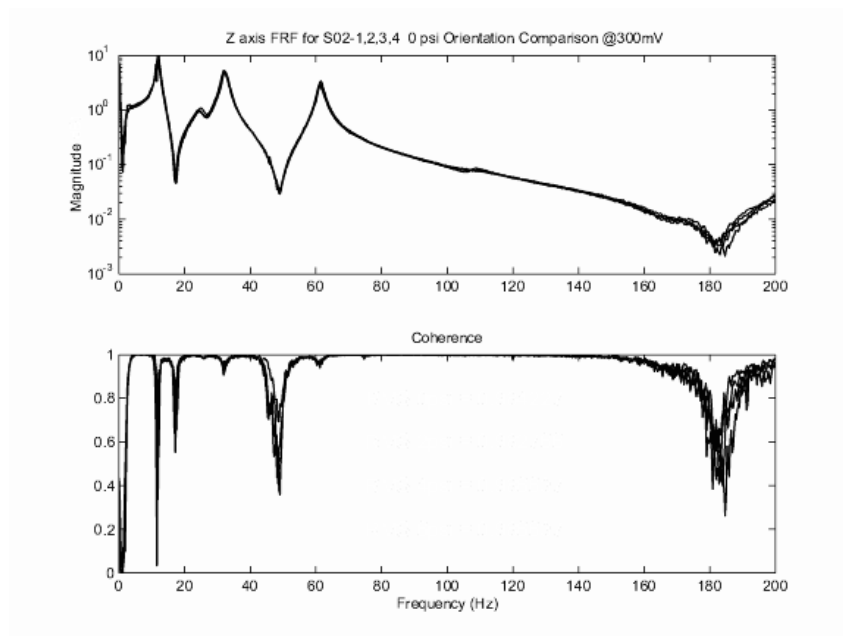


Figure 5.9 Orientation Comparison (0-200 Hz for S02 @ 0psi,300mV)

Table 5.3 Mean Values for Orientation Comparison for S02 @ 0psi,300mV

Means for S01-1		Means for S01-2		Means for S01-3		Means for S01-4	
Omega(Hz)	Zeta(%)	Omega(Hz)	Zeta(%)	Omega(Hz)	Zeta(%)	Omega(Hz)	Zeta(%)
12.15	2.41	11.97	0.35	12.13	1.76	11.99	2.78
25.39	6.92	24.48	1.42	24.88	6.49	24.91	6.11
32.13	2.34	31.98	2.73	32.44	2.33	32.12	2.43
61.23	1.73	61.39	1.77	61.57	1.56	61.45	1.36
230.22	1.2	230.73	1.34	230.21	1.27	229.84	1.18
Means for S01- 1 & 3				Means for S01- 2 & 4			
Omega Mean	Omega STDEV	Zeta Mean	Zeta STDEV	Omega Mean	Omega STDEV	Zeta Mean	Zeta STDEV
12.14	0.01	2.09	0.46	11.98	0.01	1.57	1.72
25.14	0.36	6.71	0.30	24.70	0.30	3.77	3.32
32.29	0.22	2.34	0.01	32.05	0.10	2.58	0.21
61.40	0.24	1.65	0.12	61.42	0.04	1.57	0.29
230.22	0.01	1.24	0.05	230.29	0.63	1.26	0.11
Mean for all 4 orientations							
Omega Mean	Omega STDEV	Zeta Mean	Zeta STDEV				
12.03	0.09	1.63	1.22				
24.76	0.24	4.67	2.82				
32.18	0.24	2.50	0.21				
61.47	0.09	1.56	0.21				
230.26	0.45	1.26	0.08				

Table 5.3 is a partial list of the means calculated for the means of first few modes of interest. Note that because the beams are symmetric that we expect 1 and 3 to correspond and 2 and 4 to correspond. The seam is along orientation 1 which is probably the cause of 1 and 3 to have slightly higher values due to the small amount of increased stiffness. The beams also were not perfectly circular. Figure 5.10 shows that the peak frequencies do not change by orientation position.

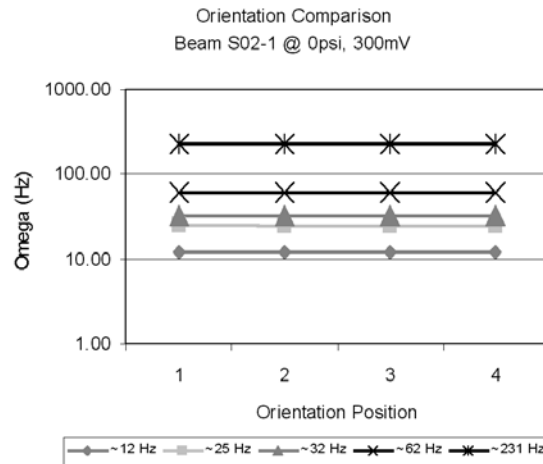


Figure 5.10 Omega vs Position Orientation Comparison of the 1st 8 modes for S02 @ 0psi,300mV)

Figures 5.11 and 5.12 compare the damping versus the peak frequency. It can be seen that the orientation does effect the level of damping, due to the irregularities in the beam construction.

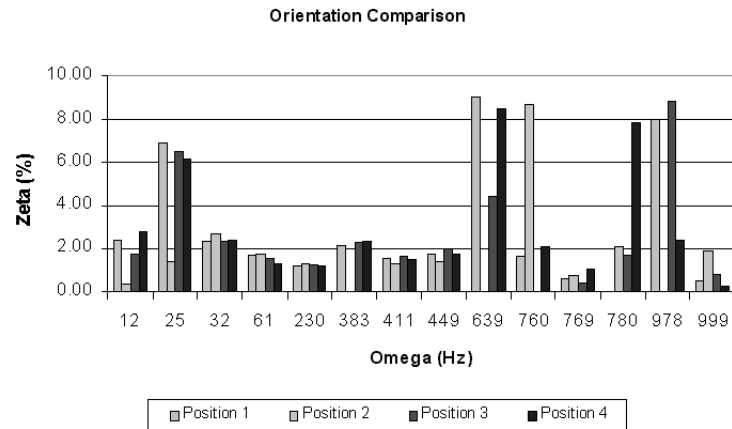


Figure 5.11 Zeta vs. Omega Orientation Comparison (0-1000 Hz for S02 @ 0psi,300mV)

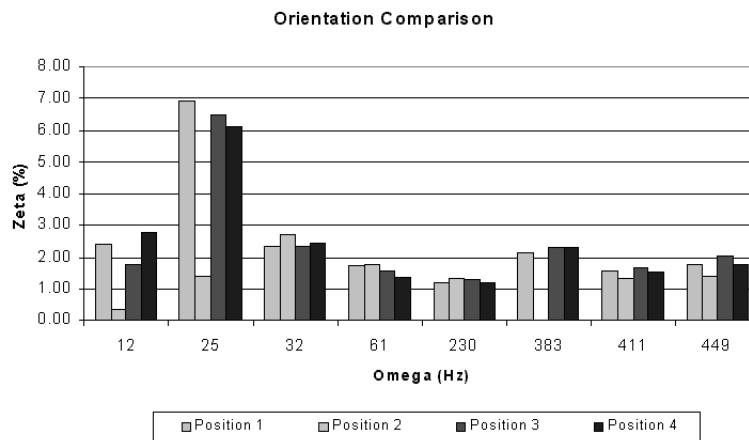


Figure 5.12 Zeta vs Omega Orientation Comparison of the 1st 8 modes for S02 @ 0psi,300mV)

5.2 Pressure Comparison

Pressure comparisons were made for 0,2,4,and 6 psi (gage pressure). Zero was selected as the reference point where the pressure in the beam equals the ambient conditions. The beam will be inflated in space at 4 psi, so it had to be tested on the ground. Reference points of 2 and 6 were also selected for give 4 data points, yielding better data to draw results from than with just 2 data points. Figure 5.13 and Figure 5.14 show the variations in pressure at 1000 and 200 Hz. It can be seen that the change in pressure does not effect the transfer functions below 300 Hz. The higher frequencies are effected slightly. Further testing will determine if assuming that this remains constant for the test conditions and in the vacuum of space. If it does, then the pressure level would not effect the bending modes, which is an unexpected result.

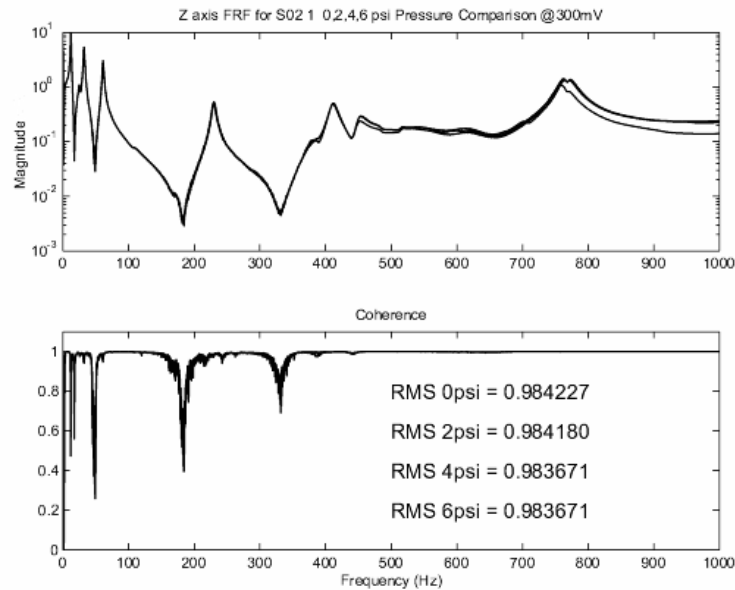


Figure 5.13 Pressure Comparison (0-1000 Hz for S02-1 @ 300mV)

For the sake of brevity, Table 5.4 lists only the means of the means for the first few modes of interest. The entire set of data was used for the comparison graphs at the end of this section.

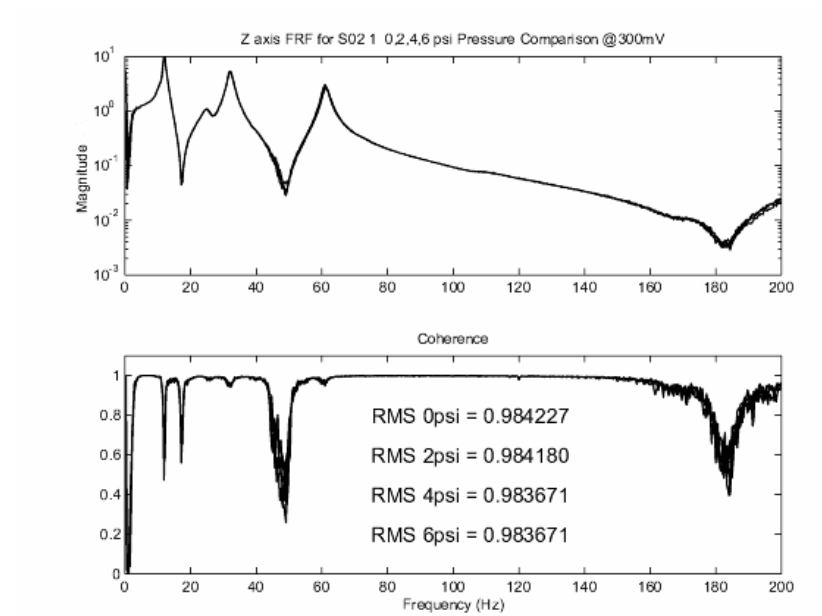


Figure 5.14 Pressure Comparison (0-200 Hz for S02-1 @ 300mV)

Table 5.4 Mean Values for Pressure Comparison

Omega Mean	Omega STDEV	Zeta Mean	Zeta STDEV
12.16	0.01	2.56	0.01
25.64	0.02	7.24	0.12
32.02	0.01	2.23	0.04
60.92	0.03	1.60	0.01
229.31	0.04	1.31	0.01

The values of zeta are graphed against the peak frequencies in Figure 5.15, and omega versus the mode number are shown in Figure 5.16. The values are plotted according to the mode number from PSV. It can be seen that since all of the calculated points do not exactly agree, except for the first couple of modes. A more meaningful representation will have the the mode numbers aligned with approximately the same value of omega. The remainder of the graphs have been aligned.

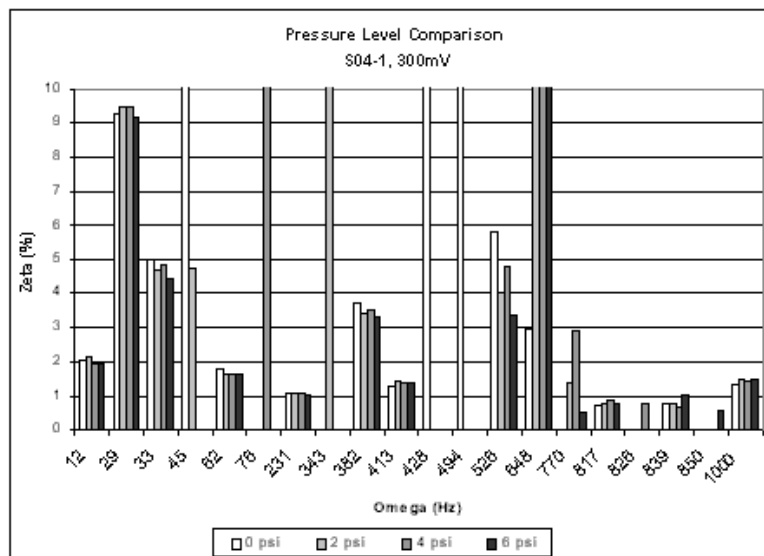


Figure 5.15 Pressure Comparison: Zeta vs Omega for S04-1 for Raw Data

Figure 5.17 shows the peak frequency versus the mode number for 0 and 4 psi. It is expected that the 4 psi test would result in a higher peak value than 0 psi, and for the most part it does. The first couple of modes are closely matched, and the higher mode numbers vary. The test with S03 has the 0 psi peaks higher than the 4 psi peaks, and is probably directly related to the unexpected transfer functions that were discovered earlier. There was obviously an error in the vibration testing or setup for S03. The results of mounting the PZT will be shown later, except that S03 with the PZTs mounted is shown here for a comparison. Note that the modes are more closely aligned, only above the 7th mode do the two curves diverge. This

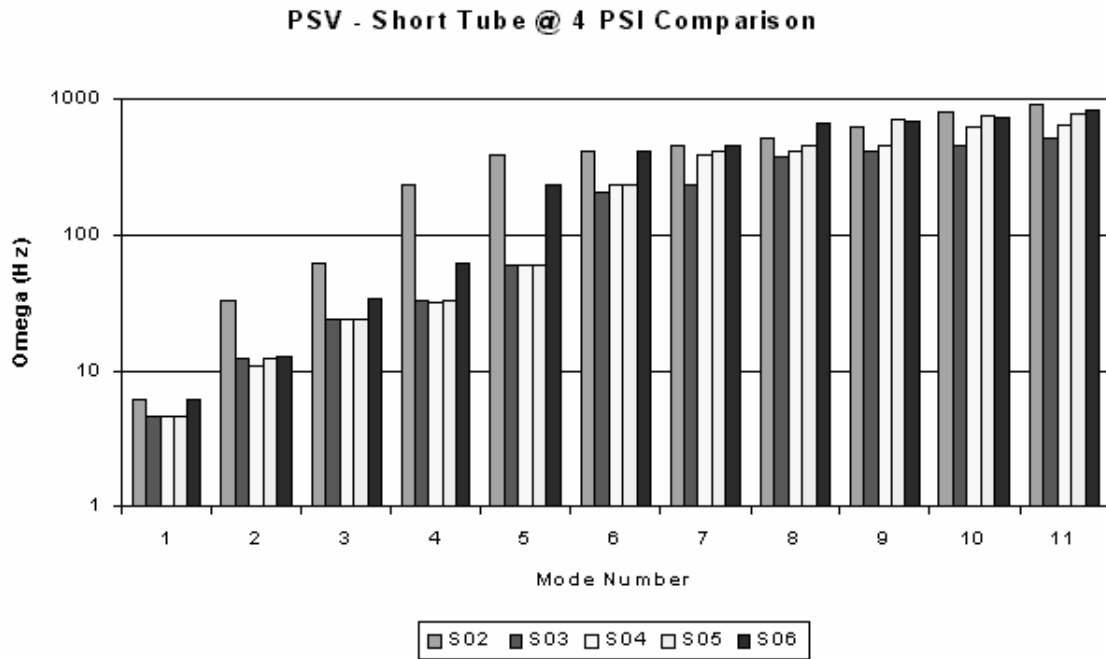
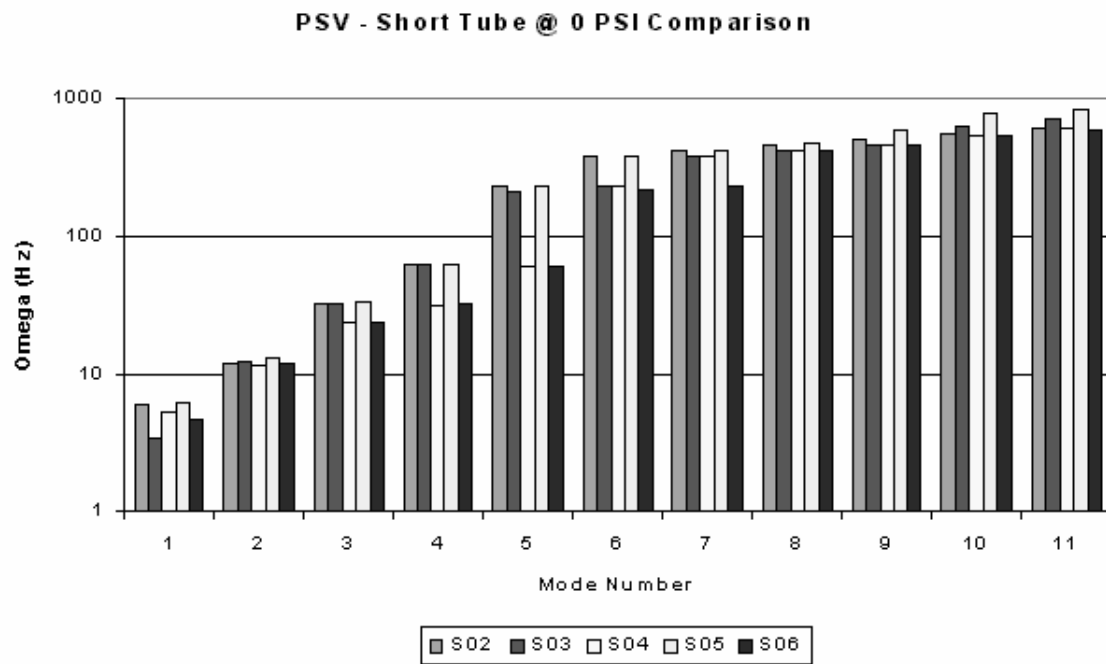


Figure 5.16 Omega vs Mode for Pressure Comparison from PSV

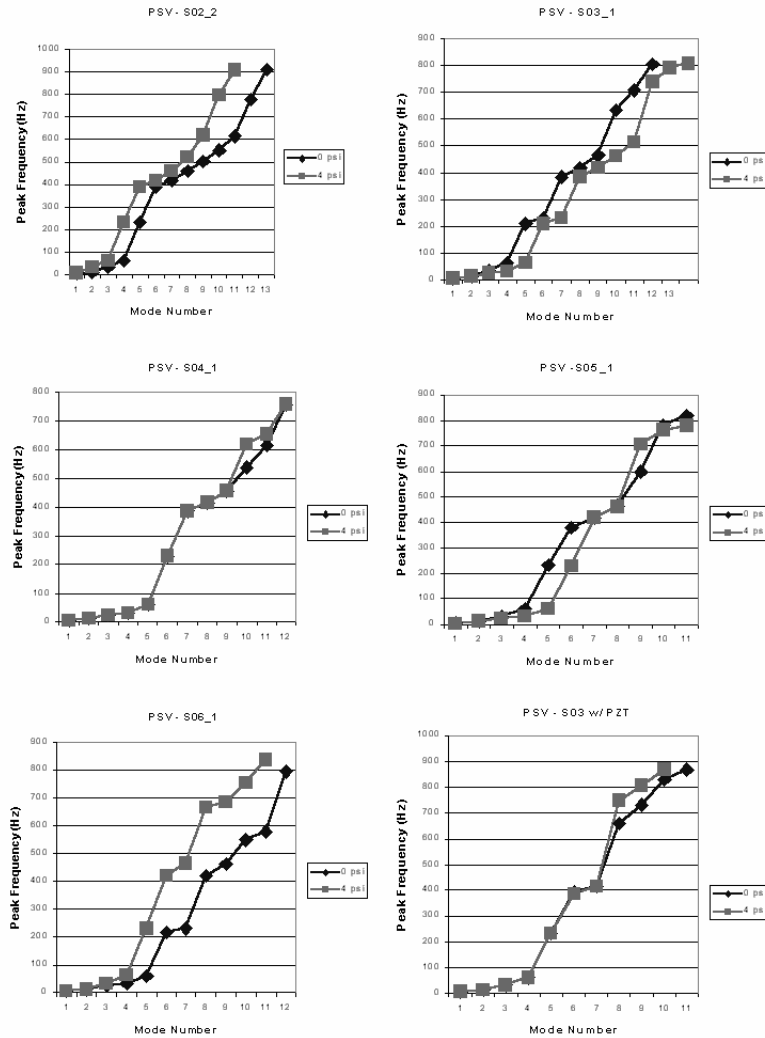


Figure 5.17 Individual Short Beam Pressure Comparisons from PSV

is most likely due to the increased stiffness and mass, which negates the small effect of the pressure change.

Figure 5.18 shows the FRF for S04 for various pressures. Figure 5.19 compares zeta versus omega for S04 for a range of pressures. In general, the different pressure levels do not change the values of zeta significantly. The 25, 520, and 647 Hz modes show some significant differences in values of zeta. The higher frequency values have been shown to not correlate as closely as the lower frequencies; however, the mode at 25 Hz shows a drop from 6% to 4% damping from 0 to 6 psi. The trial and excitation

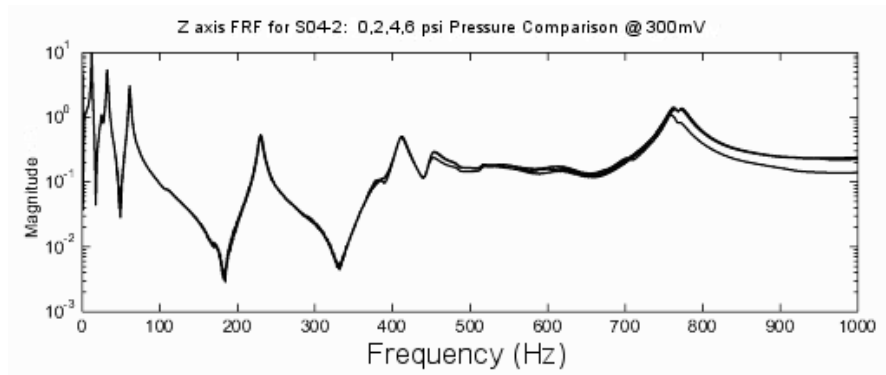


Figure 5.18 FRF for Pressure Comparison

comparisons did NOT show this drop-off. The pressure in the beams was assumed to stay constant throughout the tests and were monitored. This may be due to the fact that the higher pressure creates a stiffer beam which would relate to a drop in damping. A FRF is shown above the figure for comparisons. It can be seen that the peak values of omega do not directly correspond with the peak values of zeta.

The natural frequencies are compared to the pressure at several frequencies in Figure 5.20 for beam S04. The upper left graph demonstrates for four lower frequencies how consistent the frequencies are as the pressure level changes, they are very close to a straight line. The bottom left graph, plotted with a logarithmic y scale, is a representation showing the increase of natural frequency. The damping levels are surprising. They are not as consistent over the different pressure ranges and the damping changes for the different pressure levels. The conclusion that can be reached that the increasing pressure level does not effect the natural frequency; however, the damping ratio will in general decrease as the beam becomes stiffer. This is as expected for cantilever beams.

A comparison of the pressure changes for the long beams was also accomplished. The FRF responses at 0 and 4 psi are shown in Figure 5.21 for the two long beams. The curves are all closely correlated. The upper left-hand plot shows a bending

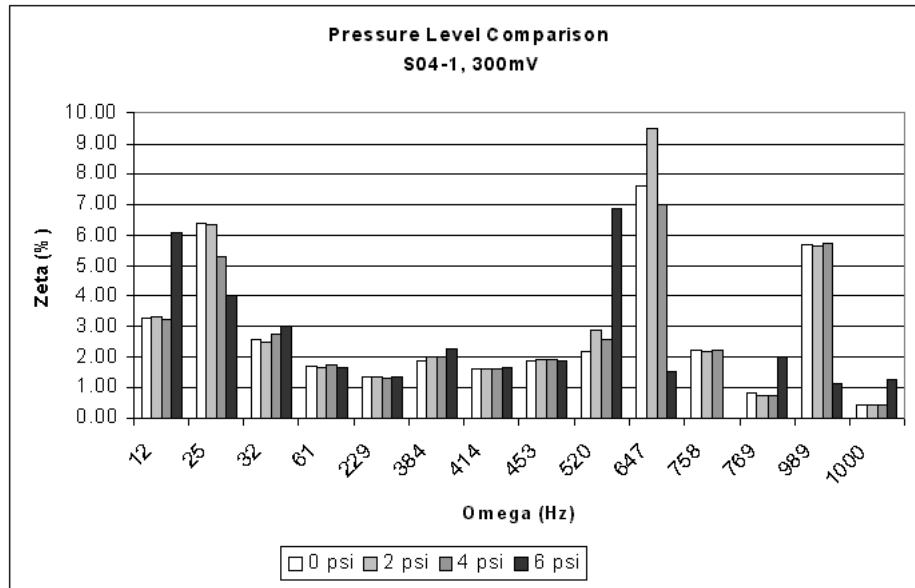


Figure 5.19 Zeta vs Omega for Pressure Comparison: Zeta vs Omega for S02-1

mode around 115 Hz and the damped peaks at the higher frequencies. Figure 5.22 shows a comparison from PSV of 0 and 4 psi.

Figures 5.23 and 5.24 show that the natural frequencies and damping are not dependent on pressure.

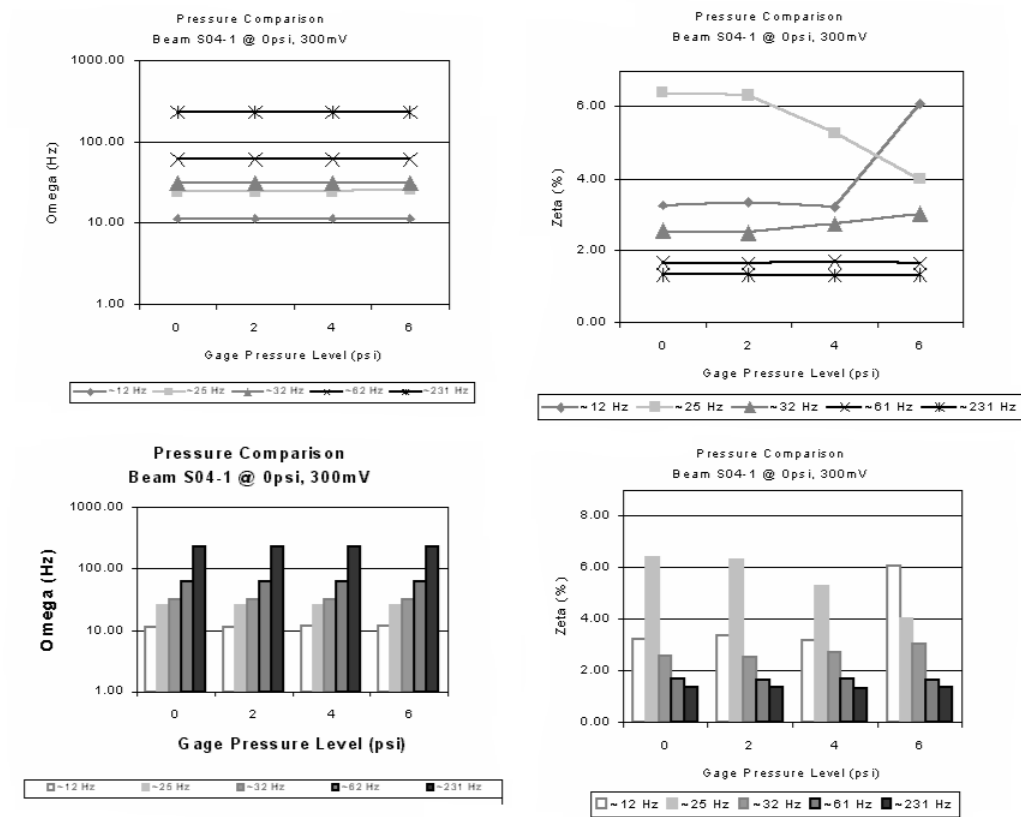


Figure 5.20 Pressure Comparison: Zeta vs Omega for S04-1 for Aligned Data

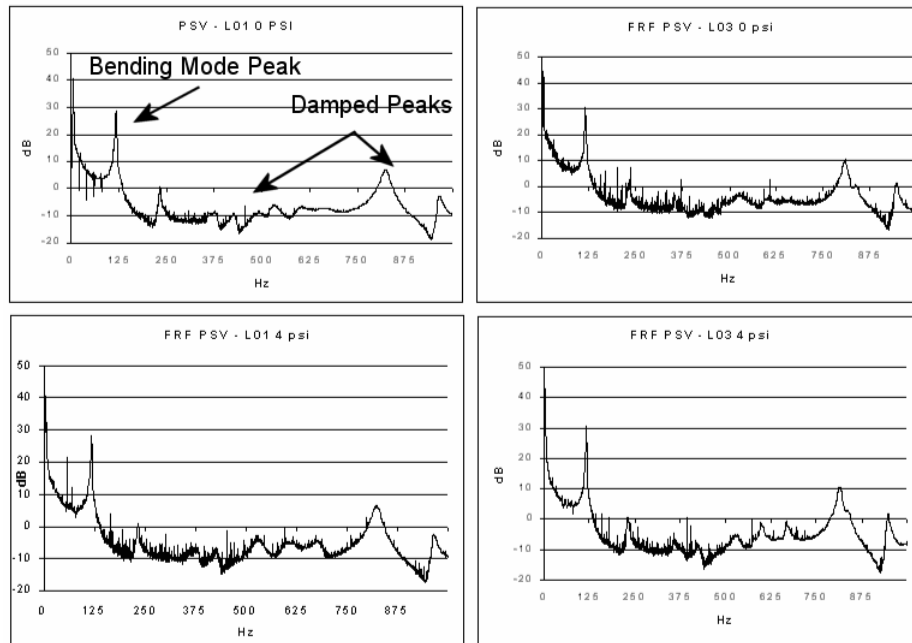


Figure 5.21 FRF PSV - Long Beams

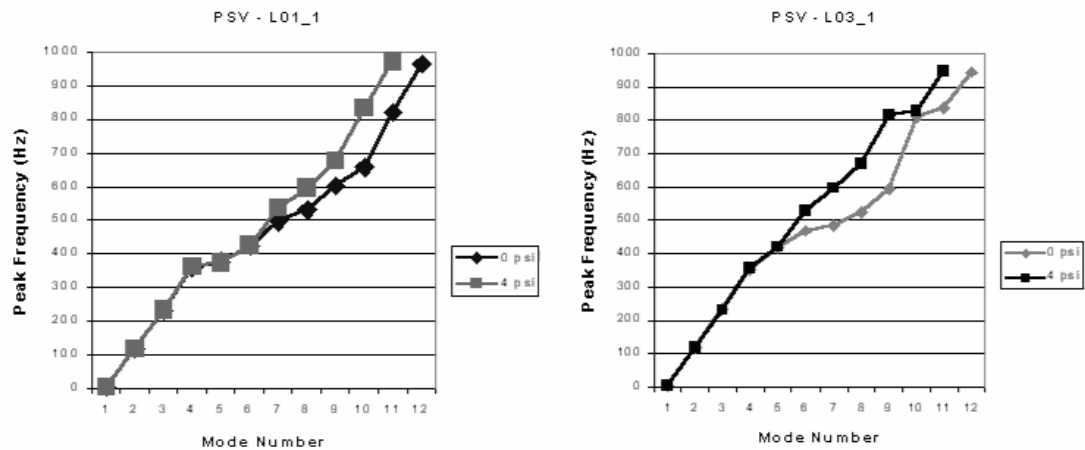


Figure 5.22 PSV Long Beam Comparison

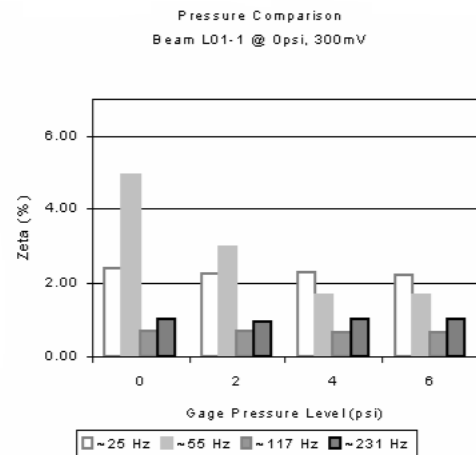
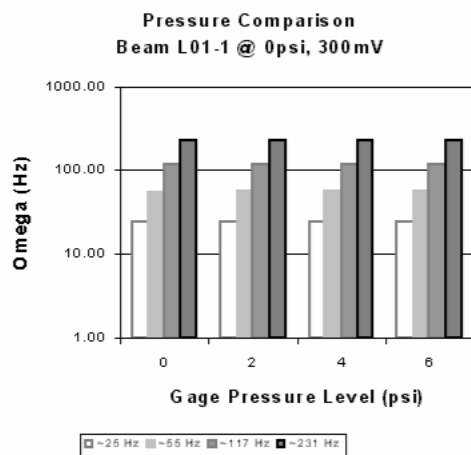
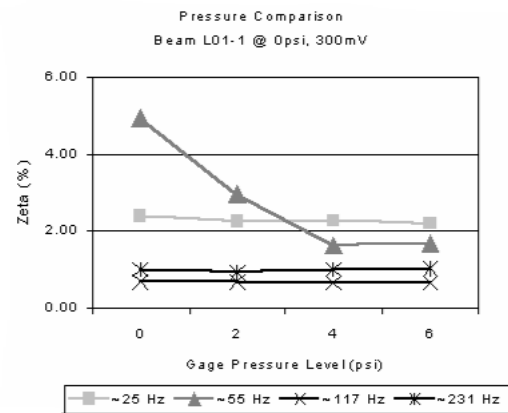
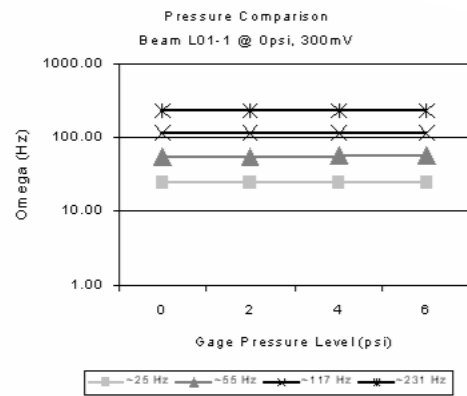


Figure 5.23 Pressure comparison L01

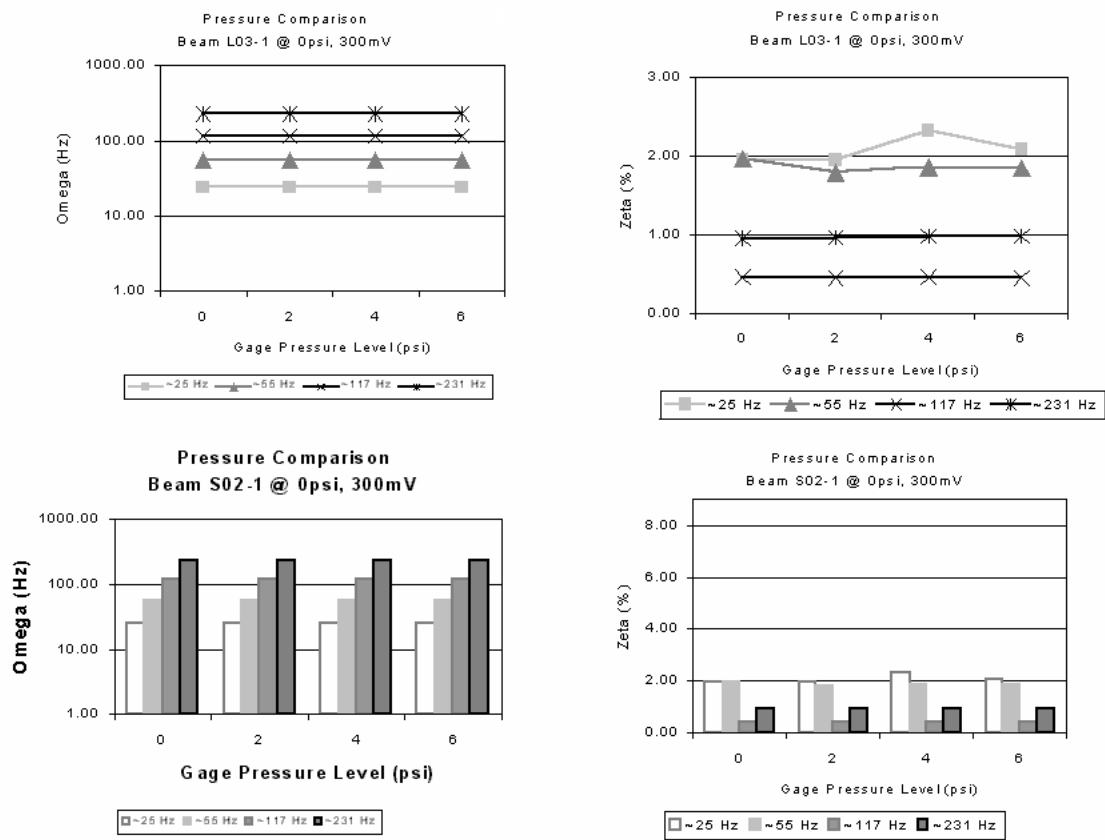


Figure 5.24 Pressure comparison L03

5.3 Temperature Comparison

The temperature effected the properties of the beams, as expected. The increased temperature softens the beam. This shifts the natural frequencies slightly down and increases the damping as shown in the following figures. Figure 5.25 shows the transition region in the range of 45 to 65 degrees for the 50 Hz mode. The higher frequency modes were more linear and were not as greatly effected, as shown in the curve for the 62 Hz mode.

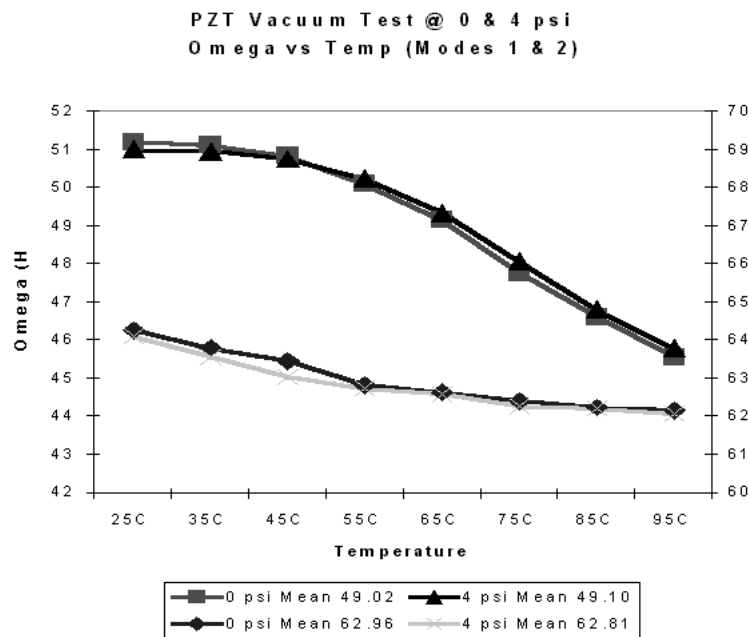


Figure 5.25 Temperature Comparisons for S03

Figures 5.26 and 5.27 show the comparisons of omega and zeta temperature comparisons for the first few modes. The frequencies did not change significantly, however, it can be seen that the damping did vary.

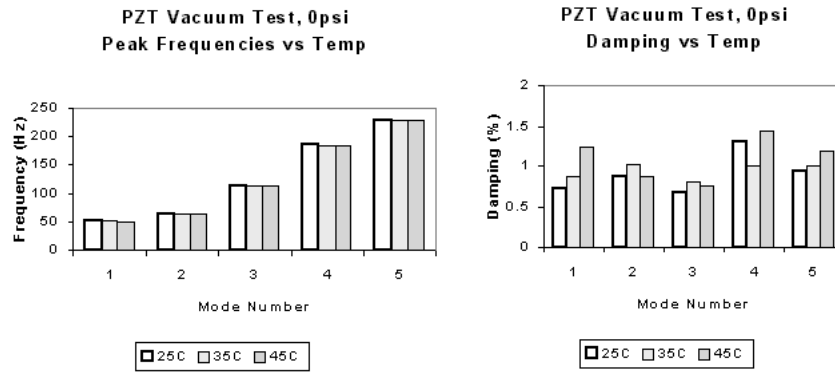


Figure 5.26 Omega and Zeta vs Temperature Comparisons for S03

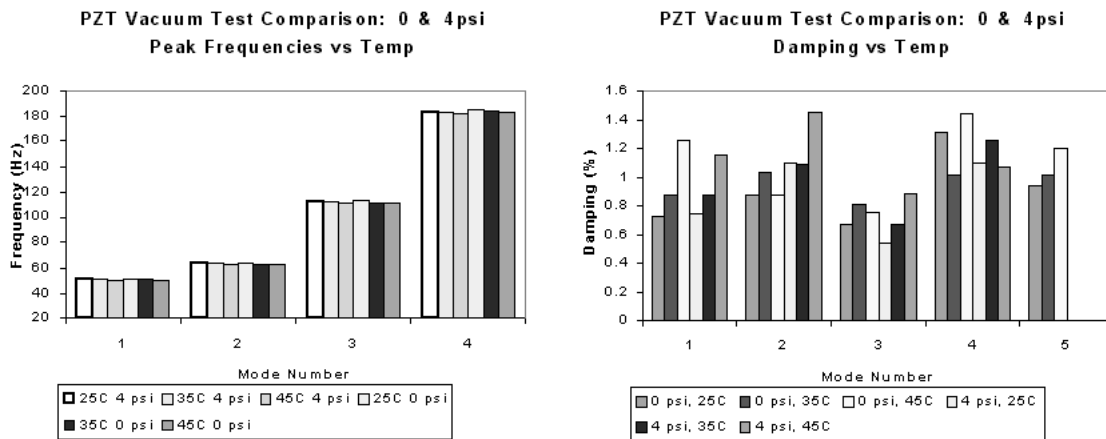


Figure 5.27 Omega and Zeta Temperature Comparisons for 0 & 4 psi.

5.4 Vacuum Comparison

Figure 5.28 is a comparison of ambient to vacuum conditions at 25C. This figure shows that in a vacuum, the damping is less. The figure following shows zeta vs omega at a slightly higher temperature. This figure also shows that the damping is reduced in the vacuum.

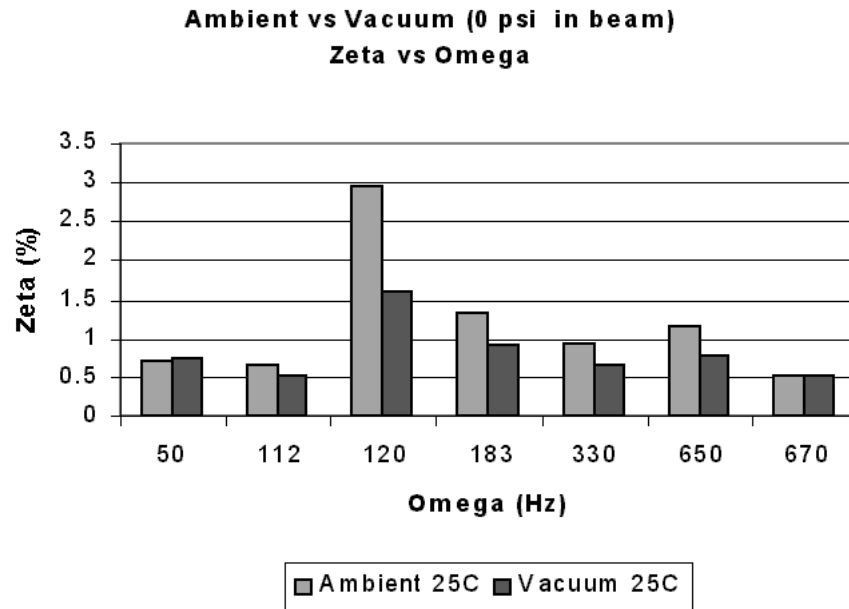


Figure 5.28 Ambient vs. Vacuum Comparisons for S03 @ 25C

5.5 Summary

In summary, the repeatability between trials was very good. The data collected was very consistent. The excitation level did not effect the FRFs however, there was an optimum range to collect data to minimize noise. The orientation position did not effect the natural frequencies; however, there was variation in the damping level. Changing the internal pressure of the beams caused a slight increase in omega values and a slight decrease in damping values due to the increased stiffness of the beams. However, for the for the first few modes, the pressure did not effect omega or zeta

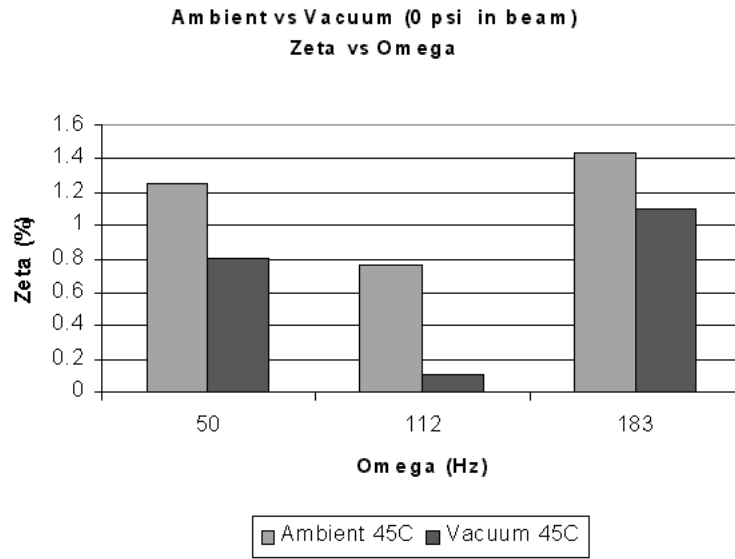


Figure 5.29 Ambient vs. Vacuum Comparisons for S03 @ 45C

noticeably. The temperature showed a shift in both natural frequency and damping levels due to the softening of the beam. As expected, testing in the vacuum reduced the damping and increased the natural frequencies. The last chapter summarizes the research and presents suggestions for future work.

VI. Summary and Future Work

6.1 Summary

The shaker was used for the initial testing due to its ease of use and familiarity with the equipment. The modes imparted by the shaker proved significant. The shaker was used to characterize the parameters effecting the modal properties of the beams. It was determined that the pressure level had almost no change on the modal properties for the lower frequencies. The heating of the beams only had slight effects, but the beam did change as expected.

The bending modes were identified. The first bending mode was identified at 32 Hz on the shaker, and 51 Hz in the vacuum chamber. The second and third modes were fairly consistent around 62 and 231 Hz. The testing showed that a simplified beam bending theory provides a reasonable estimate for the first couple of modes. There were different natural frequencies found for the different test configurations, which were also different from the analytic results. It was discovered that the beams have torsional modes and other modes that requires a more advanced study. In order to model a more complicated system, beam theory would probably not produce accurate results.

6.2 Future Work

The future work that will be accomplished on the flight test should take into account the following factors. All of the materials used will have to meet the temperature and vacuum requirements. All of the wiring and plumbing will have to take the temperature extremes, while not out-gassing. The kapton heaters should be ordered with the aluminum adhesive backing already installed. Several methods were used during this experiment, and having the the peel-off backing would work the best. The heaters can also be painted flat black for greater emissivity; however, this was not required for the ground testing. A digital controller should be used

to control the temperature in the vacuum chamber. One was not available for the ground testing; however, one has been purchased and can now be used.

A significant hurdle to overcome is the PZTs. All of the future testing should utilize the PZTs. Additionally, the PZTs have a higher operating frequency range than the shaker that is limited to 200 Hz. The beams should be manufactured with the PZT built into it. The PZT will also have to be small enough to allow the beam to be folded. Tests will have to be accomplished to determine if these smaller PZTs will be able to excite the beams so that data can be collected. In a 0-g environment, only small excitation levels will be required and this needs to be determined to ensure that the forces applied are not too great. A “cleaner” method needs to be found for attaching the PZT. The EZ-mount clip seemed to work well in the vacuum chamber and can probably be used for future testing. It allows quick and easy removal and attachment of the accelerometer.

The quality of the beam material was not very good. There were many irregularities and two of the beams were not air-tight. The manufacturer is continually improving their methods, so future beams should be of higher quality and the vibration testing will have to be accomplished for each new batch of beams. Beams need to be ordered that are folded in order to determine how the folding effects the results. Additional beams of varying lengths should also be tested to verify the accuracy of an analytic model. As the structures become more complex, the analysis becomes more difficult and it is important that data for the beams is accurate. The mode shapes need to be determined as well. The time constraints of this project did not allow for this to be accomplished. However, it should prove easy to accomplish.

Additional testing must be done in a cold environment. There was not a way to chill the beam to below freezing. A test chamber needs to be found, or the current vacuum chamber could have a chiller system attached to it. The beams will be in the cold vacuum of space and there needs to be some testing prior to the flight test.

Since the temperature is a significant factor in material properties, it is necessary to chill the beams and test them.

The PC 104 computer must be programmed to work as a data acquisition system. It is important to ensure that the computer will be able to collect and store the experimental data. This system should be tested in the next set of experiments. The next step is to build the flight test experiment and run it from beginning to end on the ground. The data collected will have to be analyzed to make sure the experiment does not have to be changed.

AFIT has a great opportunity to make advances in this field. There are many applications for inflatable structures for the Air Force. Satellites are a significant one. However, rigidized structures could be used for emergency shelters, portable antennas, or anything else where a light weight, compact structure is needed. The identification of the bending modes and determining that beam theory can be used is another step in the continuation of the study of inflatable space structures. Additional testing is required before operational deployment of any rigidized inflatable space structure, and this future work should be pursued! Inflatable space structures appear to offer cost savings and should provide increased capability for the Air Force.

Appendix A. RIGEX CAD Drawings [13]

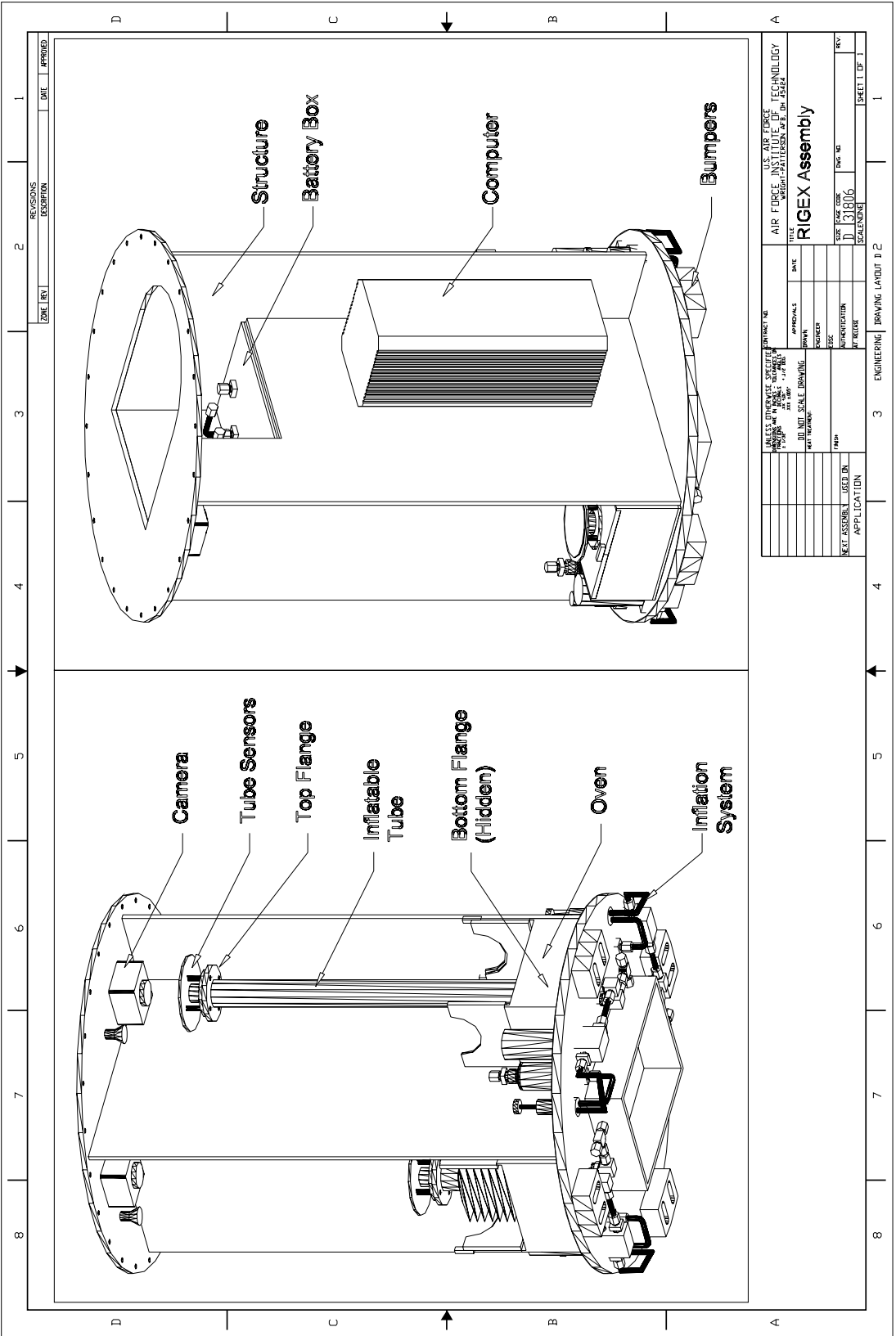
The final configuration of the RIGEX components will be driven by the integration into the complete design. The preliminary design of each part, along with detailed dimensions are included as a starting point.

The first drawing displays the configuration of the preliminary design. The structure is made of one-quarter inch aluminum honeycomb (except for the bottom plate which is one-half inch aluminum) and welded/epoxied at the joints. The top plate of the structure has twenty-four holes for securing to the EMP provided by NASA.

The battery box is constructed of one-eighth inch aluminum plates and welded at the joints. The cover of the battery box is one-quarter inch aluminum and connects to the top of the box with #10-32 socket head cap screws. The final layout of the batteries and the design of the box should be made to maximize the use of the center section of the experiment, to possibly include placement of the computer in the same area as the batteries. Menco heaters will have to be placed with the batteries and heaters to ensure that they do not freeze.

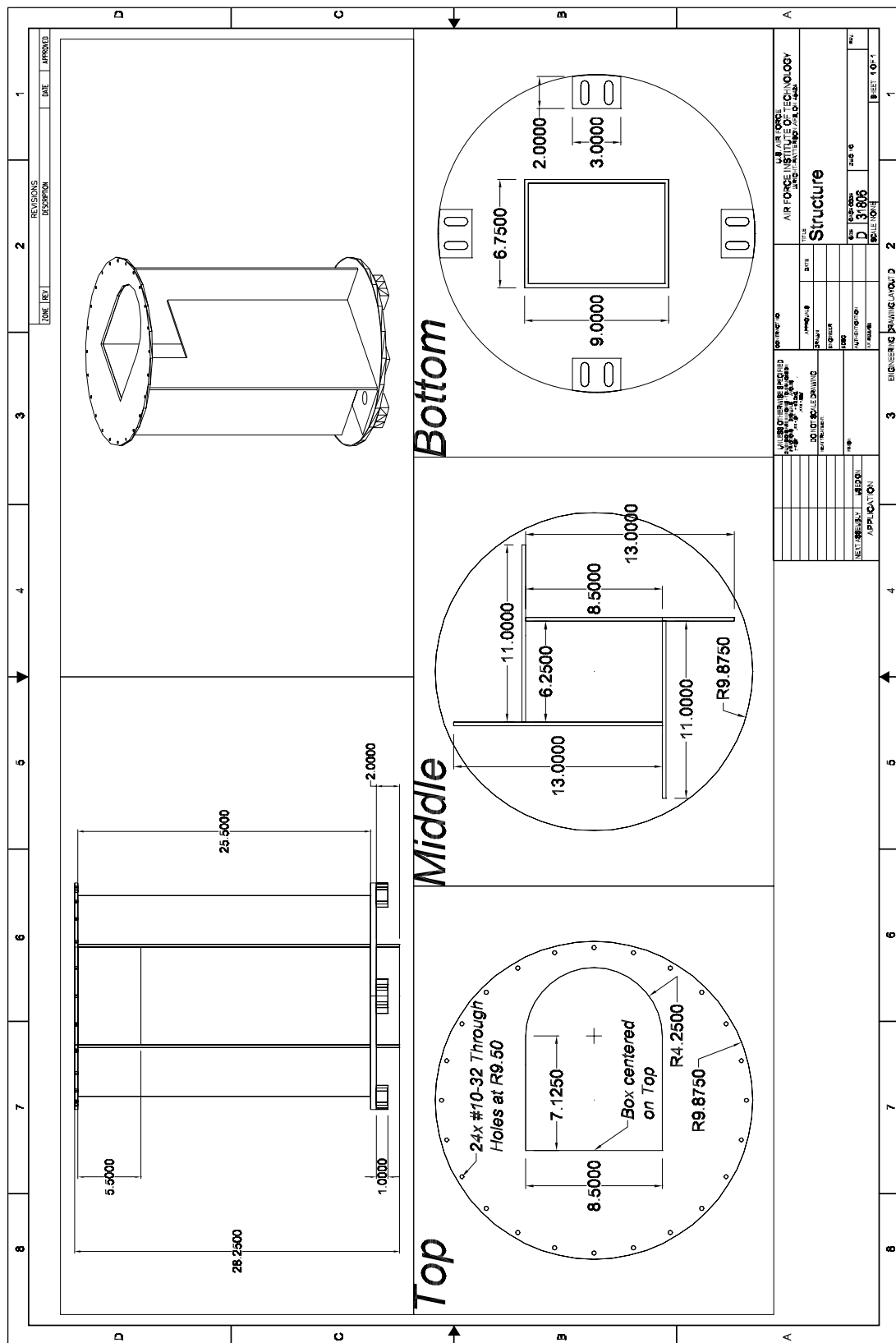
The oven is constructed of one-eighth inch low-conductance thermoplastics to minimize heat transfer out of the oven. The top of the oven is hinged at the ends and grooved to hold the top flange when closed. Commercial pins are used to hold the oven closed until inflation. The pins will have to be controlled by the PC 104 and the hinges should open simultaneously and with constant velocity.

The flanges are also constructed of low-conductance thermoplastics. The inflatable structure is placed over the flange and connected with an adhesive. The top flange is capped to create an airtight seal and allow a cavity for mounting sensors. The bottom flange has a groove for an o-ring and is hollow to allow the inflation system access to the beams. Both flanges have #10-32 threaded holes for mounting the bottom to the structure and the top to the sensors.



REV	DESCRIPTION	DATE	APPROVED
1			

PROJECT NO.		U.S. AIR FORCE		TECHNOLOGY	
TITLE		DATE		REV	
RIGEX Assembly		31806		1	
DRAWN		CHECKED		SCALE	
DO NOT SCALE DRAWING		NEXT TRAINING		SHEET 1 OF 1	
NEXT ASSEMBLY		USED IN		APPLICATION	



Appendix B. Photos of Beam Irregularities

B.1 Beam S02

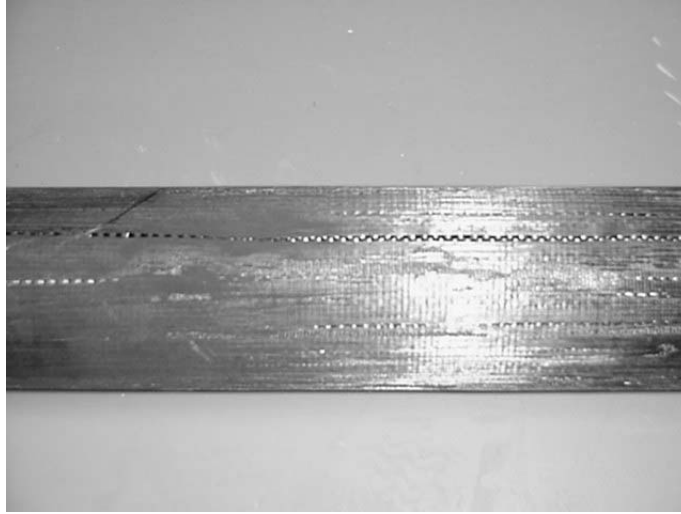


Figure B.1 Beam Surface S02

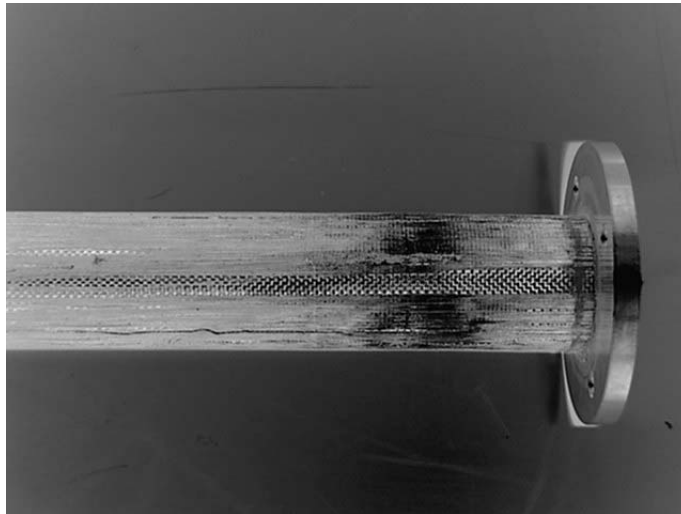


Figure B.2 Beam Surface S02

B.2 Beam S03

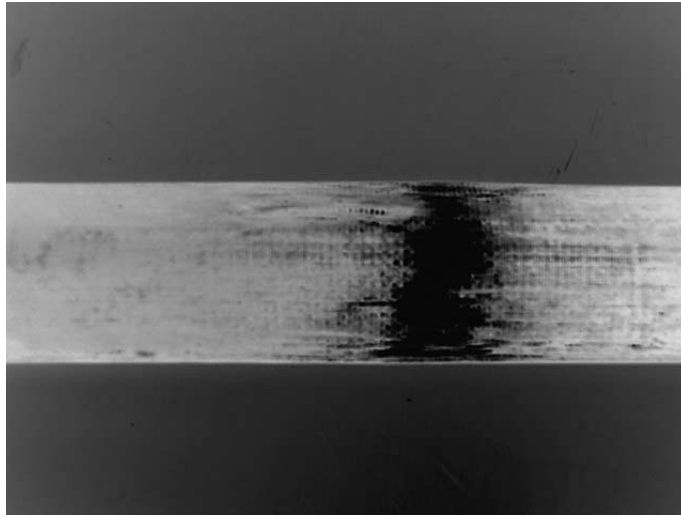


Figure B.3 Beam Surface S03



Figure B.4 Beam Surface S03

B.3 Beam S04

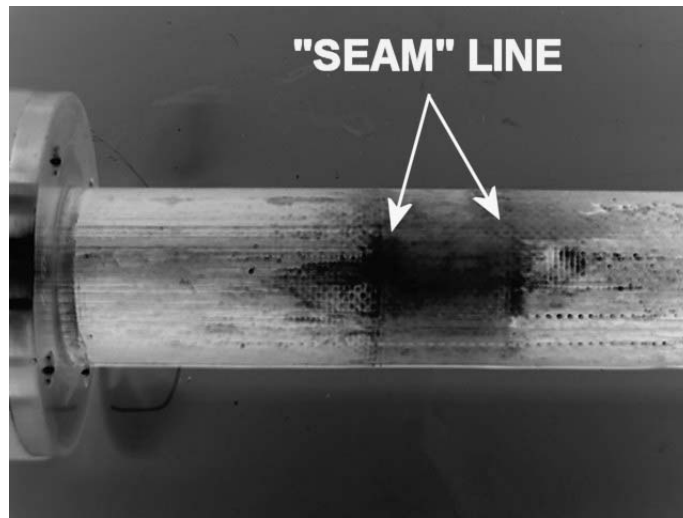


Figure B.5 Beam Surface S04

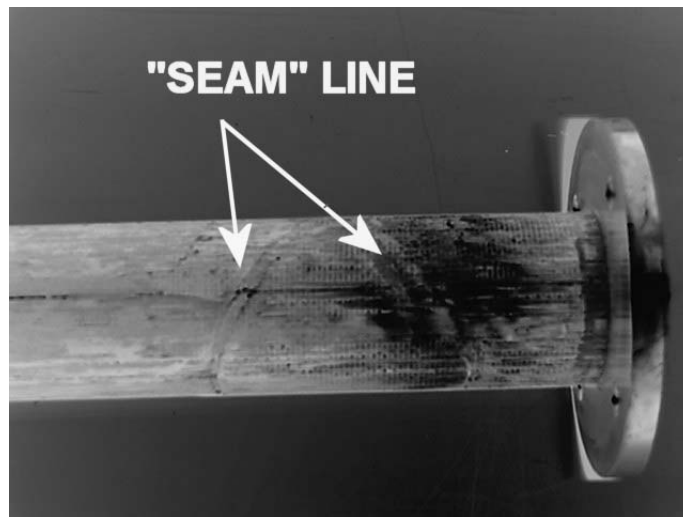


Figure B.6 Beam Surface S04

B.4 Beam S05

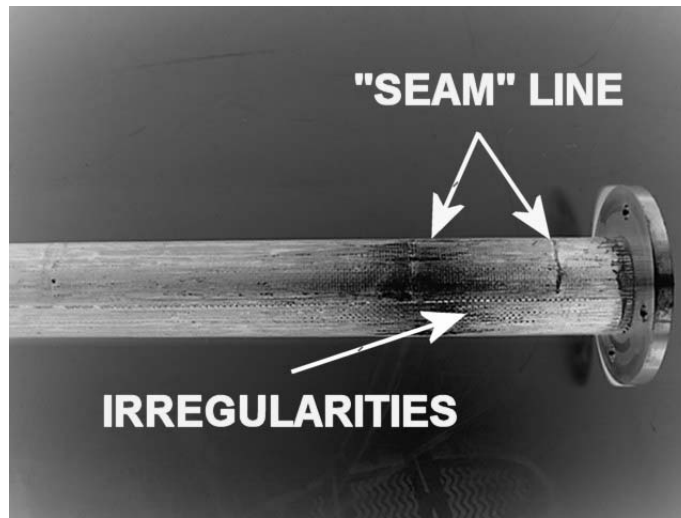


Figure B.7 Beam Surface S05

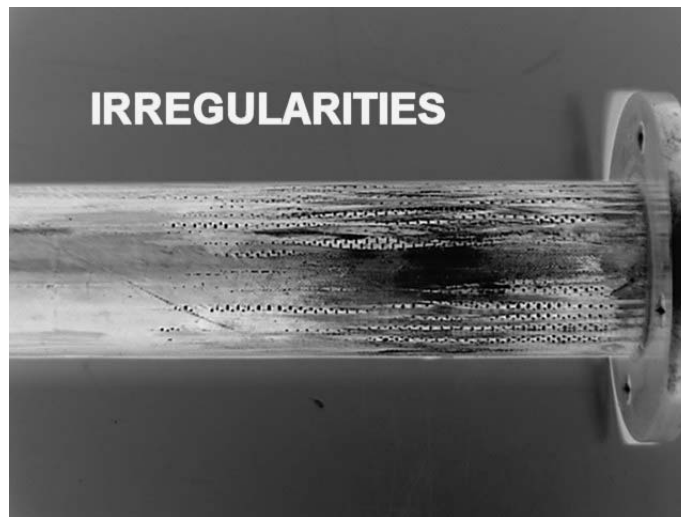


Figure B.8 Beam Surface S05

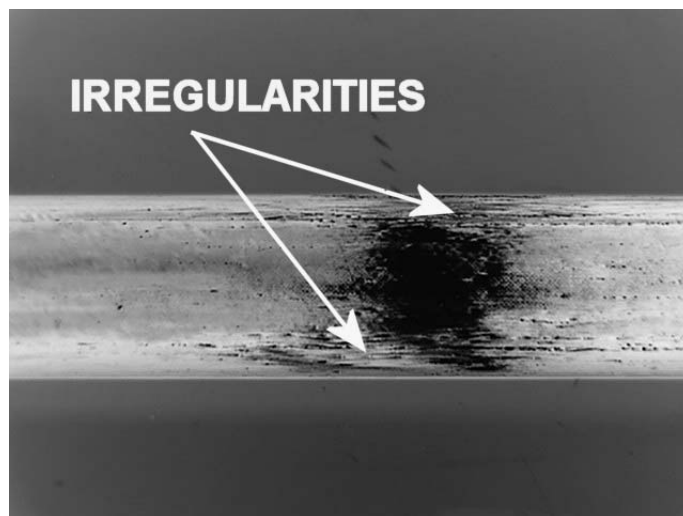


Figure B.9 Beam Surface S05

B.5 Beam S06



Figure B.10 Beam Surface S06

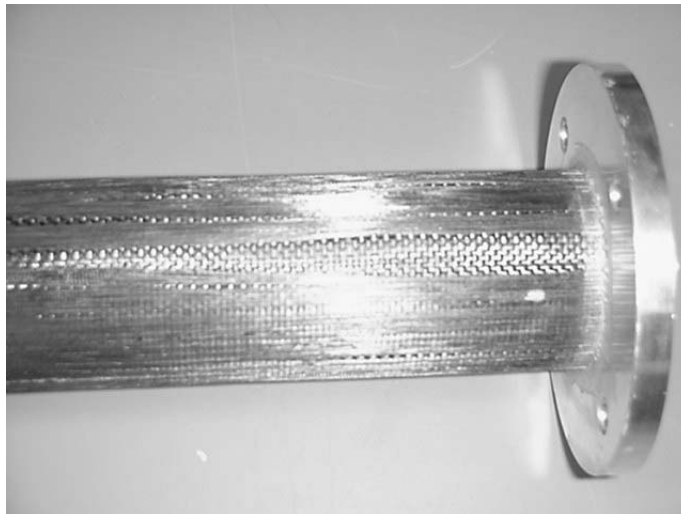


Figure B.11 Beam Surface S06

Appendix C. Modal Testing Data

The following sections show the data that was collected for each beam. Close-up pictures of the individual beams are shown, as well as the FRF for each axis of the tri-axial accelerometer and the vibrometer. The coherence for the Z axis is also shown. The modal data that was extracted from ERA and the frequencies from PSV are listed in tables at the end of each section. Note that not all of the data collected is shown; a representative result for each parameter or test is presented. The entire set of data was presented on CD to the Thesis Advisor.

C.1 FRF Excitation Comparisons for S02

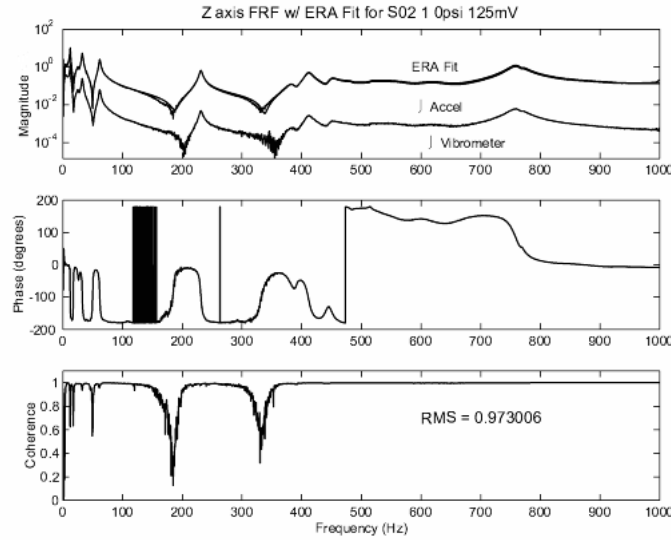


Figure C.1 Sample of Results used for Trial Comparison

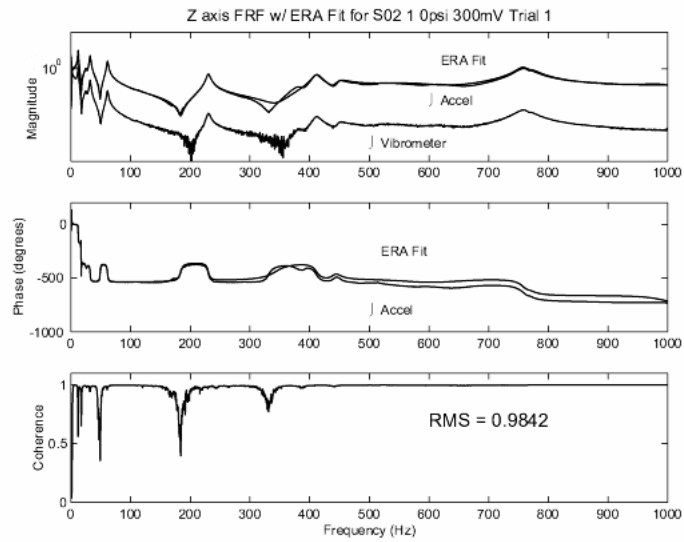


Figure C.2 Sample of Results used for Trial Comparison

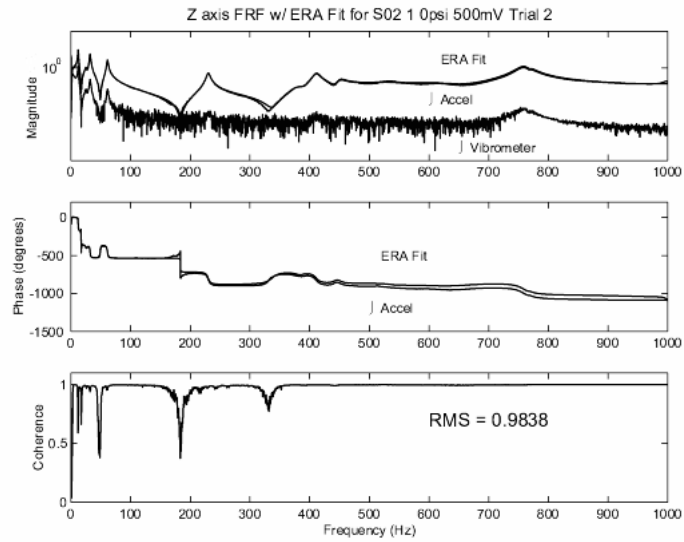


Figure C.3 Sample of Results used for Trial Comparison

C.2 FRF Pressure Comparisons for S02

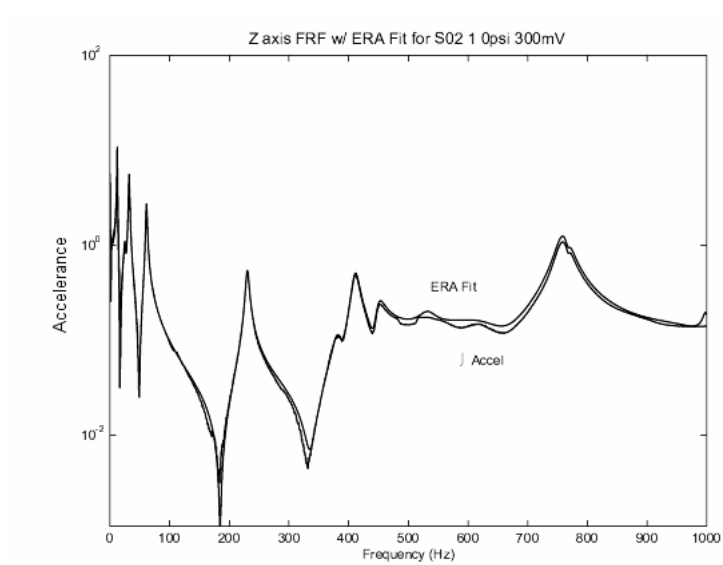


Figure C.4 Sample of Results used for Trial Comparison

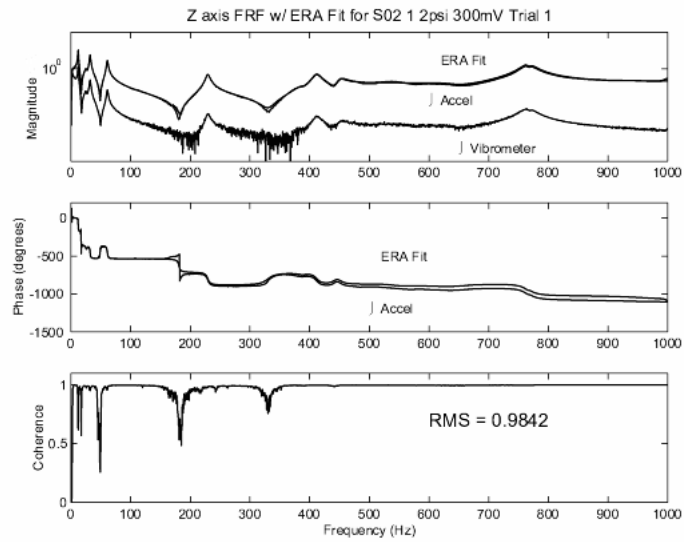


Figure C.5 Sample of Results used for Trial Comparison

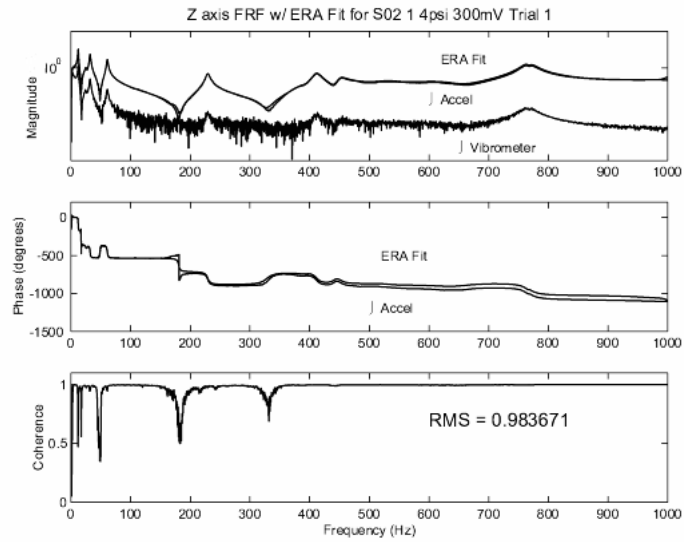


Figure C.6 Sample of Results used for Trial Comparison

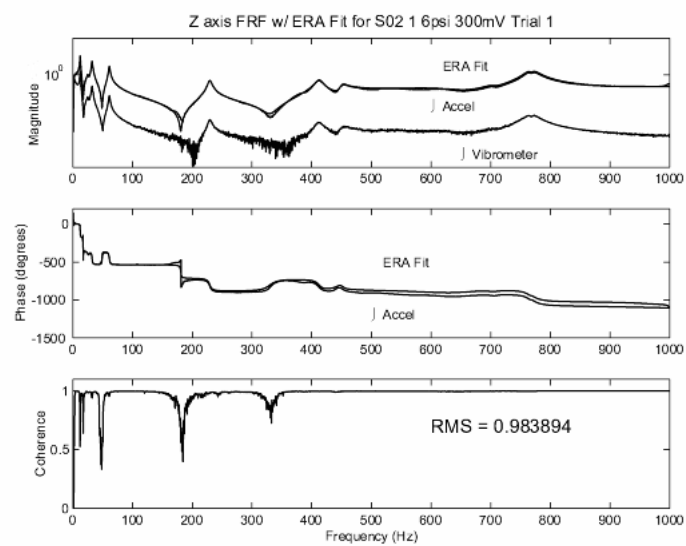


Figure C.7 Sample of Results used for Trial Comparison

The following two figures are for S05 and S06 for additional comparison. They perform as expected.

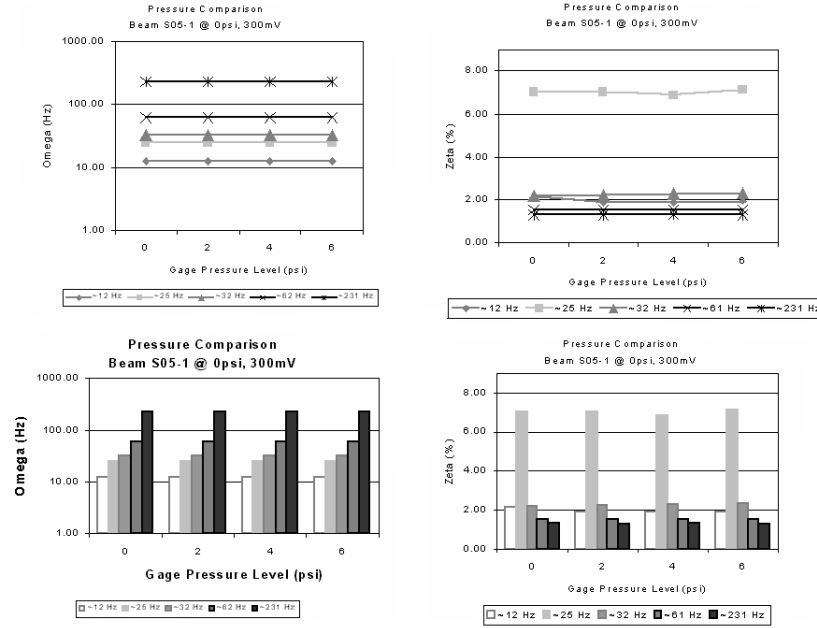


Figure C.8 Pressure Comparisons for S05-1

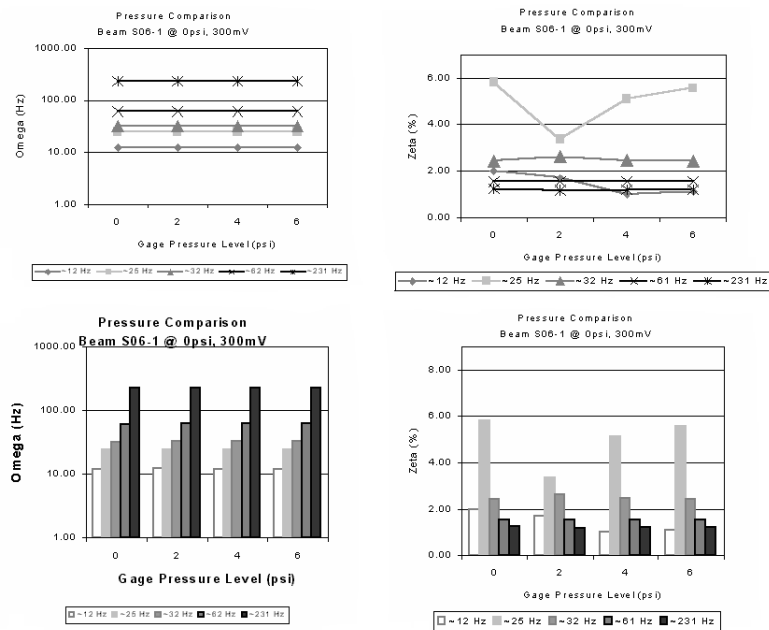


Figure C.9 Pressure Comparisons for S06-1

C.3 FRF Orientation Comparisons for S02

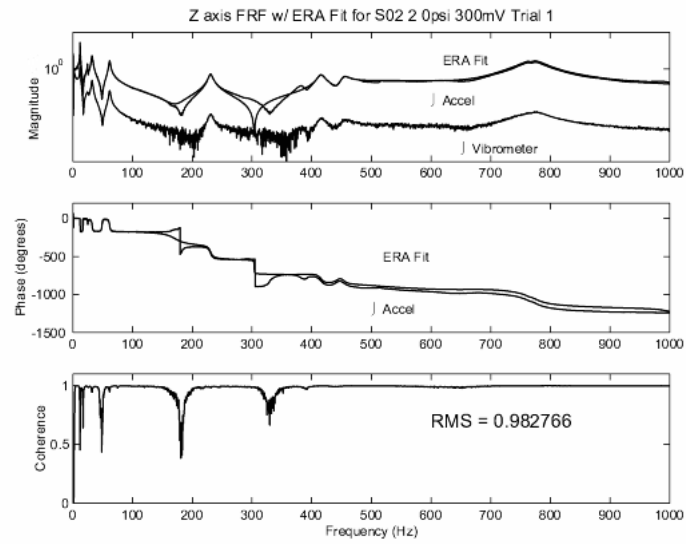


Figure C.10 Sample of Results used for Trial Comparison

C.4 S03 with PZT Test Data

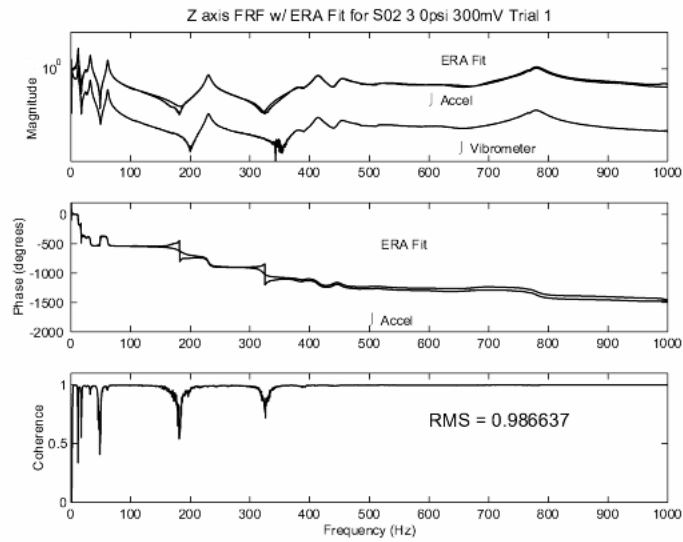


Figure C.11 Sample of Results used for Trial Comparison

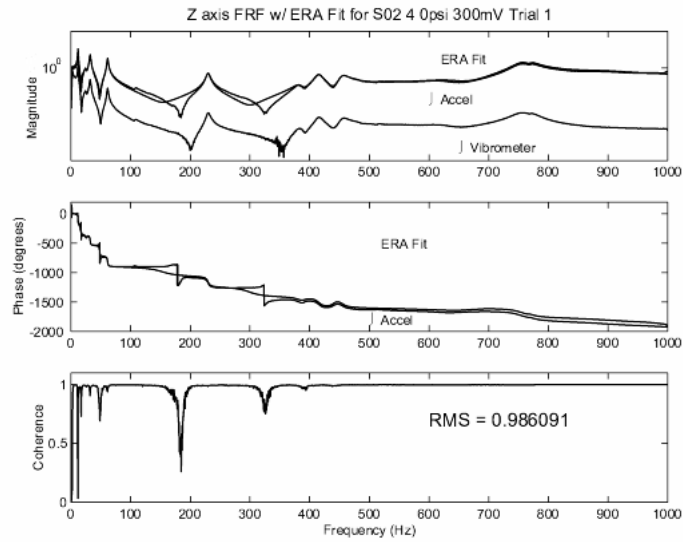


Figure C.12 Sample of Results used for Trial Comparison

Table C.1 S03 with PZT on with Shaker exciting at 0, 2, and 4 psi

0 psi			2 psi			4 psi		
Mode #	Freq (Hz)	Zeta (%)	Mode #	Freq (Hz)	Zeta (%)	Mode #	Freq (Hz)	Zeta (%)
1	1.47	100	1	1.93	100	1	1.64	100
.
2	11.89	2.03	2	11.88	2.13	2	11.9	1.91
3	29.49	9.26	3	29.56	9.49	3	29.83	9.49
4	33.03	5.01	4	33.06	4.67	4	33.13	4.85
5	45.28	39.11	5	50.43	4.76	.	.	.
6	62.34	1.79	6	62.4	1.64	5	62.41	1.66
.	6	75.51	100
7	231.33	1.1	7	231.38	1.06	7	231.43	1.08
.	.	.	8	343.1	100	.	.	.
8	381.62	3.73	9	386.42	3.4	8	386.46	3.55
9	412.55	1.26	10	412.7	1.43	9	412.7	1.37
10	428.25	100
11	493.53	15.29
12	525.67	5.81	11	534.36	4.02	10	531.6	4.82
13	648.33	2.96	12	671.27	20.9	11	672.57	18.49
.	.	.	13	769.65	1.37	12	748.37	2.88
14	817.16	0.73	14	817.66	0.79	13	801.43	0.87
.	14	826.24	0.77
15	839.22	0.81	15	838.7	0.8	15	839.09	0.7
.
16	1002	1.34	16	999.27	1.49	16	998.81	1.43

Table C.2 S03 with PZT with Shaker exciting at 6 psi

6 psi			Omega (Hz)		Zeta (%)	
Mode #	Freq (Hz)	Zeta (%)	Mean	STDEV	Mean	STDEV
1	1.51	100
2	6.52	100
3	11.9	1.96	11.89	0.01	2.01	0.10
4	29.9	9.14	29.70	0.20	9.35	0.17
5	33.16	4.45	33.10	0.06	4.75	0.24
.	18.27
6	62.43	1.62	62.40	0.04	1.68	0.08
.	.	.	231.38	0.04	1.07	0.03
7	231.39	1.04
.	.	.	385.11	2.34	3.50	0.18
8	385.95	3.33	412.68	0.09	1.36	0.07
9	412.77	1.39	412.68	0.09	1.36	.
.
.
10	532.03	3.39	660.35	13.38	14.73	8.04
11	649.22	16.57	768.77	19.98	1.59	1.20
12	788.3	0.52	811.76	7.56	0.80	0.06
13	810.77	0.8
.	.	.	839.37	0.77	0.84	0.15
14	840.47	1.05
15	850	0.57	999.69	1.56	1.44	0.07
16	998.67	1.48

Appendix D. Vacuum Tests Data

Table D.1 Vacuum Tests **0psi**, 25°C to 95°C

25°C, 300 Hz			25°C, 1000 Hz			35°C		
Coherence RMS = 0.9807			Coherence RMS = 0.9808			Coherence RMS = 0.9905		
Mode #	Freq (Hz)	Zeta (%)	Mode #	Freq (Hz)	Zeta (%)	Mode #	Freq (Hz)	Zeta (%)
1	0.23	100	1	51.18	0.74	1	51.1	0.73
2	47.19	1.63	2	64.25	1.18	2	63.78	1.09
3	51.09	0.95	3	113.22	0.51	3	112.81	0.46
4	51.7	1.02	4	122.55	1.59	4	123.32	1.27
5	64.17	1.09	5	179.46	0.92	5	179.21	0.66
6	96.54	12.46	6	231.58	1.83	6	231.42	0.77
7	113	0.53	7	333.01	0.67	7	330.36	2.2
8	122.34	0.76	8	337.81	2.17	8	333.04	0.6
9	156.39	1.77	9	376.27	0.79	9	364.1	30.55
10	179.25	0.87	10	420.44	78.3	10	376.02	0.75
11	198.9	1.37	11	653.36	0.77	11	648.75	0.89
12	223.75	1.17	12	673.29	0.53	12	670.57	0.7
13	231.29	0.83	13	732.76	1.69	13	734.02	1.19
14	257.65	10.12	14	978.7	16.43	14	1000.55	0.6
15	309.29	5.07	15	999.33	0.94	15	1037.27	12.61
16	380.84	100
Mean		1.42	Mean		1.10	Mean		0.92
STDEV		1.20	STDEV		0.54	STDEV		0.45

45°C, 300 Hz			55°C, 1000 Hz			65°C		
Coherence RMS = 0.9899			Coherence RMS = 0.9861			Coherence RMS = 0.9889		
.	.	.	1	0.05	100	1	0	100
.	.	.	2	47.84	100	2	47.06	1.82
1	50.81	0.81	3	50.08	1.24	3	49.13	1.69
2	63.43	1.06	4	62.82	1.4	4	62.61	1.06
3	112.65	0.11	5	111.82	0.33	5	111.68	0.5
4	124.91	7.56	.	.	.	6	121.28	0.95
.	7	151.07	2.08
5	179.64	1.1	6	178.83	0.79	8	178.38	0.93
6	235.05	4.06	7	227.89	3.24	9	229.14	1.53
7	298.32	100	.	.	.	10	332.71	2.01
8	333.93	0.39	8	332.68	0.84	11	333.29	0.7
9	334.31	1.39	9	346.12	100	12	371.35	0.6
10	375.74	0.75	10	374.98	0.76	13	373.86	0.92
11	635.9	1.33	.	.	.	14	569.6	100
12	662.15	1.01	11	642.53	2.18	15	610.23	2.84
.	.	.	12	1001.37	1.66	16	1000.14	0.52
13	1002.56	1.44	.	.	.	17	1019.27	11.46
Mean		1.75	Mean		1.38	Mean		1.30
STDEV		2.08	STDEV		0.89	STDEV		0.71

75°C, 300 Hz			85°C, 1000 Hz			95°C		
Coherence RMS = 0.9891			Coherence RMS = 0.9886			Coherence RMS = 0.9888		
1	0.72	100	1	46.59	1.76	1	0.18	100
2	47.74	1.76	2	62.23	1.07	2	45.55	1.69
3	62.4	1.04	3	111.23	0.36	3	62.15	1.06
4	111.51	0.41	4	121.34	1.33	4	108.69	100
5	121.29	1.16	5	149.99	1.09	5	110.99	0.44
6	150.16	1.15	6	151.67	100	6	177.36	1.1
7	178.33	1.01	7	177.99	1	7	222.98	5.88
8	229.26	2.02	8	229.77	1.83	8	236.39	14.96
9	327.3	0.75	9	308.92	100	9	325.17	0.4
10	331.89	0.72	10	326.44	0.45	10	330.57	0.81
11	350.52	3.18	11	331.16	0.8	11	342.3	3.4
12	372.17	0.82	12	343.04	2.15	12	368.62	0.85
13	571.06	3.37	13	367.33	0.25	13	496.05	3.92
14	693.32	100	14	370.46	0.86	14	965.7	17.5
15	1000.43	0.64	15	535.48	3.95	15	976.84	2.97
16	1019.09	11.61	16	998.21	6.32	16	999.62	0.39
Mean		1.39	Mean		1.66	Mean		1.91
STDEV		0.95	STDEV		1.64	STDEV		1.75

Table D.2 Vacuum Tests **4psi** 25°C and 35°C

25°C			35°C		
Coherence RMS = 0.9886			Coherence RMS = 0.9885		
Mode #	Freq (Hz)	Zeta (%)	Mode #	Freq (Hz)	Zeta (%)
1	0.07	100	1	0.1	100
2	50.98	0.77	2	50.92	0.75
3	64.09	1.28	3	63.56	1.4
4	112.38	0.85	4	112.29	0.88
5	331.91	0.94	5	182.59	5.51
6	375.46	100	6	332.14	0.89
7	376.11	0.83	7	376.06	0.78
8	665.5	0.63	8	436.84	100
9	1016.17	5.19	9	663.69	0.66
.	.	.	10	1000.81	2.38
Mean		1.50	Mean		1.66
STDEV		1.64	STDEV		1.66

Table D.3 Vacuum Tests **4psi**, 45°C to 95°C

45°C, 300 Hz			55°C, 1000 Hz			65°C		
Coherence RMS = 0.9871			Coherence RMS = 0.9874			Coherence RMS = 0.9871		
Mode #	Freq (Hz)	Zeta (%)	Mode #	Freq (Hz)	Zeta (%)	Mode #	Freq (Hz)	Zeta (%)
1	12.81	100	1	0.73	100	1	1.81	100
2	50.73	0.87	2	50.23	1.08	2	49.33	1.49
3	63.02	1.11	3	62.72	1.04	3	62.57	1.02
4	112.08	0.93	4	111.65	0.85	4	111.44	0.73
5	120.63	3.87	5	120.65	2.42	5	120.67	2.14
6	184.12	1.22	6	183.77	1.14	6	149.34	2.08
7	229.53	2.22	7	202.3	100	7	183.55	1.1
8	267.78	100	8	228.48	1.56	8	227.94	1.84
9	331.93	1.83	9	325.68	2.12	9	326.64	0.75
10	332.13	0.49	10	331.97	0.67	10	331.53	0.73
11	375.8	0.78	11	367.75	8.27	11	354.72	4.1
12	658.4	0.91	12	375.1	0.8	12	374.23	0.83
13	681.7	0.89	13	647.47	1.52	13	391.2	100
14	733.29	1.29	14	688.99	5.22	14	621.44	2.16
15	999.37	0.7	15	1000.25	0.64	15	1000.23	0.59
16	1019.76	13.28	16	1018.94	11.13	16	1022.1	11.47
Mean		1.32	Mean		2.10	Mean		1.50
STDEV		0.90	STDEV		2.22	STDEV		0.98

75°C, 300 Hz			85°C, 1000 Hz			95°C		
Coherence RMS = 0.9846			Coherence RMS = 0.9872			Coherence RMS = 0.9876		
Mode #	Freq (Hz)	Zeta (%)	Mode #	Freq (Hz)	Zeta (%)	Mode #	Freq (Hz)	Zeta (%)
1	0.69	100	1	0.95	100	1	0.05	100
2	48.05	1.67	2	46.78	1.71	2	45.77	1.56
3	62.24	0.76	3	62.19	0.61	3	62.05	0.57
4	111.14	0.6	4	110.99	0.41	4	103.04	100
5	120.5	2.1	5	121.72	4.28	5	110.45	0.5
6	148.72	2.11	6	149.41	3.4	6	130.28	1.44
7	183.05	1.02	7	182.87	1.06	7	182.33	0.8
8	226.81	2.2	8	196.02	100	8	227.79	2.18
9	325.81	0.46	9	228.26	2.9	9	272.72	100
10	331.01	0.79	10	325.07	0.59	10	325.62	0.6
11	351.39	4.77	11	330.42	0.78	11	329.48	0.79
12	372.76	0.84	12	354.42	5.24	12	354.48	3.38
13	409.36	100	13	371.12	0.86	13	369.51	0.88
14	586.47	2.85	14	546.25	3.5	14	512.69	3.7
15	1000.24	0.62	15	1000.8	0.89	15	975.47	4.39
16	1022.29	11.99	16	1045.13	13.56	16	999.95	0.4
Mean		1.60	Mean		2.02	Mean		1.63
STDEV		1.23	STDEV		1.64	STDEV		1.36

Bibliography

1. Agnes, Gregory, Maj. USAF. *Beam-Type Modelling of Adaptive Inflatable Beams*. Technical Report, Dayton, OH: Air Force Institute of Technology, 2002.
2. Allemang, Randall. *Vibrations: Experimental Modal Analysis*. Technical Report, Cincinnati, OH: University of Cincinnati, Structural Dynamics Research Lab, 1995.
3. Beards, C. F. *Vibration Analysis and Control System Dynamics*. Chichester, England: Ellis Horwood Limited, 1981.
4. Beards, C. F. *Engineering Vibration Analysis with Application to Control Systems*. New York: Halsted Press, 1996.
5. Cassapakis, Dr. Costa and Dr. Mitch Thomas. *Inflatable Structures Technology Development Overview*. Technical Report AIAA 95-3738, Tustin, CA: L'Garde, Inc., 1995. www.lgarde.com.
6. Clough, W. and J. Penzien. *Dynamics of Structures*. New York: McGraw-Hill, 1975.
7. Cobb, Richard, Captain USAF. *Structural Damage Identification From Limited Measurement Data*. Dissertation, Air Force Institute of Technology, Dayton, OH, March 1996.
8. Cobb, Richard G., Captain USAF. *An Experimental Determination of the Effects of Blending Collocated and Non-Collocated Sensor Measurements to Control a Flexible Structure*. Master's Thesis, Air Force Institute of Technology, Dayton OH, December 1992.
9. Cox, Amy, Second Lieutenant USAF. *A Statistical Analysis of Space Structure Mode Localization*. Masters's Thesis, Air Force Institute of Technology, Dayton OH, March 1999.
10. C.R. Fuller, S.J. Elliot and P.A. Nelson. *Active Control of Vibration*. San Diego, CA: Academic Press, 1996.
11. Cudney, H.H. and D.J. Inman. "Determining Damping Mechanisms in a Composite Beam by Experimental Modal Analysis," *Journal of Modal Analysis*, 138-143 (October 1989).
12. Data, Physics Corporation. *Making Measurements with SignalCalc 620*. User Manual, San Jose, CA: Data Physics Corporation, 1998.
13. DiSebastian III, John, Captain USAF. *RIGEX: Preliminary Design of a Rigidized Inflatable Get-Away-Special Experiment*. Master's Thesis, Air Force Institute of Technology, Dayton OH, March 2001.

14. Division, Micro-Measurements. *Strain Gage Installations with M-Bond 300 Adhesive*. Instruction Bulletin B-133-2, Raleigh, NC: Measurements Group, Inc, February 1996.
15. Division, Micro-Measurements. *Strain Gage Installations with M-Bond AE-10, AE-15, and GA-2 Adhesive Systems*. Instruction Bulletin B-137-16, Raleigh, NC: Measurements Group, Inc, November 1999.
16. ENDEVCO. *Model 63B-100 Accelerometer Product Sheet*. Technical Report 0799, San Juan Capistrano, CA: ENDEVCO Corporation.
17. ENDEVCO. *Technical Information for Models 2250A-10/2250AM1-10 Micro Miniature IsotronTM Shear Accelerometers*. ENDEVCO General Catalog, San Juan Capistrano, CA: ENDEVCO Corporation, 1989.
18. Ewins, D.J. *Modal Testing: Theory and Practice*. Engineering Dynamics, Letchworth England: Research Studies Press LTD., 1984.
19. Freeland, Robert, Steven Bard Gordon Veal Gayle Bilyeu Costa Cassapakis Thomas Campbell M.C. Bailey. *Inflatable Antenna Technology with Preliminary Shuttle Experiment Results and Potential Applications*. Technical Report AIAA 95-3738, Pasadena and Tustin, CA and Hampton VA: Jet Propulsion Laboratory, L'Garde, Inc., NASA Langley Research Center, 1996. www.lgarde.com.
20. Gaudreault, Michele, Captain USAF. *Simultaneous Design of Active Vibration Control and Passive Damping*. Dissertation, Air Force Institute of Technology, Dayton, OH, December 1993.
21. Goossens, Michel, Frank Mittelbach and Alexander Samarin. *The L^AT_EX Companion*. New York: Addison-Wesley Publishing Company, 1994.
22. Grätzer, George. *Math into L^AT_EX* (3 Edition). Boston: Birkhäuser-Springer, 2000.
23. Harker, Ralph J. *Generalized Methods of Vibration Analysis*. New York: John Wiley and Sons, 1983.
24. Huybrechts, Dr. Steven and Dr. Keith Denoyer of the AFRL Space Vehicles Directorate. "Innovations in spacecraft component technology are redefining space in the 21st century," *AFRL Technology Horizons*, 1(3):11–16 (September 2000).
25. Inman, Daniel J. *Engineering Vibration* (Second Edition). Upper Saddle River New Jersey: Prentice Hall, 2001.
26. Jenkins, Christopher H. *Gossamer Spacecraft: Membrane and Inflatable Structures Technology for Space Applications, 191*. Progress in Astronautics and Aeronautics. Reston, VA: The American Institute of Aeronautics and Astronautics, Inc., 2001.

27. Juang, J. and R.S. Pappa. "An Eigensystem Realization Algorithm for Modal Parameter Identification and Model Algorithm," *AIAA Journal of Guidance, Control, and Dynamics*, 8(5):620–627 (1985).
28. Main, John. *Analysis and Design of Inflatable Aerospace Structures*. PhD Dissertation, Vanderbilt University, Nashville TN, May 1993.
29. Main, John A., Robert A. Carlin Ephraim Garcia Steven W. Peterson and Alvin M. Strauss. "Dynamic analysis of space-based inflated beam structures," *Journal of Acoustical Society of America*, 97(2):1035–1045 (February 1995).
30. Main, John A., Steven W. Peterson and Alvin M. Strauss. "Beam-Type Bending of Space-Based Inflated Membrane Structures," *Journal of Aerospace Engineering*, 8(2):120–125 (April 1995).
31. Meirovitch, Leonard. *Elements of Vibration Analysis* (Second Edition). New York: McGraw-Hill, 1986.
32. Michel Lalanne, Patrick Berthier, Johan Der Hagopian. *Mechanical Vibrations for Engineers*. New York: John Wiley and Sons, 1984.
33. Minco. *Recommended Adhesives for ThermofoilTM Heater Installation*. Application Aid #22, Minneapolis, MN: Minco Products, Inc., August 2000.
34. Minco. *Thermofoil Heaters*. Product Bulletin HS-201, Minneapolis, MN: Minco Products, Inc., June 2000.
35. Wertz, James and Wiley Larson. *Space Mission Analysis and Design* (Third Edition). Space Technology Series, El Segundo CA: Microcosm Press and Kluwer Academic Publishers, 1999.
36. Ying, Shuh-Jing. *Advanced Dynamics*. AIAA Education Series, Reston, VA: American Institute of Aeronautics and Astronautics, 1997.

Vita

Captain Thomas G. Single was born in Baltimore, Maryland. He graduated from North Harford High School in Pylesville, Maryland. Captain Single entered undergraduate studies at Worcester Polytechnic Institute (WPI) in Worcester, Massachusetts. While at WPI, he majored in Aerospace Engineering and graduated with a Bachelor of Science in Mechanical Engineering.

His first assignment was to the 392nd Training Squadron at Vandenberg AFB, California, for Undergraduate Missile Training. He was assigned as a Missile Combat Crewmember to the 319th "Screaming Eagles" Missile Squadron at the 90th Space Wing, F.E. Warren AFB, Wyoming. During this time, he earned a Masters of Business Administration in Operations Management from Regis University in Denver, Colorado. He was subsequently assigned to the 90th Operations Support Squadron as an Emergency War Orders Trainer and as Chief, Emergency War Orders Training.

In August 2000, he began the Graduate Space Operations program at the Air Force Institute of Technology, Wright Patterson AFB, Ohio. He also anticipates earning a second Master of Science degree in Astronautical Engineering from AFIT in the fall of 2002. Upon graduation, he will be assigned to the 17th Test Squadron (AFSPC), Schriever AFB, Colorado.

REPORT DOCUMENTATION PAGE				Form Approved OMB No. 074-0188	
<p>The public reporting burden for this collection of information is estimated to average 1 hour per response, including the time for reviewing instructions, searching existing data sources, gathering and maintaining the data needed, and completing and reviewing the collection of information. Send comments regarding this burden estimate or any other aspect of the collection of information, including suggestions for reducing this burden to Department of Defense, Washington Headquarters Services, Directorate for Information Operations and Reports (0704-0188), 1215 Jefferson Davis Highway, Suite 1204, Arlington, VA 22202-4302. Respondents should be aware that notwithstanding any other provision of law, no person shall be subject to a penalty for failing to comply with a collection of information if it does not display a currently valid OMB control number.</p> <p>PLEASE DO NOT RETURN YOUR FORM TO THE ABOVE ADDRESS.</p>					
1. REPORT DATE (DD-MM-YYYY) 26-03-2002		2. REPORT TYPE Master's Thesis		3. DATES COVERED (From – To) Aug 2000 – Mar 2002	
4. TITLE AND SUBTITLE EXPERIMENTAL VIBRATION ANALYSIS OF INFLATABLE BEAMS FOR AN AFIT SPACE SHUTTLE EXPERIMENT				5a. CONTRACT NUMBER	
				5b. GRANT NUMBER	
				5c. PROGRAM ELEMENT NUMBER	
6. AUTHOR(S) Single, Thomas G., Captain, USAF				5d. PROJECT NUMBER 02-131	
				5e. TASK NUMBER	
				5f. WORK UNIT NUMBER	
7. PERFORMING ORGANIZATION NAMES(S) AND ADDRESS(S) Air Force Institute of Technology Graduate School of Engineering and Management (AFIT/ENY) 2950 P Street, Building 640 WPAFB OH 45433-7765				8. PERFORMING ORGANIZATION REPORT NUMBER AFIT/GSO/ENY/02-2	
9. SPONSORING/MONITORING AGENCY NAME(S) AND ADDRESS(ES) AFOSR/NA Structural Mechanics Attn: Mr. Daniel Segalman 801 North Randolph Street Arlington, VA 22203 COMML: 703-696-7259 e-mail: Daniel.Segalman@afosr.af.mil				10. SPONSOR/MONITOR'S ACRONYM(S)	
				11. SPONSOR/MONITOR'S REPORT NUMBER(S)	
12. DISTRIBUTION/AVAILABILITY STATEMENT APPROVED FOR PUBLIC RELEASE; DISTRIBUTION UNLIMITED.					
13. SUPPLEMENTARY NOTES					
14. ABSTRACT The development of lightweight, large-aperture optics is of vital importance to the Department of Defense and the US Air Force for improving remote sensing capabilities. One way of constructing a large space structure is to use rigidized, inflatable beams. This research presents the experimental vibration analysis of the ground testing for inflatable beams that will be used in an AFIT Space Shuttle rigidized inflatable beams experiment. The natural frequencies, damping ratios, and bending modes were identified for the beams. Various parameters were modified to determine what affects the vibration characteristics of the beams. The test results were compared to an Euler-Bernoulli beam model using a Ritz approximation.					
15. SUBJECT TERMS RIGEX, Inflatable Structures, Inflatable Beams, Vibration Testing, Modal Analysis, GASCAN Experiments, Large Space Structures, Experimental Vibration Analysis					
16. SECURITY CLASSIFICATION OF:			17. LIMITATION OF ABSTRACT UU	18. NUMBER OF PAGES 179	19a. NAME OF RESPONSIBLE PERSON Gregory S. Agnes, Maj, USAF (ENY)
a. REPORT U	b. ABSTRACT U	c. THIS PAGE U			19b. TELEPHONE NUMBER (Include area code) (937) 255-6565, ext 4317; e-mail: Gregory.Agnes@afit.edu